ExPo: A Sensitive Imaging Polarimeter for Observations of Scattered Light from Circumstellar Environments

© 2011 M. Rodenhuis
Alle rechten voorbehouden

ISBN 978-90-393-55879

Gedrukt door Wöhrmann Print Service, Zutphen

Cover image: Polarized intensity image made with ExPo of the circumstellar envelope surrounding the young star T Tauri.

ExPo: A Sensitive Imaging Polarimeter for Observations of Scattered Light from Circumstellar Environments

ExPo: Een gevoelige beeldvormende polarimeter voor waarnemingen van gereflecteerd licht van de omgevingen van sterren

(met een samenvatting in het Nederlands)

Proefschrift

ter verkrijging van de graad van doctor aan de Universiteit Utrecht op gezag van de rector magnificus, prof. dr. G. J. van der Zwaan, ingevolge het besluit van het college voor promoties in het openbaar te verdedigen op donderdag 16 juni 2011 des ochtends te 10.30 uur

door

Michiel Rodenhuis

geboren op 25 september 1971 te Schiedam

Promotor: Prof. dr. C. U. Keller

Contents

1 Introduction **1**
- 1.1 High-contrast astronomy . . . 1
- 1.2 The high-contrast challenge . . . 2
  - 1.2.1 Coronagraphy . . . 3
  - 1.2.2 Differential imaging . . . 3
  - 1.2.3 Polarimetry . . . 4
- 1.3 ExPo: The Extreme Polarimeter . . . 6
- 1.4 ExPo science drivers . . . 6
  - 1.4.1 Circumstellar disks . . . 6
  - 1.4.2 Dust shells around evolved stars . . . 8
  - 1.4.3 Exoplanets . . . 8
- 1.5 The development of ExPo . . . 9
- 1.6 Outlook . . . 10
- 1.7 Thesis overview . . . 10
- 1.8 A first peek . . . 11
- 1.9 References . . . 12

2 The Extreme Polarimeter: Design of a sensitive imaging polarimeter **15**
- 2.1 Introduction . . . 16
- 2.2 The ExPo design . . . 17
  - 2.2.1 Design objectives . . . 17
  - 2.2.2 ExPo polarimeter design . . . 17
  - 2.2.3 ExPo optical design . . . 19
  - 2.2.4 Atmospheric dispersion compensator . . . 20
  - 2.2.5 The ExPo camera . . . 21
  - 2.2.6 Mechanical design . . . 21
  - 2.2.7 Control software . . . 22
- 2.3 Laboratory concept demonstration . . . 23
- 2.4 Outlook . . . 25
- 2.5 References . . . 26

3 An exoplanet and circumstellar disk laboratory simulator for testing polari-

metric imaging instruments **27**
3.1 Introduction . . . 28
3.2 Simulator requirements . . . 29
3.2.1 Exoplanet simulator requirements . . . 29
3.2.2 Circumstellar disk simulator requirements . . . 29
3.3 Exoplanet simulator design . . . 29
3.3.1 Design overview . . . 29
3.3.2 Design implementation . . . 30
3.4 Exoplanet simulator performance . . . 34
3.5 Design of the circumstellar disk simulator . . . 35
3.6 Circumstellar disk simulator performance . . . 38
3.7 Discussion and conclusion . . . 39
3.8 References . . . 41

4 The Extreme Polarimeter: A sensitive imaging polarimeter for high-contrast observations of scattered light from circumstellar environments **43**
4.1 Introduction . . . 44
4.2 Beam-exchange polarimetry . . . 45
4.3 Instrument design . . . 46
4.4 Data reduction and polarimetric calibration . . . 50
4.5 Instrument performance . . . 54
4.6 Sample result: AB Aurigae . . . 58
4.7 Discussion & conclusion . . . 60
4.8 References . . . 62

5 Imaging polarimetry of the asymmetric dust envelope around the Mira binary system **65**
5.1 Introduction . . . 66
5.2 Observations . . . 67
5.3 Imaging polarimetry results . . . 67
5.4 Modeling the bipolar structure of the Mira envelope . . . 71
5.5 Discussion & conclusion . . . 75
5.6 References . . . 75

6 High-contrast imaging: Reaching 10^{-8} using polarimetry **77**
6.1 Introduction . . . 78
6.2 Experiment set-up . . . 79
6.3 Data reduction . . . 80
6.4 Results . . . 81
6.5 Discussion & conclusion . . . 81
6.6 References . . . 83

7 First detection of ring-like polarized features in the atmosphere of Venus **85**
7.1 Introduction . . . 86

7.2 Observations . . . 86
7.3 Image processing . . . 87
7.4 Results . . . 88
7.5 Discussion . . . 94
7.5.1 Increased polarization in the polar regions . . . 94
7.5.2 Polarized rings: An instrumental effect? . . . 96
7.5.3 Polarized rings: A halo effect? . . . 98
7.5.4 Intensity gradient and optical depth effects . . . 98
7.5.5 Polarized rings: Stratification in the Venus atmosphere? . . . 99
7.5.6 Why have the polarized rings not been observed before? . . . 100
7.6 Conclusion . . . 101
7.7 References . . . 101

8 Samenvatting in het Nederlands 103
8.1 Hoge-contrast sterrenkunde . . . 103
8.2 Het ontwerp van ExPo . . . 104
8.3 De testsimulator . . . 105
8.4 Beeldbewerking, kalibratie en gevoeligheid . . . 105
8.5 Eerste resultaten . . . 106
8.6 Mira . . . 107
8.7 Contrast van 10^{-8} in het laboratorium . . . 107
8.8 Polarimetrie van de Venusatmosfeer . . . 107
8.9 Vooruitblik . . . 108

Acknowledgments 109

Curriculum vitae 111

Chapter 1

Introduction

1.1 High-contrast astronomy

Over the past centuries, our knowledge about the universe has increased as the technologies we employ to observe it have advanced. Relying only on the naked eye, generations of astronomers have been able to observe the 5600 stars brighter than 6^{th} magnitude as well as the Moon, the planets out to Saturn and transient phenomena such as comets and supernovae. With the development of telescopes and their associated instrumentation, it has become possible to observe ever fainter objects. The Hubble Space Telescope (HST) has observed targets fainter than 30^{th} magnitude in the visible (Hathi et al. 2007), a brightness almost $4{\times}10^{-9}$ times that of the faintest visible stars.

There are, however, many cases in which a comparatively faint astronomical target is accompanied by a much brighter source at close proximity. Observing such faint targets poses an enormous challenge even for today's extremely sensitive astronomical instruments.

A prime example of this type of targets are planets orbiting other stars: exoplanets. The brightness of Jupiter is about 10^{-9} compared with that of the Sun. This is comparable to the size ratio of Mount Everest and a red blood cell. Directly observing such an exoplanet is thus similar to finding a red blood cell on the slopes of Mount Everest using only an altimeter (Keller, private communication). The numerous, mostly indirect, detections of exoplanets (Schneider 2010) have generated a lot of interest, both within the astronomical community as in the general public. As a result, development of high-contrast imaging techniques with the goal of directly observing exoplanets, has accelerated.

High-contrast imaging has many more applications than exoplanets, however. The direct imaging of protoplanetary disks, the birthplace of planets, and debris disks, made up of the material that did not form planets, also requires high contrasts. Examples of these types of targets can be found in figures 1.1 & 1.2. Even stars in

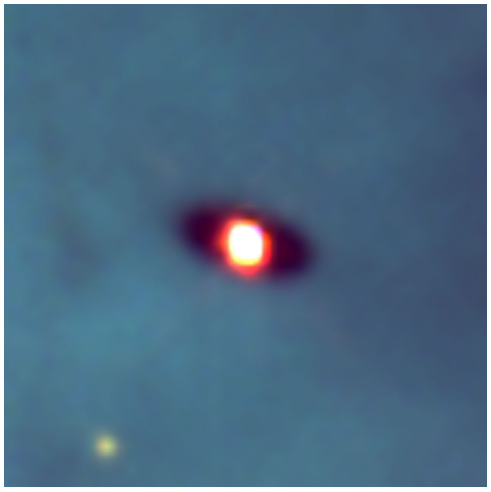

Figure 1.1: The protoplanetary disk around a young star is silhouetted against the bright backdrop of the hot gas of the Orion nebula. The object at lower left is not associated with the star. Image credit: Mark McCaughrean (Max-Planck-Institute for Astronomy), C. Robert O'Dell (Rice University), and NASA/ESA.

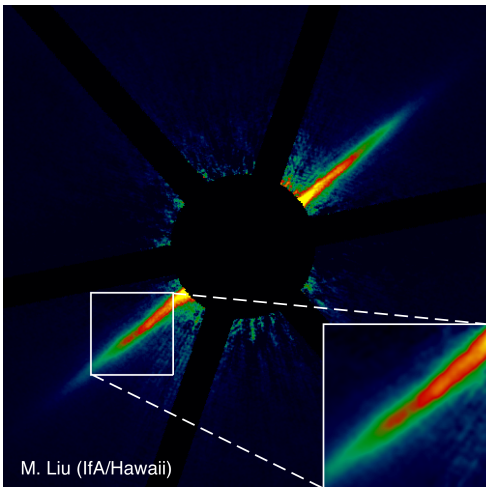

Figure 1.2: Infrared image of the edge-on debris disk around the star AU Microscopii obtained with the Keck II Telescope. The disk is visible because its orbiting dust particles scatter the light of the star. The image is 100 Astronomical Units wide, about the size of our solar system. The black mask blocks out the inner 15 AU in radius and the optical artifacts from the bright central star. Irregularities in the disk (insert) may be the sign of planet(s) orbiting this star. Image credit: M. Liu, IfA-Hawaii/Keck Observatory.

their last stages of life show highly interesting phenomena, such as circumstellar envelopes or shells formed through rapid mass loss, that can only be imaged with high contrast.

1.2 The high-contrast challenge

Achieving high contrast poses numerous challenges. First of all, recording a strong and a weak signal simultaneously requires an instrument with a large dynamic range. Observing two targets at a small separation furthermore requires high angular resolution if the two sources must be separated spatially.

The separation should be seen in relation to the resolving power of the optical system used. Because of the diffraction of the entrance aperture, even a perfect optical system will not be able to focus a point source to an infinitely small point, but spreads it out in an Airy pattern. This imposes a limit, the diffraction limit, on the

separation between sources that can be resolved, which depends on the wavelength and the size of the telescope aperture (equation 1.1),

$$\theta = \frac{1.22\lambda}{D}. \tag{1.1}$$

As an example, the Hubble Space Telescope should theoretically be able to achieve an angular resolution of 0.05'' in the visible. In practice, the resolution provided is about 0.1''. As a comparison, the innermost planet directly imaged around the star HR8799 (Marois et al. 2008) has an angular separation of about 0.6''. Circumstellar disks around nearby stars can extend for tens of arcseconds.

For ground based telescopes, the atmospheric seeing further blurs the image, reducing the angular resolution. High-contrast imaging therefore requires large telescopes and high-order adaptive optics (AO) systems to counteract the seeing-induced blurring. Even if these preconditions are met, supplementary techniques are required to reach the desired contrast:

1.2.1 Coronagraphy

A classic technique to reduce the starlight is coronagraphy: masking the star but with a mask sufficiently small that a planet can still be observed outside the edge of the mask. The classic coronagraph is the Lyot design consisting of a circular mask in the focal plane and an aperture (Lyot stop) in a pupil plane that removes the light diffracted at the edge of the telescope aperture. A host of modern coronagraph types exist (e.g. Guyon 2003, Mawet et al. 2005, Swartlander et al. 2008) with many concepts relying on destructive interference between different parts of the beam. These concepts claim very high contrast performance (e.g. 10^{-7} at a separation of 3 λ/D for the Annular Groove Phase Mask (AGPM) coronagraph, Mawet et al. 2005), but not all of them are very practical, requiring for example very high pointing accuracy to center the star on the coronagraph axis. On sky, the contrast achieved is generally quite a bit lower. The state-of-the-art HiCIAO AO-assisted coronagraph instrument on the 8.2–m Subaru telescope (Hodapp et al. 2008) achieves a H-band contrast of 10^{-4} at 0.5'' and 10^{-5} at 1'' separation, using a coronagraph with an inner working angle of 0.3'' (Suzuki et al. 2010). At NASA's JPL laboratory, a contrast of 10^{-10} has been achieved on a laboratory test-bed for a space mission; the Terrestial Planet Finder (Trauger & Traub 2007, Levine et al. 2009). However, this required a temperature-stabilized setup inside a vibration-damped vacuum tank and only works for monochromatic laser light.

1.2.2 Differential imaging

Even with a high-order AO system and an advanced coronagraph design, it is still difficult to detect a (planet) point source in the speckle halo that results from the interference of residual wavefront aberrations. To overcome this, differential imaging

techniques may be employed. If the speckle halo is reasonably constant in relation to the instrument system of reference, observations at two different sky rotation angles can be subtracted to reduce the speckle halo and reveal the (moving) point source. This technique is known as angular differential imaging (ADI) (Marois et al. 2006). A similar technique, Spectral Differential Imaging (SDI) (Racine et al. 1999) relies on the wavelength-dependent shift of the speckles. Images taken at different wavelengths and scaled with this shift are subtracted, again reducing the speckle background. A real point source will have a constant position which can then be detected as a movement in the shifted images.

These techniques do have limitations. ADI will not work if the speckle pattern changes by too much between the two observations. For SDI, several observations in different, narrow, wavelength ranges are needed. The limited photon flux in these narrow bands poses even higher requirements on the instrument sensitivity.

1.2.3 Polarimetry

Another differential technique offers a number of advantages: Polarimetry. As we know well from our own solar system, planets and circumstellar material reflect the light from the Sun. Through this scattering process, the light becomes partially linearly polarized. The degree of polarization can become high, up to 100% at 90° scattering. The light from the star, being thermal radiation, is largely unpolarized. Thus, an instrument that is sensitive to linearly polarized light and *in*sensitive to unpolarized light will be able to detect the light scattered by circumstellar matter. Isolating the linearly polarized light can be performed by subtracting two images taken through orthogonal linear polarizers: unpolarized light will be equally present in both images while linearly polarized light will vary between them.

Achieving high contrast is only one part of the attractiveness of employing polarimetry. The polarized light itself provides information on the scattering material. The scattering of light by particles substantially smaller than the wavelength of the scattered light is described by the Rayleigh approximation of the more general Mie scattering theory. The amount of light reflected through Rayleigh scattering depends on both the particle size and the wavelenghth of the scattered light. This means the particle size distribution of the scattering medium can be constrained by comparing the degree of polarization measured at different wavelengths.

For larger particles, laboratory measurements (e.g. Volten et al. 2005) and Mie scattering simulations (e.g. Haudebourg et al. 1999) can reveal how the polarization signature, in terms of wavelength and scattering angle, is influenced by the shape and the index of refraction of the particles. Comparing these data to real observations can then be used to e.g. differentiate between compact and more fluffy particles, and yield information on the chemical composition of the dust.

Finally, as illustrated by figures 1.3 & 1.4, the degree of polarization also depends heavily on the scattering angle. As a consequence, imaging polarimetry can yield insight in the 3D structure of complex circumstellar envelopes. An example of this is given in Chapter 5 of this thesis.

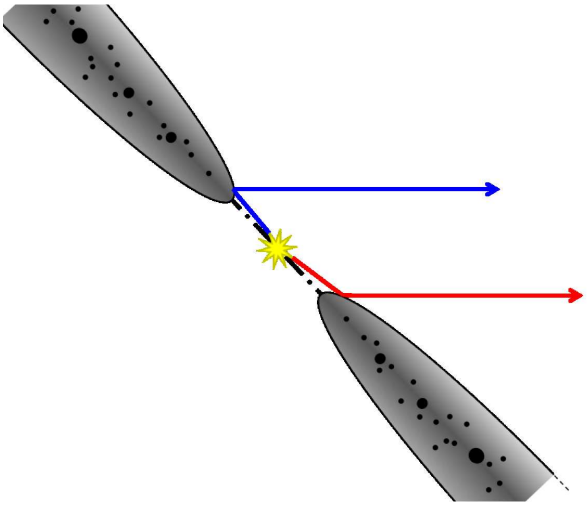

Figure 1.3: Forward (red) and backward (blue) scattering of starlight by a tilted circumstellar disk with an inner gap.

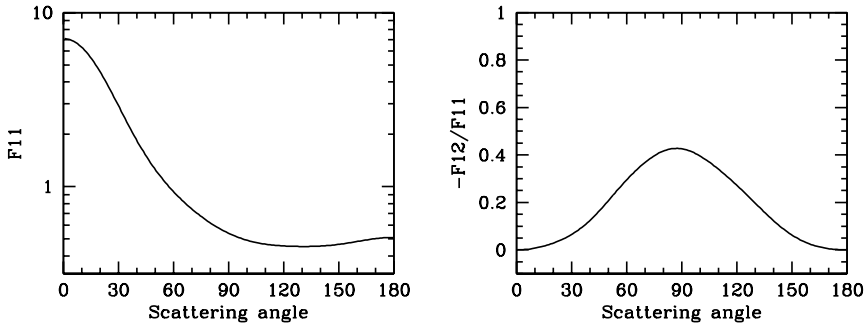

Figure 1.4: Intensity (left) and degree of polarization (right) as a function of scattering angle for a simulation of scattering by circumstellar dust particles. Image credit: M. Min.

A few groups have built aperture-integrated polarimeters, without imaging capability, to detect the polarization signatures of orbiting exoplanets (Hough et al. 2006, Wiktorowicz & Matthews 2008). The polarization sensitivities reached by this type of instrument can be very high, 10^{-6} has been published (Hough et al. 2006). But they rely on detecting a periodically varying polarization signal from an orbiting planet. This requires very high stability of the instrument and a very accurate way of removing time-variable background signals such as the sky-polarization. Although a claim has been made (Berdyugina et al. 2008), no planet detection using aperture-integrated polarimetry has so far been confirmed.

Imaging polarimetry offers a number of advantages, even though spreading the limited amount of photons over more pixels inherently reduces the maximum polarimetric sensitivity that can be reached. Most importantly, the spatial information helps us to determine the origin of any polarization signal detected: is it from a small point source or a flat background signal? This type of instrument is also very useful to study polarization from extended sources, such as disks, that have polarization structures that combine to a very small disk-integrated net polarization signal.

1.3 ExPo: The Extreme Polarimeter

The Extreme Polarimeter (ExPo), the subject of this thesis, has been developed to advance the imaging polarimetry technique and explore the science possibilities it offers. Polarimetry is a demanding technique, requiring great care in the instrument design. Reflections on mirrors and other asymmetrical optical configurations will always affect the polarization, making it difficult to reach high sensitivity. Instruments where polarimetry has been added as an afterthought (and there are a few) therefore often have limited performance (Potter et al. 2000, Kuhn et al. 2001, Apai et al. 2004, Perrin et al. 2004). The concept of ExPo is to focus exclusively on polarimetry and build an instrument that is fully optimized to do this. Hence the 'Extreme'. ExPo is also built as a flexible instrument, that can easily be modified or extended.

When combined with an AO system, ExPo will be able to reach a contrast of 10^{-8} at an angular separation of 1''. figure 1.5 presents simulated results that show the contribution of the various instrument components to achieving this contrast, demonstrating the added value of the polarimetry. Chapter 6 of this thesis will show this contrast is also reached with the real instrument.

1.4 ExPo science drivers

1.4.1 Circumstellar disks

Exploring protoplanetary disks, the birthplace of planets, already becomes possible at a contrast several orders of magnitude less than that required for direct observations of exoplanets. While a general understanding of disk evolution and planet formation is emerging (e.g. Williams & Cieza 2011), many aspects of this process remain unclear. In particular, the growth of km-sized planetesimals from m-sized rocks is poorly understood (e.g. Blum & Wurm 2008). Most planet formation models predict that the abundance and mass of the m-sized boulders will result in frequent collisions with sufficient energy to shatter them, forming a barrier to further growth. The sensitivity of polarimetry to dust grain size, index of refraction and shape is a powerful diagnostic of at least the precursor to this stage of evolution, and may thus help in refining the current planet formation models.

Imaging of protoplanetary disks may also yield information on planet formation in a different way: Asymmetries such as spiral arms have been observed in disks

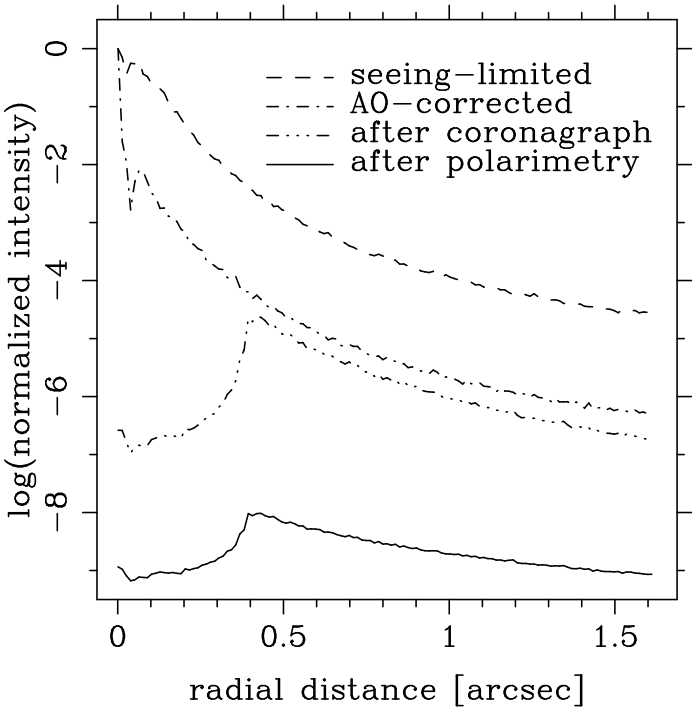

Figure 1.5: Simulation showing the contribution of various instrument elements on the contrast provided by an instrument with the polarimetric sensitivity of ExPo, in combination with an AO and a classical Lyot coronagraph. The simulation is based on the broadband flux from a $M_V = 0$ star through a 4.2-m telescope, observed with an exposure time of 10000 seconds. A Kolmogorov spectrum has been used to simulate the atmospheric seeing, with a ratio between the mirror diameter and the seeing Fried parameter (D/r_0) of 28.0. The AO system's 76 actuators remove the first 76 Zernike polynomials from the wavefront error. The coronagraph has an inner working angle of 0.4″. Image credit: C.U. Keller.

(Fukagawa et al. 2004, chapter 4 of this thesis). These asymmetries may be the hallmark of planets either fully formed in cleared regions of the disk or still forming and embedded in the disk. Detailed observations of the disks and, eventually, their dynamics over time, can provide more insight in this stage of evolution.

Even without planets, protoplanetary disks are of course also interesting in themselves. The ability of polarimetry to probe the dust grain size at different locations in the disk can further our knowledge of the processes taking place during the early stages of disk evolution, such as the dust sedimentation towards the midplane, dust transport through the disk towards and accretion onto the star and possibly the clearing of the inner region of the disk through photoevaporation and radiation pressure. Polarimetry has been used in this context by Pinte et al. (2007) to infer the dust stratification in the disk of GG Tau.

Finally, the contrast provided by imaging polarimetry also allows studying the end point of circumstellar disk evolution, debris disks. An example of this are the observations by Graham et al. (2005) of the disk around AU Microscopii, where polarimetry was used to constrain the dust grain size distribution.

1.4.2 Dust shells around evolved stars

Asymptotic Giant Branch (AGB) stars are low to intermediate mass (0.6 – 10 $M_{\odot}$) stars in a late stage of their evolution. These stars undergo rapid changes in the fusion processes taking place in their interiors, resulting in high mass loss rates. Evolved stars such as post-AGB stars may literally blow away their outer atmospheres, forming shells of dust and gas as a precursor to extended planetary nebulae. The structure of the shells and the composition of the dust in them form clues to the processes occurring in this stage of stellar evolution. As with the circumstellar disks, the shells themselves are faint but scatter the light from the star which becomes linearly polarized in the process. Imaging polarimetry is therefore a powerful tool to study these shells. Chapter 5 of this thesis is dedicated to the observation of an enigmatic variable evolved star (Mira), with some preliminary conclusions drawn on the structure of the outflow and the grain size distribution of the dust. Mira has already been studied extensively (an overview is given by Karovska 1999) and our observations clearly demonstrate the added value of imaging polarimetry.

1.4.3 Exoplanets

As exoplanets also scatter starlight, imaging polarimetry is a powerful technique to directly observe exoplanets. As chapter 6 will demonstrate, the sensitivity of ExPo is approaching the level where this becomes possible. But getting a signal at the 10^{-9} level above the photon noise requires extreme amounts of photons. On the William Herschel Telescope, with its 4.2-m aperture, this would require exposure times much longer than a single night. Besides a bigger telescope, the resolution and stability provided by an extreme AO system and the additional contrast offered by a good coronagraph system is needed to achieve a contrast of 10^{-9}.

A custom, polarimetry-friendly AO system for ExPo is in fact currently being developed. In the mean time, ExPo is an excellent test bed for further developing imaging polarimetry and increasing the sensitivity and contrast that can be achieved to a level where direct imaging of exoplanets is feasible. In combination with our exoplanet laboratory simulator (chapter 3 of this thesis), the instrument, the observation strategies and the data reduction techniques can be refined. The experience gained by this will be very valuable for future exoplanet imaging and characterization instruments that employ polarimetry, such as Sphere/ZIMPOL and EPICS.

1.5 The development of ExPo

ExPo as a dedicated night-time imaging polarimeter was proposed by Christoph Keller in 2005, and funding was obtained to develop it. Two PhD students, one to design and build the instrument (the author) and one to develop the data reduction techniques (Hector Canovas) were hired in addition to a postdoc (Sandra Jeffers).

At the start of the project (early 2007), a simple prototype was built to evaluate various design options available. Tradeoff studies on the camera and the polarization beamsplitting and modulating components were performed and the design was finalized in early 2008. The instrument was built and assembled during the summer and saw first light in October 2008.

Five observing runs have been conducted with ExPo so far, all of them at the William Herschel Telescope on La Palma. The first commissioning run was very successful with all components working as required and many science-grade observations of protoplanetary disks made, including a disk that has not been imaged before (V1685Cyg). The short second run was lost due to bad weather. Our third run, dedicated to a survey of protoplanetary disks around young stars was very successful. Many disks were observed, again including some directly imaged for the first time (including MWC361, HD203024, V628Cas, COUP932). This thesis presents results on two targets from this run, AB Aurigae and Mira, one of a few evolved stars also targeted during this run. Our fourth run was dedicated to AGB stars but included a few targets of opportunity. Again, many high-quality science observations were made, including those of Venus that are the subject of chapter 7. A fifth run was intended to study comet 103/P Hartley, but the two nights were again lost to bad weather. A proposal for a new run to study Active Galactic Nuclei has just been submitted.

Based on experience from solar imaging polarimetry, it was expected that a polarization sensitivity of 10^{-5} would be reachable. Compared with solar polarimetry, the night time polarimetry has much less photons available, requiring longer exposure times to get a polarization signal above the photon noise. On sky we have typically worked with accumulated exposure times of 10 - 30 minutes, in which a polarization sensitivity of 10^{-4} can be achieved. As this thesis will show (chapter 4), the instrument performance is in fact photon noise limited, meaning that a higher sensitivity can be reached with longer exposures.

On the William Herschel Telescope, ExPo is not able to directly image exoplanets. As will be shown in chapter 6, this is not really a limitation of the instrument, but is the result of the lack of an Adaptive Optics system and the limited angular resolution and light-gathering power provided by the 4.2–m main mirror.

ExPo is not the only imaging polarimeter currently in existence or under development. The HiCIAO instrument on the Subaru telescope includes an imaging polarimetry mode (Hodapp et al. 2008), and the combination of imaging polarimetry in the near infrared, a high-performance Adaptive Optics (AO) system and a good coronagraph have yielded spectacular results (Hashimoto et al. 2011). Two instruments including imaging polarimetry that will become operational in the next few

years are Sphere-ZIMPOL (Thalmann et al. 2008) and the Gemini Planet Imager (GPI) (Perrin et al. 2010). GPI is somewhat different in that the image is first sampled in the spatial domain by a microlens array, after which the polarimetry is performed. This has the advantage of removing any spatially varying (optical) effects that may degrade the polarimetric performance. ExPo is unique in that it is dedicated to developing imaging polarimetry alone and in being available today. Another difference is that ExPo has expressly been limited to visible wavelengths, where scattering polarization is stronger.

1.6 Outlook

This thesis documents the beginning, but certainly not the end of the development of ExPo. Two projects are currently underway to extend and improve the instrument. First of all a custom-designed AO system is being developed. Apart from providing higher spatial resolution, the AO system will allow more efficient use of the ExPo coronagraph resulting in higher contrasts. By designing our own AO system, we can minimize the effects on the polarization.

A second project is the development of a spectro-polarimetric integral field unit (IFU) for ExPo. This system will allow simultaneous imaging polarimetry for a range of wavelengths, or, phrased differently, allow the taking of polarized spectra for a range of spatial locations in the image. This is very attractive because many scattering effects, e.g. by dust particles, have wavelength-dependent behavior. Obtaining polarimetry at different wavelengths simultaneously removes instrument stability issues and the effects of time-variability of the atmospheric seeing, which currently hampers our filter-based efforts at comparative polarimetry at different wavelengths. The IFU will likely employ a microlens array to first sample the image plane, after which the light of the sub-apertures can be split according to wavelength and polarization.

These projects should also be seen against the backdrop of the development of EPICS, the exoplanet imaging and characterization instrument under development for the European Extremely Large Telescope (Kasper et al. 2010). This instrument will include an imaging polarimeter arm (EPOL) which is being developed by our group (Keller et al. 2010). The design of EPOL is strongly influenced by the experience gained with ExPo and ExPo will be available as a testbed for new concepts that may be developed for this instrument.

1.7 Thesis overview

The next chapter is an early paper published in the Proceeding of the SPIE presenting the design of ExPo. It describes the science rationale, discusses design tradeoffs and includes the prototyping results.

As ExPo is an instrument that is constantly being developed further, it is shipped back to Utrecht between observation runs and assembled in our optical lab for testing and improvements. This can not be done at the telescope as telescope time is scarce and expensive. Instead, an exoplanet and circumstellar disk laboratory simulator has been developed to test the instrument. The exoplanet simulator was largely built by Nick Miesen, a Master's student whom the author helped at the start of his PhD. A Bachelor student, Lars Einarsen, later added a simulation of a circumstellar disk under my supervision. Chapter 3 documents the design, testing and test results of these simulator parts.

A key part of the thesis is chapter 4, which summarizes the key elements of the final instrument design and explains the methods used to process and calibrate our observations. Performance results gathered during the first science runs are also reported here. As a sample science result, this paper also presents our observations of AB Aurigae in which we detect the spiral arms observed earlier with Hubble (Grady et al. 1999) and the CIAO coronagraphic imager of the 8.2–m Subaru AO-assisted telescope (Fukagawa et al. 2004).

Chapter 5 is a paper dedicated to a specific science target: the complex Mira variable binary system. Detailed structures are found in the dust envelope in this system and to our knowledge, our observations are the first of this system with this level of detail in the optical. The structures observed are compared to a numerical model of the density distribution and dust composition and its scattering behavior, and we make some preliminary conclusions about the topology and inclination of the bipolar outflow from the Mira A primary, an AGB star.

In chapter 6, results of a laboratory experiment, in which the contrast limit of the instrument was tested, are presented. The experiment mimics the performance of ExPo when used with an AO-system (or in space) to detect exoplanets. A contrast of 10^{-8} has been reached at 1'' from the star, approaching the contrast required for exoplanet detection. This is a result that we believe can still be improved on.

The final chapter presents imaging polarimetry of an actual planet, albeit one in our own solar system: We have observed Venus through a range of broad- and narrowband filters and believe to have discovered an unknown phenomenon: polarized rings in the Venusian atmosphere.

1.8 A first peek

As a conclusion to this introduction, and a warm-up to the rest of the thesis, we offer a first glimpse of some of the most interesting ExPo observations so far. Each of the targets is the subject of dedicated science papers currently in preparation, and no attempt at any scientific interpretation is done here.

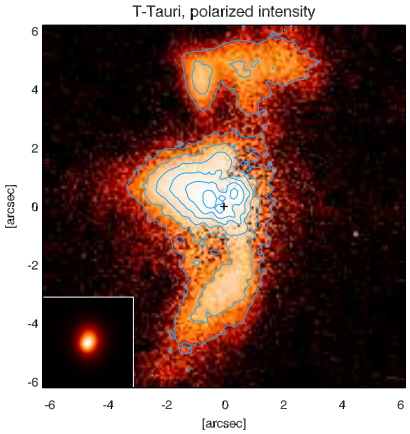

Figure 1.6: T-Tauri, the well-known prototype of this class of newborn stars, embedded in its extensive and highly assymetric nebula. The background image shows the polarized intensity, scaled logarithmically. The '+' marks the star. The polarized intensity is traced by contours, spaced at logarithmic intervals and boxcar-smoothed with a width of 3 pixels. The insert at the lower left shows the intensity image at the same geometrical scale.

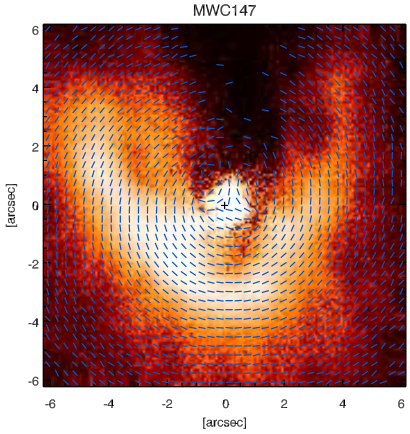

Figure 1.7: MWC147, a Herbig Ae/Be object, is another young star surrounded by a circumstellar cloud from which it formed and is still accreting material. The background image shows the histogram-equalized polarized intensity. This is overlaid with vectors mapping the polarization orientation. The vectors have not been scaled. The '+' marks the star position.

1.9 References

Apai, D., Pascucci, I., Wang, H. et al. 2004, Star Formation at High Angular Resolution. Burton, M. G., Jayawardhana, R. & Bourke, T. L. Eds. IAU Symposium vol. 221pp. 307

Berdyugina, S. V., Berdyugin, A. V., Fluri, D. M. et al. 2008, Astrophys. J. vol. 673 pp. L83

Blum, J., Wurm, G. 2008, Astron. Astrophys. vol. 46 pp. 21

Fukagawa, M., Hayashi, M., Tamura, M. et al. 2004, Astrophys. J. vol. 605 pp. L53

Grady, C. A., Woodgate, B., Bruhweiler, F. C. et al. 1999, Astrophys. J. vol. 523 pp. L151

Guyon, O. 2003, Astron. Astrophys. vol. 404 pp. 379

Hashimoto, J., Tamura, M., Muto, T. et al. 2011, Astrophys. J. vol. 729 pp. L17

Hathi, N. P., Malhotra, S. & Rhoads, J. E. 2007, Astrophys. J. vol. 673 pp. 686

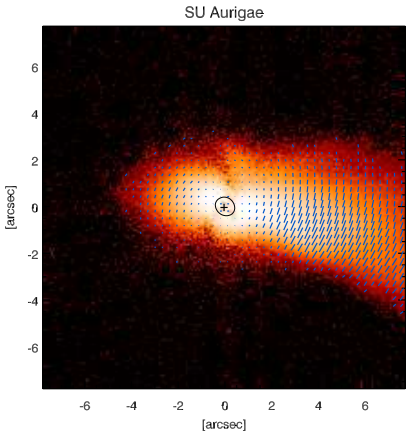

Figure 1.8: The T-Tauri star SU Aurigae has a strong jet-like feature. Again the image is of the polarized intensity (histogram-equalized). The vectors have been scaled with the degree of polarization. The small oval is the intensity contour at half its peak value.

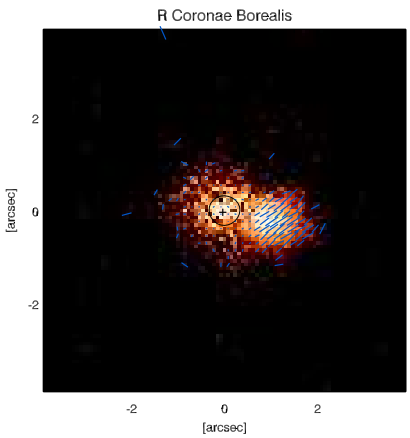

Figure 1.9: The enigmatic star R Coronae Borealis is an irregular variable. The star is currently in a dramatic minimum, its intensity having decreased by no less than 9 magnitudes. This is attributed to a dust cloud emitted in our direction. This eclipse allows us to see another cloud, at right, which shows up clearly as a linearly polarized blob in this ExPo polarized intensity image.

Haudebourg, V., Cabane, M. & Levasseur-Regourd, A. -C. 1999, Physics and Chemistry of the Earth, vol. 24 pp. 603

Hodapp, K. W., Suzuki, R., Tamura, M. et al 2008, Ground-based and Airborne Instrumentation for Astronomy II – Proceedings of the SPIE. Edited by McLean, Ian S.; Casali, Mark M. Proceedings of the SPIE, vol. 7014, pp. 701419

Hough, J. H., Lucas, P. W., Bailey, J. A. et al 2006, Publ. Astron. Soc. Pac. vol. 118 pp. 1302

Karovska, M. 1999, Asymptotic Giant Branch Stars - IAU Symposium vol. 191 pp. 139

Kasper, M., Beuzit, J.-L., Verinaud, C. et al. 2010, Ground-based and Airborne Instrumentation for Astronomy III – Proceedings of the SPIE. Edited by McLean, vol. 7735 pp. 81

Keller, C. U., Schmid, H. M., Venema, L. B. et al. 2010, Ground-based and Airborne Instrumentation for Astronomy III – Proceedings of the SPIE. Edited by McLean, vol. 7735 pp. 212

Kuhn, J. R., Potter, D. & Parise, B. 2001, Astrophys. J. vol. 553 pp. L189

Levine, M., Lisman, D., Shaklan, S. et al. 2009 arXiv vol. 0911 pp. 3200

Marois, C., Lafrenière, D., Doyon, R. et al. 2006, Astrophys. J. vol. 641, pp. 556

Marois, C., Macintosh, B., Barman, T. et al. 2008, Science, vol. 322, pp. 1348

Mawet, D., Riaud, P., Absil, O. et al. 2005, Astrophys. J. vol. 633 pp. 1191

Perrin, M. D., Graham, J. R., Kalas, P. et al. 2004, Science vol. 303 pp. 1345

Perrin, M. D., Graham, J. R., Larkin, J., et al. 2010, Adaptive Optics Systems II. Edited by Ellerbroek. Proceedings of the SPIE, vol. 7736 pp. 192

Potter, D. E., Close, L. M., Roddier, F. et al. 2000, Astrophys. J. vol. 540 pp. 422

Racine, R., Walker, G. A. H., Nadeau, D. et al. 1999, Publ. Astron. Soc. Pac. vol. 111 pp. 587

Schneider, J. 2010, The Extrasolar Planets Encyclopaedia (www.http://exoplanet.eu/catalog.php)

Suzuki, R., Kudo, T., Hashimoto, J. et al. 2010, Ground-based and Airborne Instrumentation for Astronomy III – Proceedings of the SPIE. Edited by McLean, vol. 7735 pp. 101

Swartlander, G. A., Ford, E. L., Abdul-Malik, R. S. et al. 2008, Optics Express vol. 16 pp. 10200

Thalmann, C., Schmid, H.-M., Boccaletti, A. et al. 2008, Ground-based and Airborne Instrumentation for Astronomy II. Edited by McLean, Ian S.; Casali, Mark M. Proceedings of the SPIE, vol. 7014, pp. 112

Trauger, J. T., Traub, W. A. 2007, Nature vol. 446 pp. 771

Volten, H., Munoz, O., Hovenier, J.W. et al. 2005, Journal of Quantitative Spectroscopy & Radiative Transfer vol. 90 pp. 191

Wiktorowicz, S. J., Matthews, K. 2008, Publ. Astron. Soc. Pac. vol. 120 pp. 1282

Williams, J. P. & Cieza L. A. 2011, arXiv eprint vol. 1103 pp. 556

Chapter 2

The Extreme Polarimeter: Design of a sensitive imaging polarimeter

M. Rodenhuis, H. Canovas, S.V. Jeffers, and C.U. Keller[1]

Abstract

The Extreme Polarimeter (ExPo) is approaching its first deployment at the 4.2 m William Herschel Telescope at La Palma. This imaging polarimeter, developed at the Astronomical Institute of Utrecht University, aims to study circumstellar material at a contrast ratio with the central star of 10^{-9}. Working at visible wavelengths, it will provide an inner working angle down to 0.5″ and a field of view of 20″ diameter. ExPo employs a dual beam-exchange technique based on polarimeter designs for solar studies. A partially transmitting coronagraph mask placed in the first focus reduces the light of the star. The beam is modulated using three ferro-electric liquid crystals in a Pancharatnam configuration, then split in a polarizing beamsplitter. Both beams are re-imaged onto the same Electron-Multiplying CCD camera. We present the design of the ExPo instrument, highlighting the elements that are critical to the polarimetric performance. Some prototype laboratory experiments demonstrating the instrument concept are discussed. These have been performed using our realistic exoplanet laboratory simulator.

[1]published in the proceedings of the SPIE, 2008

2.1 Introduction

Over the last decade, over 500 exoplanets have been discovered, mostly using precise spectroscopic measurement of the Doppler effect caused by their motions. The information that can be gained about the discovered planets using this technique is however limited. To further characterize exoplanets we must be able to directly detect light from them and separate it from the light of the central star.

Imaging polarimetry holds the promise to do exactly this. While the light from the star is unpolarized, light scattered by a planet surface or atmosphere will exhibit linear polarization. For Jupiter-like planets, the ratio of polarized light to the intensity of the star is 1×10^{-9} (Stam et al. 2004). Dual beam-exchange polarimetry, developed for solar studies, has demonstrated sensitivities in excess of 1×10^{-5} (Keller 1996). The combination of this technique with adaptive optics (AO) and a coronagraph will reduce the stellar intensity by several more orders of magnitude to achieve the required contrast ratio.

A broader and less demanding application of imaging polarimetry is studies of circumstellar environments in general. At contrast ratios many orders of magnitude less than that needed for exoplanet characterization, the sensitivity and spatial resolution will be well suited for detailed studies of circumstellar disks. Of particular interest is the investigation of dust grain distributions in disks. Studies of these distributions are fundamental to increasing our knowledge about disk dynamics and planetary system evolution. Even where exoplanets cannot be imaged directly, high-resolution polarimetry has the potential to image density fluctuations, gaps and waves in the inner parts of disks that may be caused by orbiting planets.

Several efforts are currently under way to develop imaging polarimeters with these applications in mind. The SPHERE/ZIMPOL instrument being developed for ESOs Very Large Telescope (VLT) in Chile will include an imaging polarimeter, as will the EPICS instrument targeted for the future European Extremely Large Telescope. The experimental astrophysics group at the Utrecht Astronomical Institute is building a pathfinder for these instruments, named the Extreme Polarimeter (ExPo). The first concepts for this instrument have been presented by Keller (2006). ExPo aims to achieve a polarimetric sensitivity of 10^{-5} while providing a field of view of around 20″. The instrument will operate in the visible wavelength range between 450 and 900 nm. The instrument will initially be deployed at the William Herschel Telescope (WHT) at La Palma, placed in the Nasmyth focus. First light is foreseen for the second half of 2008. ExPo will initially be used without an adaptive optics system; this will be included at a later stage. In the future, using the instrument at other telescopes or placing it in the WHT Cassegrain focus is also possible.

2.2 The ExPo design

2.2.1 Design objectives

As ExPo is an experimental instrument, its design is modular and flexible, allowing easy and fast exchange of its components. The current design is intended to evolve over the next two years; the ultimate aim of the instrument is to achieve a contrast ratio better than 10^{-8} in the visible at 1″ from the central star. The major specifications of the current ExPo design are listed in table 2.1 below.

Table 2.1: ExPo design specifications

Field of view:	20″
Inner working angle:	$< 1''$
Contrast ratio:	$< 10^{-8}$
Polarimetric sensitivity:	$< 10^{-5}$
Wavelength range:	450 – 900 nm

2.2.2 ExPo polarimeter design

While ExPo is being built for night-time applications, its design borrows heavily from advances in instrumentation for solar studies made over the last decade. Using the dual beam-exchange technique, solar polarimetry has been demonstrated to reach sensitivities of better than 1×10^{-5} of the total intensity (Keller 1996). The dual beam-exchange technique uses a rotating or switchable retarder to modulate the polarization in the incoming beam and a polarizing beamsplitting element to split the beam into its orthogonal polarization states (Semel et al. 1993). These two beams can then be recorded simultaneously.

The advantage of modulating the polarization is twofold: first, the instrument is significantly less sensitive to any instrument-induced polarization downstream of the modulator: The filtering of the polarization state to which the instrument is sensitive takes place at the modulation element. Second, any differences in transmission between the two beams are cancelled due to the swapping of the beams.

Our instrument uses three Ferro-electric Liquid Crystals (FLCs) as the modulating element. The liquid crystals act as a half-wave plate of which the fast axis can be rotated by 45 degrees by applying a voltage. The three FLCs are combined in a Pancharatnam configuration to provide achromatic performance in the 450 – 900 nm wavelength range (Pancharatnam 1955). A key advantage of the FLC is the fast switching speed, allowing modulation frequencies in excess of 1 kHz. Using fast modulation ensures that atmospheric seeing changes little during each exposure set. In practice, the modulation frequency is limited by the maximum camera frame rate to about 35 Hz.

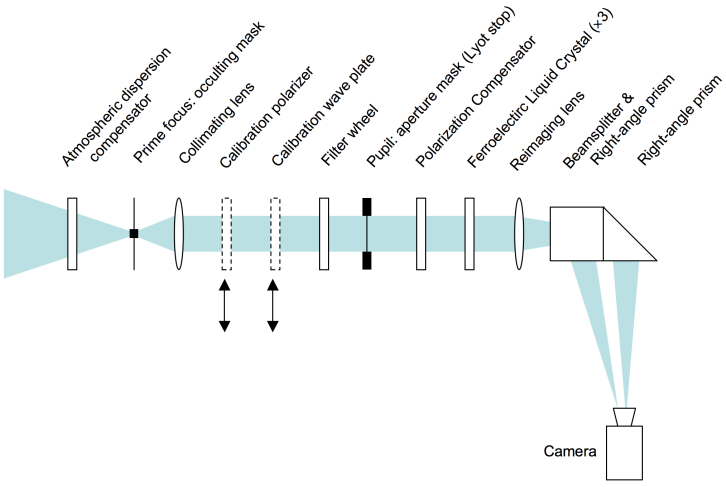

Figure 2.1: Schematic diagram showing the different ExPo components. The occulting mask in the prime focus and the aperture mask in the pupil image together form the coronagraph that suppresses the light from the star. The core of the polarimeter consists of the Ferroelectric Liquid Crystals (FLC) acting as the modulating element and the polarizing beamsplitter that splits the beam into its orthogonal polarization components.

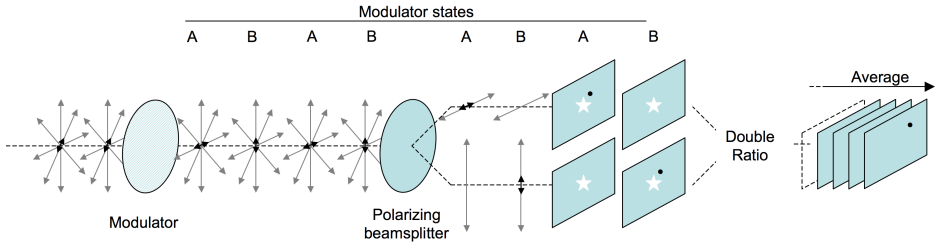

Figure 2.2: Diagram demonstrating the dual beam-exchange technique being used to detect an exoplanet. The modulator alternately aligns the polarization orientation of interest with two orthogonal directions that are then separated by the polarizing beamsplitter. Both beams are imaged simultaneously by a camera. Subtracting the resulting images cancels out the large unpolarized signal while the (partially) polarized planet signal remains.

The beamsplitting element is a polarizing thin-film beamsplitter cube. Polarizing cube beamsplitters have the disadvantage that the extinction ratio, the ratio between the suppressed polarization direction and the transmitted one, is much lower in

the reflected beam than in the beam passing straight through the cube. On ExPo, the extinction ratio in the reflected beam is on the order of 1:30. This is however outweighed by the fact that beamsplitting cubes do not suffer from chromatic splitting and do not introduce the crystal aberrations of splitting elements such as Wollaston prisms.

Immediately after exiting the beamsplitter, the two beams are projected onto the camera using two right angle prisms. Both prisms are rotated by a few degrees to achieve this as is shown in figure 2.3 below.

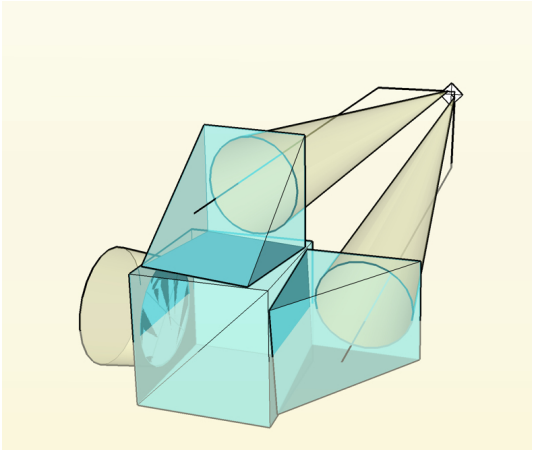

Figure 2.3: After the beamsplitter, the beams are projected onto the camera image sensor by slightly rotating the two right-angle prisms.

By projecting both beams on the same CCD, the camera will take simultaneous exposures of both orthogonal polarization states. By using a single camera, we avoid having to perform the complex synchronization required when using separate cameras for each beam. If the beams are not imaged at exactly the same time, combining the two images will introduce error signals that reduce the sensitivity.

As the Nasmyth mirror of the telescope introduces polarization, this must be compensated before the modulating element. We use a glass plate that can be tilted to remove the unwanted polarization. The tilting mechanism can itself be rotated about the optical axis to adjust for changing telescope elevation as it tracks a target across the sky. The polarization compensator is placed after the Lyot stop as it introduces a slight, variable beam displacement. Finally we have included the possibility to insert both a calibration polarizer and retarder into the beam.

2.2.3 ExPo optical design

The ExPo optical design has been kept as simple as possible. Every additional optical element adds potential for ghosts and systematic polarization effects. Thus a classic

two-lens configuration was chosen with a first collimating lens after the prime focus and a second re-imaging lens positioned to create a telecentric beam on the camera.

The choice of lenses was restricted by the need to achieve a field of view of at least 20″. Slow lenses are preferred to limit aberrations and to reduce the angle of the two separate beams directed onto the camera. Finally, the collimated beam width is limited to about 35 mm due to the difficulty of obtaining larger liquid crystal modulators, filters etc. This has resulted in the selection of two 1.5-inch diameter lenses with focal lengths of 280 and 250 mm for the first and second lens, respectively.

In an early version of the design we tried to position the second lens after the polarizing beamsplitter assembly. This would then be a large-diameter lens where the two beams would pass through the lens at different positions near the lens edge. An advantage of this idea was the very small angles of the two beams required to project both onto the camera CCD. However, analysis of the design showed that the aberrations near the lens edges were too big. Thus, the re-imaging lens is now placed just in front of the beamsplitter, further adding to the need to use a long focal-length lens.

A Lyot stop is placed in the pupil image between the two lenses. The mask design is based on our own modelling and analysis and work performed for OSCA, the Optimized Stellar Coronagraph for Adaptive optics, developed for the William Herschel Telescope (Thompson et al. 2003). The mask outer diameter is sized at 90% of the projected primary mirror while the inner diameter is at 110% of the secondary. The four spiders holding the secondary are also masked, the masks being 6 times oversized.

A coronagraph mask is placed in the telescope prime focus to achieve an initial reduction of the stellar flux. The mask has a number of positions with different spot sizes, ranging from 0.5″ to 5″. We have a set of masks with different transmission values (including zero) for the central spot. Our data reduction technique will make use of the transmitted fraction of the starlight (see Keller 2006).

Finally, the instrument includes a 12-position filter wheel. We would prefer to have this after the Lyot stop but due to space limitations it is placed just before the Lyot stop.

2.2.4 Atmospheric dispersion compensator

A key component of ExPo, the Atmospheric Dispersion Compensator (ADC), is mounted in front of the prime focus. The longitudinal ADC design is based on Avila et al. (1996) and consists of two thin wedge prisms where the first can be translated to correct for different amounts of dispersion. For a sensitive polarimeter, this configuration offers a number of advantages:

- If mounted directly to an alt-azimuth telescope, only the translation of the first prism needs to be adjustable.
- The orientation of any polarization induced by the ADC will be fixed in the telescope coordinate system.

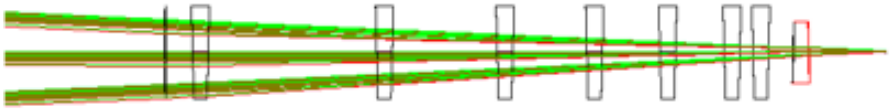

Figure 2.4: ZEMAX plot of the ExPo atmospheric dispersion compensator. The first prism is shown at different positions compensating (from left to right) for zenith angles of 60, 50, 40, 30, 20, 10 and 5 degrees. The rightmost prism is the second, fixed prism.

- Wedge angles can be chosen such that there are no parallel surfaces perpendicular to the optical axis. Any ghost images will lie outside the field of view.
- Fused silica can be used for the ADC prisms. This material has low intrinsic and stress-induced birefringence.

Our design uses two 3-inch fused silica prisms, each with a wedge angle of 3 degrees and a thickness of 0.5 inch. The plot below shows the operation of the ADC at different telescope elevations:

The whole ADC assembly will be bolted directly to the WHT Nasmyth derotator, which will be controlled such that it rotates with the elevation of the telescope.

2.2.5 The ExPo camera

The dual-beam exchange technique used for ExPo requires a camera that must be both highly sensitive, as the exposure times are short, and must allow high frame rates to achieve the fast modulation. The camera chosen for ExPo is an Andor iXon+ Electron-Multiplying CCD (EMCCD) camera. The EMCCD technology allows us to minimize the readout noise. The frame-transfer EMCCD chip has 512×512 active pixels and can maintain frame rates up to 35 Hz. Using an external time source, the camera is synchronized with the liquid crystal modulator.

2.2.6 Mechanical design

The mechanical design uses commercially available mounts for many of the ExPo optical components. The instrument includes components, such as the Lyot stop and the polarization compensator, that will be continually adjusted using active control. Other components may be repositioned many times during measurements. Switching between different spot sizes on the occulting mask, changing the FLC orientation, inserting calibration optics and adjusting the camera focus are examples of this. To provide easy reconfiguration with sufficient repeatability and accuracy, motorized stages, controlled from a central computer are used for all these components. For the

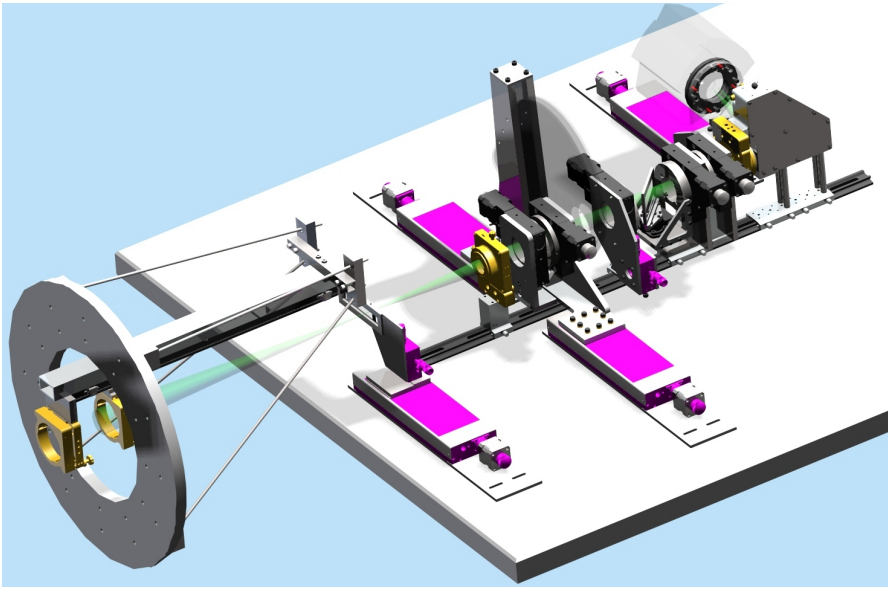

Figure 2.5: 3D rendering of the ExPo mechanical design. The atmospheric dispersion compensator is shown mounted to the telescope derotator flange at the bottom left. Space is tight; this is especially the case between the Lyot stop and the beamsplitter assembly, the top right half of the instrument.

rotation adjustments, we use stages from Thorlabs that provide arcsecond resolution and about 100″ repeatability. The translation stages selected are also from Thorlabs and provide 150 mm travel at 2 μm repeatability accuracy.

The mount of the ADC to the telescope derotator flange and the assembly holding the beamsplitter and the adjustable right-angle prisms have been designed and produced at our in-house workshop. Various brackets to mount the other components along a stable optical rail are also manufactured locally. Figure 2.5 shows a CAD drawing of the instrument mounted on the optical table at the WHT Nasmyth focus. Most of the components are mounted along an optical rail. The atmospheric dispersion corrector is shown mounted to the telescopes derotator flange.

2.2.7 Control software

Software has been developed to allow integrated control of the ExPo camera and motion system. This runs on a standard industrial PC that includes a 1TB storage system where the large number of acquired frames is recorded. A number of ExPo mechanisms have closed loop control:

- Guiding errors are fed back to the telescope control system to keep the star image under the occulting mask. This is done by continuous comparison of

the intensity in four quadrants around the mask centre in the live image stream from the camera.

- The polarization compensator and the Lyot stop in the pupil are rotated about the optical axis to account for the changing pupil rotation as the telescope tracks the target over the sky.

- The tilt of the polarization compensator glass plate is controlled by calculating the remaining instrumental polarization from two subsequent frames (A and B), representing the different modulator states:

$$p = (A - B)/(A + B) \tag{2.1}$$

  The tilt is adjusted to minimize p.

- The Atmospheric Dispersion Compensator rotation is fixed to the telescope elevation. This is done by mounting the ADC on the telescope derotator flange.

- The translation of the first ADC prism is controlled based on the telescope elevation.

Azimuth and Elevation angle corrections are input to the telescope control system at the same frequency as the frame rate, based on a running average over five previous frames. The other loops have lower update rates, mostly running at one tenth of the frame rate.

2.3 Laboratory concept demonstration

During the development of ExPo, a prototype has been used in our optical lab to investigate some basic design concepts. The testing has been done using a simulation of a 0^{th} magnitude star accompanied by a planet at 1″ separation. The planet is partially polarized and the planet intensity can be adjusted from 10^{-3} of the star intensity down to 10^{-9}. The setup includes a simulation of 1″ atmospheric seeing. The exoplanet simulator is described in detail by Jeffers et al. (2008).

The prototype used for these experiments is currently much less sophisticated than the final instrument. First of all it does not include an occulting mask at present. The beamsplitting element has a narrower wavelength range (450 – 680 nm) and a single chromatic liquid crystal modulator is used. Furthermore we have so far used a standard CCD camera for our measurements. This means the performance we can achieve is currently nowhere near that foreseen for the final instrument. The prototype experiments are, however, very useful for testing the instrument concept and investigating problems that limit the performance.

A simple test scenario is one where the effects of atmospheric seeing are temporarily left out. Figure 2.6 shows detection of a planet at the 10^{-5} level. Here our

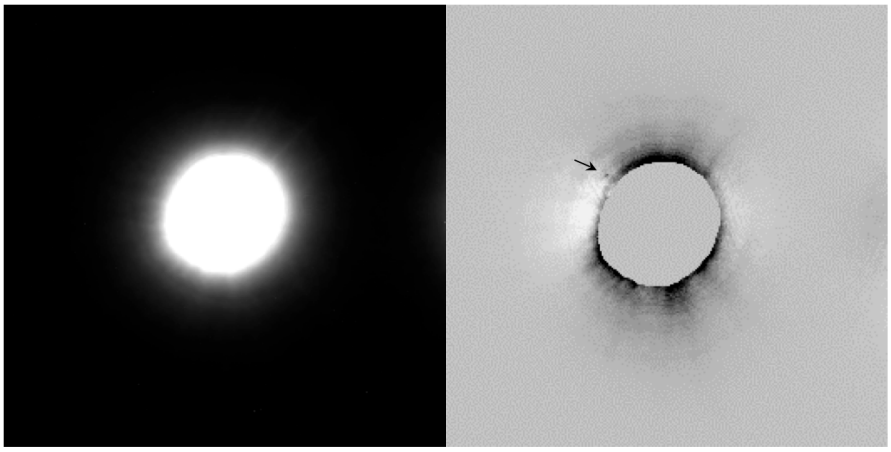

Figure 2.6: Demonstration of polarimetry in a simulation without atmospheric seeing effects: On the left is the intensity image (one of the two beams). On the right is the polarimetry image. The contrast ratio of the planet and star intensities is 1.1×10^{-5}. The planet can just be seen close to the upper left edge of what looks like the limb of the star, indicated by an arrow. In fact the central grey area is due to overexposure of the star. This image is the result of a simple subtraction of the two modulated beams, averaged over 1000 frames.

sensitivity is due exclusively to the polarimetry as no occulting mask is used. The star is overexposing a large part of the image.

The figure demonstrates that remaining polarization in the starlight complicates planet detection. This remaining polarization is caused by systematic errors in the instrument such as insufficient compensation of the polarization induced by the simulated third (Nasmyth) telescope mirror and polarization-sensitive aberrations in the two beams. Overcoming this remaining polarization is the major challenge for an imaging polarimeter intended for exoplanet detection.

As our instrument will initially be used without an adaptive optics system, a major part of our efforts are directed towards developing polarimetry techniques that can be used even when atmospheric seeing is present. The dual beam-exchange concept of the instrument is fundamental to performing imaging polarimetry under these circumstances. Combining images of both beams taken simultaneously makes polarized sources show up even when the image is blurred by seeing. Modulating the beams takes care of flat-field effects in the two beams. The effects of atmospheric seeing decrease with increasing modulation frequency: The atmospheric transmission is more static in the shorter exposures. Data-reduction techniques can be used to further improve the image quality. We use the possibility to include atmospheric seeing effects in our exoplanet simulation to improve these techniques.

Figure 2.7 demonstrates the effect of the simulated atmospheric seeing. It shows the detection of a planet under 1″ seeing conditions without AO. The contrast level here is only 10^{-3}. The second image shows the polarized planet signal. This image

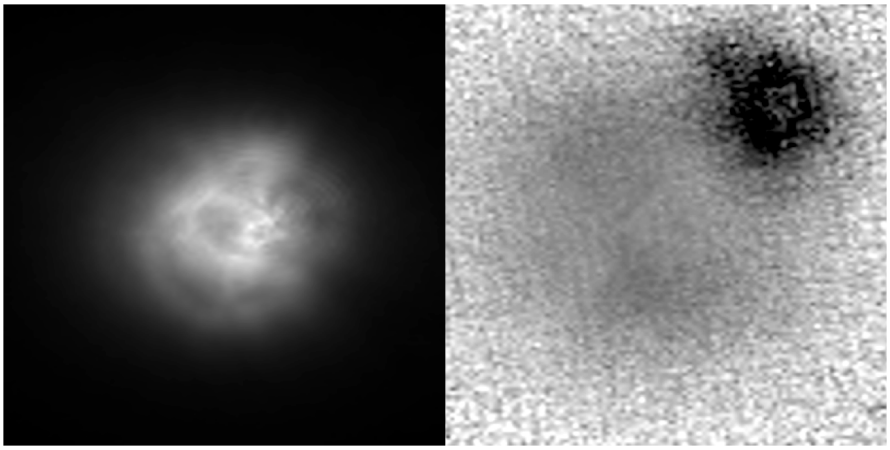

Figure 2.7: Detection of polarized source at the 10^{-3} level under 1″ seeing conditions: raw image of a single beam (left) and normalized image after the combination of the two beams (right).

is the normalized difference between the two sub-images of the two beams in each frame, averaged over a large number of frames.

2.4 Outlook

By the time that this contribution is published, the ExPo instrument will be fully assembled and tested with our laboratory exoplanet simulator. We expect to take the instrument to the William Herschel telescope for the first observing run in the second half of 2008 to perform science observations of circumstellar disks. The experimental nature and flexible and modular setup of ExPo will enable us to continuously improve it over the next two years. Within this period we expect to make marked improvements to the instrument performance and eventually reach a contrast ratio of 10^{-9}. This time is needed to understand the systematic, instrumental effects and develop appropriate mitigation strategies.

Our experience in developing and using this instrument will benefit the more capable polarimeter instruments SPHERE/ZIMPOL for the VLT and EPICS for the E-ELT. While the SPHERE development has progressed to the detailed design level, ExPo will be in operation several years before SPHERE. Techniques used for conducting observations, calibrations, and analyzing the data with ExPo will be applicable to SPHERE. As the design of EPICS is still at the conceptual stage, its design can build on the lessons learned from ExPo over the coming years.

2.5 References

Avila, G., Rupprecht, G. & Beckers, J.M. 1996, Ground-based and Airborne Instrumentation for Astronomy II. Edited by McLean. Vol. 2871 pp. 1135

Jeffers, S.V., Miesen, N., Rodenhuis, M. et al. 2008, Ground-based and Airborne Instrumentation for Astronomy II. Edited by McLean. Vol. 7014 pp. 239

Keller, C.U. 1996, Solar Physics vol. 164 pp. 243

Keller, C.U. 2006, Ground-based and Airborne Instrumentation for Astronomy II. Edited by McLean. Vol. 6269 pp. 26

Pancharatnam, S. 1955, Memoir no. 71 of the Raman research institute, Bangalore, pp. 308

Semel, M., Donati, J.-F., & Rees, D.E. 1993, Astron. Astrophys. vol. 278 pp. 231

Stam, D.M., Hovenier, J.W., & Waters, L.B.F.M. 2004, Astron. Astrophys. vol. 428 pp. 663

Thompson, S., Doel, P., Bingham, R. et al. 2003, Ground-based and Airborne Instrumentation for Astronomy II. Edited by McLean. Vol. 4839, pp. 1085

Chapter 3

An exoplanet and circumstellar disk laboratory simulator for testing polarimetric imaging instruments

N. Miesen, L. Einarsen, M. Rodenhuis, S.V. Jeffers, F. Snik and C.U. Keller[1]

Abstract

To test and calibrate the imaging polarimeter ExPo (Extreme Polarimeter), we have built a laboratory-based simulator that mimics a star accompanied by an exoplanet as seen by the 4.2m William Herschel Telescope. The star and planet are simulated using two single-mode fibers held in close proximity, simulating a star-planet separation of 1″. Both fibers are fed by the same broadband arc lamp. The unpolarized star has a flux of 10^{11} photons/s, corresponding to that of a $m_V = 0$ star, and the planet is partially linearly polarized to simulate the scattered starlight, with a flux that can be regulated to create contrasts with the star between 10^{-4} and 10^{-9}. The simulator includes effects of the Earth's atmosphere and the relevant optical properties of the telescope. 1″ atmospheric seeing is simulated using a rotating glass plate covered with hairspray, while atmospheric dispersion is approximated with a wedge prism. In addition to the exoplanet, the setup can also simulate the scattering polarization of a circumstellar disk. We show initial measurements with an ExPo prototype and this simulator that represents the first realistic laboratory simulations of imaging polarimetry for exoplanet detection and characterization.

[1]to be submitted to Astronomy & Astrophysics, 2011

3.1 Introduction

High-contrast imaging of circumstellar environments, in particular to directly image exoplanets, is a field that has seen considerable developments in recent years. Direct imaging of exoplanets is challenging because of the small separation between star and planet and the high intensity contrast between them. As a consequence, only a small fraction of the 500+ extrasolar planets detected so far (Schneider 2010) have been imaged directly (e.g. Lagrange et al. (2009), Marois et al. (2008), Thalmann et al. (2009)).

One way to achieve the required contrast is to use imaging polarimetry: Light scattered by circumstellar material such as planetary surfaces or atmospheres will become linearly polarized (Stam et al. 2004) while light from the star is generally unpolarized. To develop this technique we have built the Extreme Polarimeter (ExPo) for use at the 4.2- meter William Herschel Telescope (WHT). Using our extensive experience in precision polarimetry of the Sun, we aim to reach a sensitivity of 10^{-5} (Keller 2006, chapter 2). In this paper we present the laboratory simulator we have built to test and calibrate the instrument and to minimize any systematic errors. This simulator has greatly aided the development of ExPo.

Several laboratory simulators to test high-contrast imaging instruments have been built before. Ball Aerospace & Technologies (BAT) have developed a testbed for the Terrestrial Planet Finder Coronagraph (TPF-C). This system operates at the low temperatures and vacuum encountered by a space mission (Kendrick et al. 2006) but does not model planet polarization. At Hokkaido University, Baba & Murakami (2003) have built a simulator to test a concept to image extrasolar planets in polarized light, using a two channel stellar polarization-based nulling coronagraph to remove the light of the central star. Other setups such as those built by TU Delft and ETH Zurich use lasers as the light source.

None of these test beds meet our needs and we have opted to build a simulator of our own design. The ExPo simulator produces two point sources at a fixed separation, one of them linearly polarized. The intensity can be regulated to simulate different contrasts. At present, ExPo operates without the aid of Adaptive Optics (AO), and our simulator includes the effect of atmospheric seeing. As ExPo is currently used to study circumstellar disks and other extended sources, a simulation of the polarization structure of such a disk has been added to the simulator. Most components used for the simulator are off-the-shelf, allowing the system to be built for a limited budget.

The next section presents the requirements for the simulator. Sections 3.3 and 3.4 describe the design and test results of the exoplanet simulator. This is repeated for the circumstellar disk part of the simulator in sections 3.5 and 3.6. We conclude the paper with a short discussion of the results and comparison with other testbeds in section 3.7.

3.2 Simulator requirements

3.2.1 Exoplanet simulator requirements

For the exoplanet simulator, we require two point sources separated by 1″ in terms of the λ/D scale of the system. Although it would be desirable to have an adjustable separation between the star and the planet, this immediately leads to a much more complicated design. We want both the star and the planet to emit broadband visible (450 - 850 nm) light, preferably from the same source to avoid differential effects. The star, which shall be bright enough to simulate a $m_V = 0$ star observed through the 4.2 m William Herschel Telescope (WHT), must be unpolarized. The planet must be linearly polarized and we would like to be able to control the orientation of this polarization. It must also be possible to control the brightness of the planet, at least in the 10^{-4} - 10^{-9} contrast range.

Two effects of the atmosphere that seriously influence our observations must be simulated: The seeing effect caused by atmospheric turbulence and the dispersion introduced while observing at non-zero zenith angles. The required simulated seeing is 1″.

The simulator shall also model the relevant optical properties of the WHT. The central obscuration and the spiders in the telescope aperture must be included. The simulator shall produce a beam with the $f/11$ f-ratio of the WHT. We would also like to include the 45° Nasmyth flat reflection. It is however not necessary to simulate the rotation of this flat caused by changing telescope elevation as this would entail rotating the entire simulator in the vertical plane.

As a practical consideration, the simulator needs to fit on our 3×1.5 m optical table.

3.2.2 Circumstellar disk simulator requirements

For the simulation of a circumstellar disk, we require first of all that it must be possible to integrate it with the star-exoplanet simulator without affecting its performance. It is critical that the disk simulator reproduces the azimuthal polarization pattern of a circumstellar disk (figure 3.1). It must be possible to simulate disk diameters of up to 20″ with a surface brightness of 10^{-4} and less of the stellar flux. Preferably, we like to be able to simulate smaller disks as well. We start by simulating a face-on disk, but would like to be able to simulate tilted disks as well.

3.3 Exoplanet simulator design

3.3.1 Design overview

The design of the simulator has been developed around two core ideas that have allowed us to keep the cost relatively low:

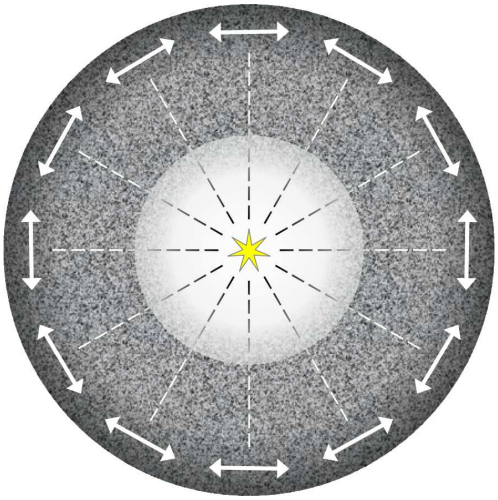

Figure 3.1: Azimuthal polarization pattern of light scattered by a circumstellar disk.

1. We use two bare-cleaved optical fibers, mounted closely together in an image plane, to simulate the star and the exoplanet. Light of different intensities can be injected into these fibers to achieve the desired contrast ratio. The planet light can be polarized before it is injected into the optical fiber, as the fiber does not significantly depolarize the light.

2. We use a glass disk rotating in a pupil plane and covered with several layers of hair spray to simulate the wavefront distortions caused by atmospheric seeing. This idea has been shown to produce realistic results by (Thomas 2004).

To avoid wavelength-dependent differential effects, we use the same light source for the star and the plane. A small fraction of the starlight is reflected to pass through a variable ND-filter and a polarizer before entering into the plane fiber. The starlight passes through a tilted glass plate before entering the fiber. The tilt of this plate can be adjusted about two axes to remove any residual polarization in the starlight.

After being emitted from the fibers, the light passes through a collimating lens. The elements simulating the atmospheric effects are placed in the parallel beam. A second lens simulates the telescope, with an aperture mask placed before it to simulate the obscuration by the spiders and the secondary. The design concept is shown in figure 3.2.

3.3.2 Design implementation

We start with the choice of lenses L1 and L2 through which the beam emerging from the fibers pass. L2 should ideally produce a $f/11$ beam to match that of the WHT telescope. Using two identical lenses for L1 and L2 limits aberrations. We have

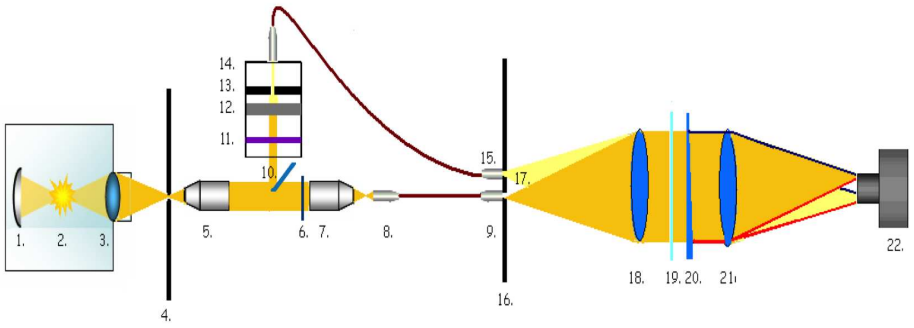

1. Source rear reflector
2. 75W Xenon arc lamp
3. F/2 focussing lens
4. Screen
5. 0.1 NA Microscope objective
6. Waveplate (neutralizing any polarization)
7. 0.1 NA Microscope objective
8. Fiber (Large mode area) input starlight
9. Fiber (LMA) output starlight
10. Tilted window
11. Polarizing filter
12. ND filters
13. Diaphragm
14. Fiber (LMA) input exoplanet
15. Fiber (LMA) output exoplanet
16. Screen
17. Custom bare fiber holder
18. F/12.5, D=80mm achromat lens
19. Atmosphere simulator
20. Wedge prism (1°)
21. F/12.5, D=80mm achromat lens
22. Meade CCD camera

Figure 3.2: Design overview of the fibre-based exoplanet simulator.

chosen two achromats with effective focal lengths of 1000 mm and usable apertures of 80 mm resulting in an f-ratio of $f/12.5$. The diffraction limit for this f-ratio at the lower (450 nm) end of the wavelength range can be computed to be 6.86 μm. For the star and planet to be simulated as point sources, the fiber core diameter must be smaller than this value.

With the diameter of the lenses chosen, the scale of the system in terms of the λ/D ratio with the WHT becomes 52.5. At this scale, the angular separation between star and planet of 1'' translates into a lateral separation of 255 μm. The diameter of the cleaved fibers thus need to be smaller than this, otherwise it will not be possible to mount the fibers next to each other at the correct separation. The Thorlabs 630-HP single-mode fiber meets our requirements as the core diameter is specified as 4±0.5 μm and the diameter of the fiber including cladding and coating as 240±0.5 μm. The fiber has a numerical aperture of 0.13 and a nominal operating wavelength range of 600 – 770 nm.

A key aspect of the design is the custom-fabricated holder we use to hold the fibers at the correct separation. The holder is a precision-machined aluminum block consisting of two symmetrical halves in which a grove has been milled to fit the fiber. With the fibers fitted in the groves, two pieces of 10 μm metal foil are placed between the fibers and the two halves of the holder bolted together. This results in a separation of about 260 μm corresponding to a scaled separation of 1.02''. Figure 3.3 shows the mechanical design of the holder, figure 3.4 the resulting image of the mounted fibers.

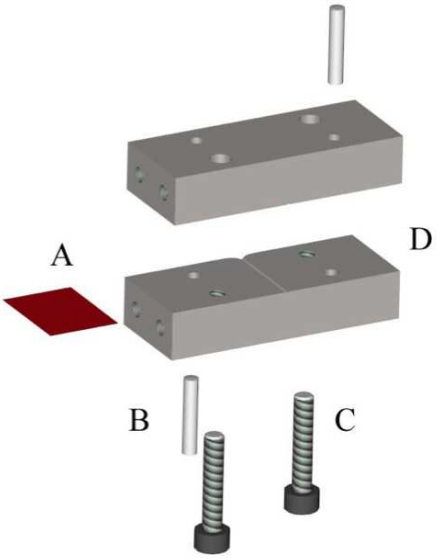

Figure 3.3: CAD-drawing of the components of the fiber holder: A) separating foil B) alignment pins, C) mounting screws ad D) Two halves of the aluminum holder.

A powerful light source is needed to provide sufficient flux to simulate the star. At the 4.2 m WHT, the V-band flux from a $m_V = 0$ star is 10^{11} photons s^{-1}. The light also needs to be focused to a small spot to be coupled into the fiber. We have chosen a Cairn 75 W Optosource Xenon arclamp. The Xenon source provides a reasonably flat spectrum in the 450 850 nm wavelength range we are interested in. The beam from the lamp has a numerical aperture of 0.25 and can focus the light to a spot with a 3 mm diameter. Two microscope objectives are used to couple the light into the star fiber. In between the two objectives, a 45° mirror reflects off a small fraction of the collimated beam towards the planet fiber. This light then passes through a small filter wheel with neutral density (ND) filters of different optical depth. This is used to reduce the planet flux to create the desired contrast with the star. Before entering the planet fiber, the light passes through a polarizer that can be rotated to achieve the right polarization direction. As we need very little light for the planet, no microscope objective is used here. This part of the simulator is placed in a closed box to avoid stray light entering the fibers. The assembly is shown in figure 3.5 below.

The final part of the setup is the simulation of the Earth's atmosphere. Using the formula given by (Drakos 1993) we calculate the differential dispersion between 500 nm and 800 nm by the Earths atmosphere at a Zenith distance of [TBD] degrees to be 0.62″. Multiplied by the system scale factor we get 32.5″. We use an off-the shelf fused silica thin wedge prism with a wedge angle of 1°. The calculated dispersion by this prism is 33.1″. For the atmospheric seeing simulation, we use a rotating

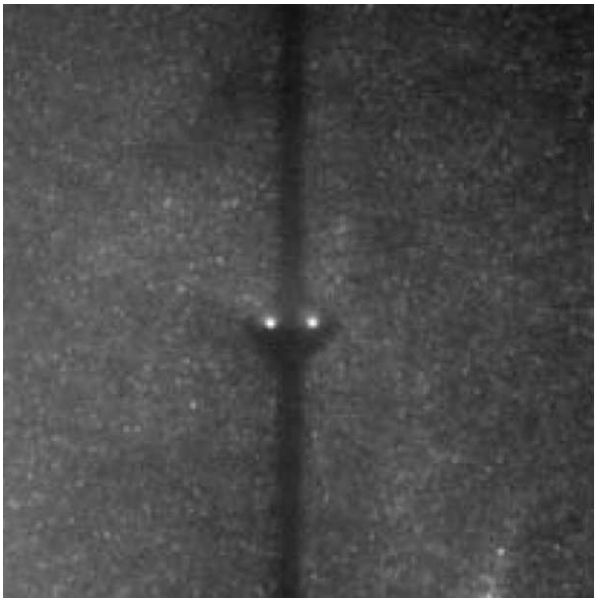

Figure 3.4: The two fibers mounted in the holder with their cores illuminated. The grooves for the fibers can be discerned.

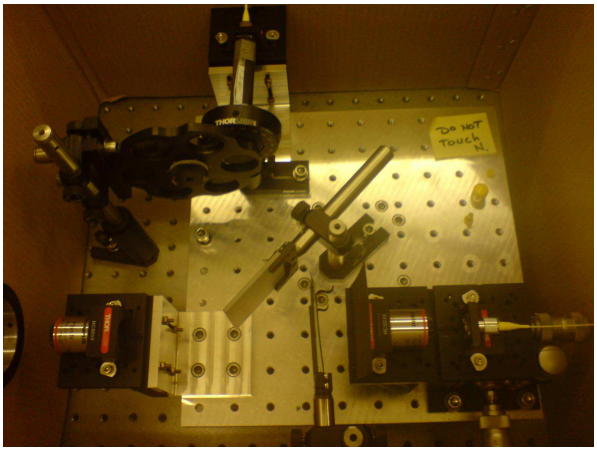

Figure 3.5: Separation of the planet and star beams.

stress-free glass plate sprayed with multiple layers of hairspray. A specific substance found in regular hairspray, Octylacramide/Acrylates/Butylaminoethyl/Methacrylate, causes the scattering of the light that simulates seeing. As will be discussed in the results section, some experimentation with the number of layers and the spraying

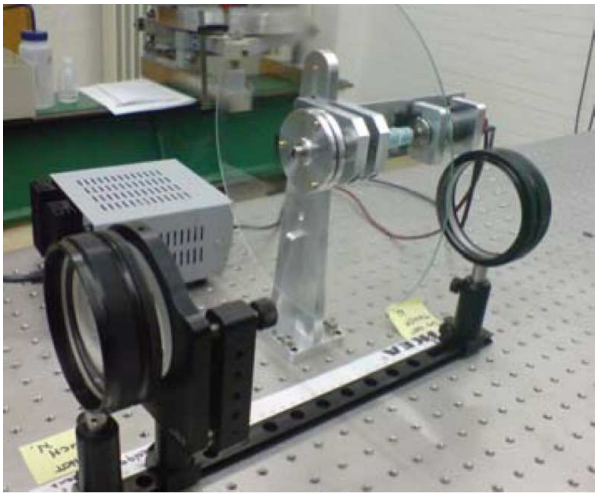

Figure 3.6: The dispersion prism (directly after the lens at lower left) and the rotating glass plate of the atmosphere simulation.

technique was needed before the desired seeing was achieved. Figure 3.6 shows the mounted components of the atmosphere simulation.

3.4 Exoplanet simulator performance

The results presented here have been measured using a Prosilica camera of 640×480 pixels and a pixel size of 7.4 μm. For polarization measurements, we have used a rotating sheet polarizer in front of the camera. A small fiber-fed spectrograph was used to take a spectrum of the simulated star. The gain of the camera was determined experimentally so an accurate measurement of the stellar flux could be made. The flux is well above the required 10^{11} photons s^{-1} needed to simulate a $m_V = 0$ star. The spectrum of the star is shown in figure 3.7, showing that it is decidedly broadband.

Without any ND-filter in front of the planet fiber, the contrast between the star and planet is 1.5×10^{-3}. Using the ND filters, we can of course decrease this contrast. The setup was modified slightly to obtain magnified images of the illuminated fiber cores. The core diameter was measured to be 6.3 μm, sufficiently below the diffraction limit of 6.86 μm. Both star and planet are therefore simulated as point sources. The magnified images were also used to check that no light is leaked between the fibers. If a fraction of the starlight would leak into the planet fiber it would decrease the contrast and make detection of the planet too easy. Light leaking the other way would make the star polarized. With only one fiber illuminated, the intensity at the position of the other fiber was measured. No leaking was detected in either case. The separation between star and planet was measured to be 261 μm, corresponding

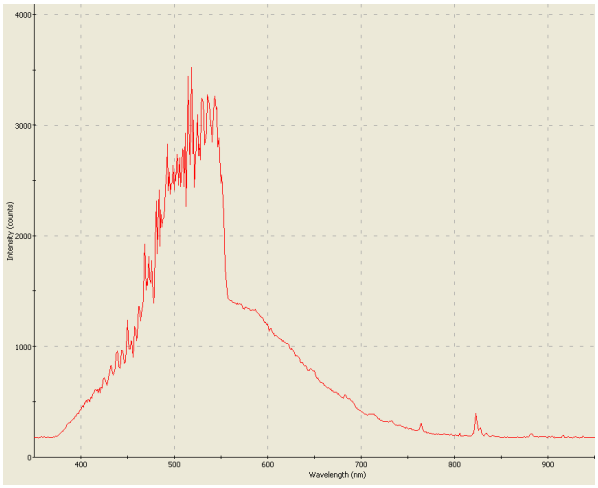

Figure 3.7: Spectrum of the light emitted by the star fiber.

to 1.06″. The polarization of the planet turns out to be sensitive to the layout of the fiber. Loops and bends in the fiber depolarize or convert the linear polarization into circular. Shortening the fiber and minimizing its curves has allowed the degree of polarization of the planet to reach well above 90%. The polarization of the star was initially measured to be several percent. By placing a tilted glass plate in the star beam before it enters the fiber it has eventually been possible to reduce the polarization to 0.6%. After some experimentation, a glass disk with hairspray producing a seeing of around 1″ was produced. The distance at which the can is held when spraying is important as it determines the scale of the structure. 3-4 layers of hairspray were needed. A reliable measure of the seeing produced can only be taken after about a week. The seeing will initially improve as solvents in the hairspray slowly evaporate. On a much longer timescale (several months) the seeing deteriorates again. This may be due to dust sticking to the layers of hairspray. Figure 3.8 shows different levels of seeing.

3.5 Design of the circumstellar disk simulator

The key issue with simulating the circumstellar disk is finding a way to create the azimuthal polarization structure. A device however exists that can achieve this. The so-called Theta cell is a device in which liquid crystals are held between two finely grooved glass plates. In one of the plates these groves are circular, in the other they are linear. The result is that the crystals orient themselves in such a way that incoming linear polarization can be converted to either an azimuthal or a radial pattern, depending of the direction of the polarization. The principle of the device is

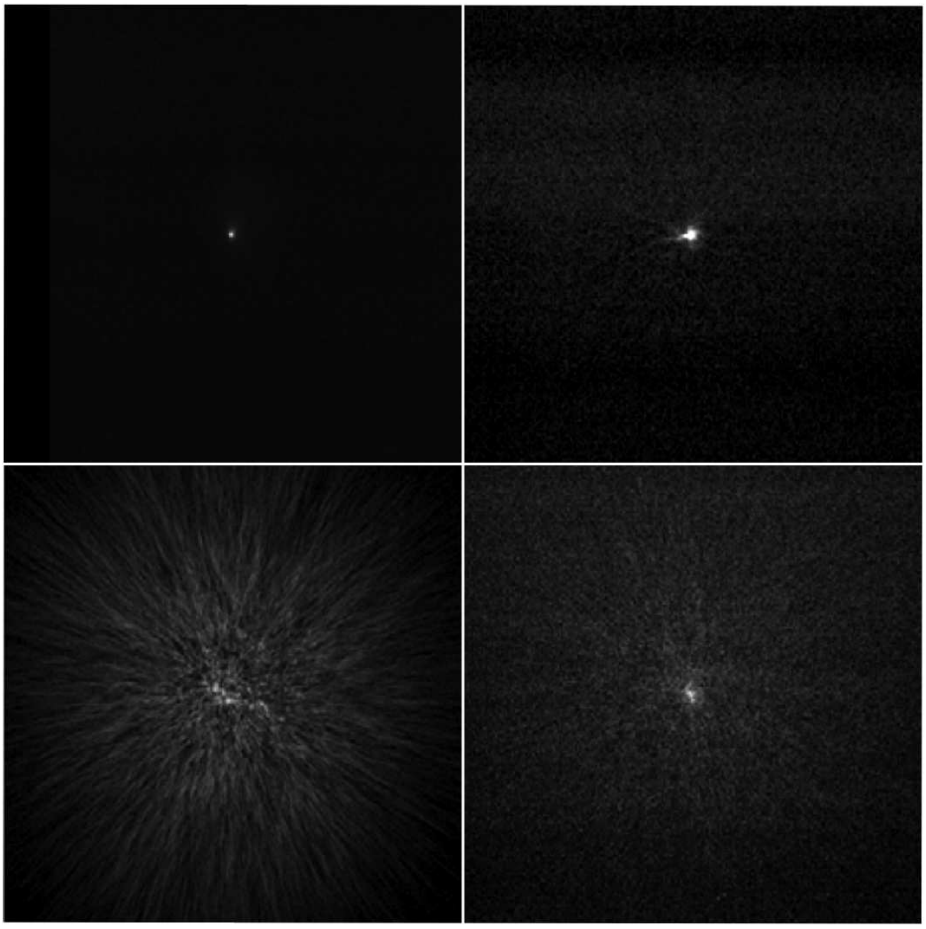

Figure 3.8: Images showing the effect of different layers of hairspray:(clockwise from top left) image with clear glass plate (FWHM = 2 pixels); image with one layer of hairspray (FWHM = 2 pixels); image with two layers of hairspray (FWHM=4.5 pixels); image with three layers of hairspray (FWHM = 29 pixels = 1.06″).

shown in figure 3.9

We project a beam of linearly polarized light through this Theta Cell onto a reflector mounted in front of the fiber holder. The reflector has an opening in the middle to let the light emitted from the fibers pass through. A schematic of this design is shown in figure 3.10.

The beam is projected onto the reflector at an angle of 20° with the optical axis of the existing exoplanet simulator. The Theta Cell is illuminated from an optical fiber through a microscope objective and the linear polarizer. The lens has been chosen to

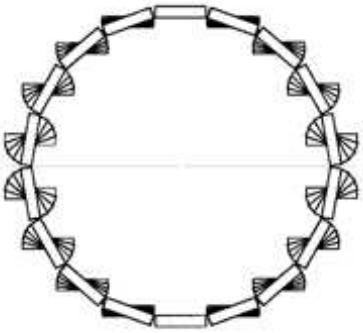

Figure 3.9: Twisted molecular structure of the Theta cell.

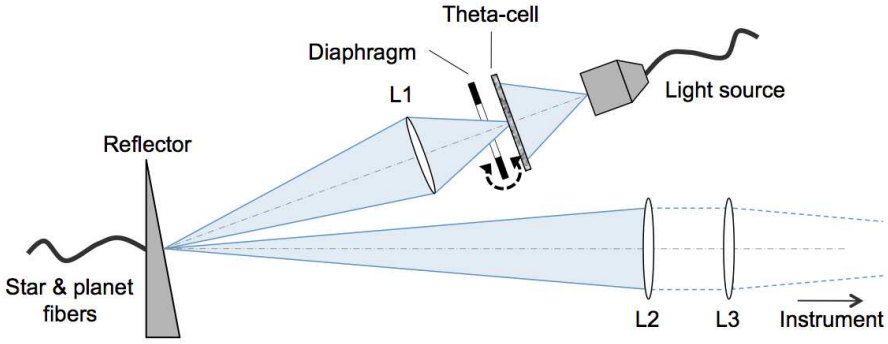

Figure 3.10: Design sketch of the disk simulator.

image the Theta Cell on the reflector with an f-ratio of 12.5, matching that of the beam from the fibers. The image on the reflector has a diameter of 12 mm, corresponding to a disk diameter of 47″. This more than fulfills the 20″minimum disk diameter requirement. A diaphragm is placed close to the Theta Cell. This can be closed to reduce the size of the disk being simulated. The diaphragm can also be rotated perpendicular the optical axis. This creates an elliptical disk image, simulating a disk that is not face-on. Note that disks viewed at an angle will look elliptical but still have a circular, azimuthal polarization structure. A separate light source is currently used to illuminate the circumstellar disk simulation. Even the maximum throughput from

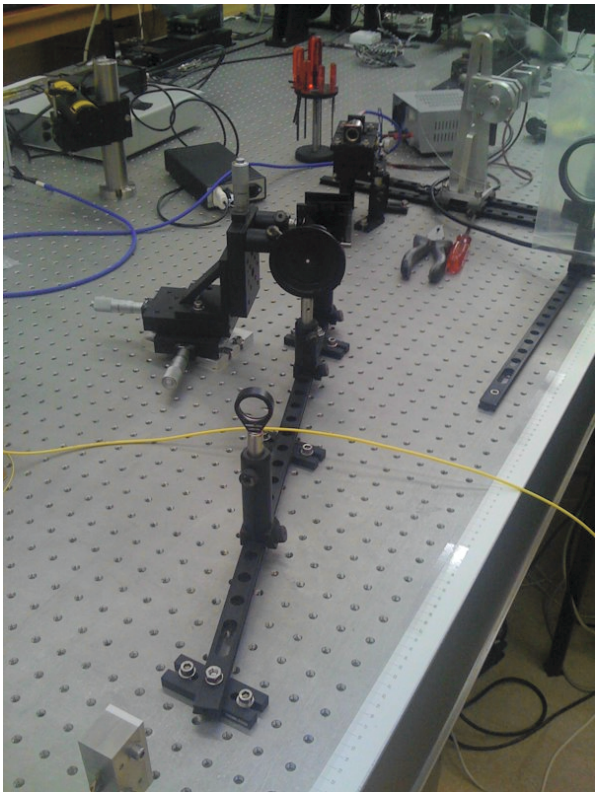

Figure 3.11: Circumstellar disk simulator integrated with the existing exoplanet simulator. Fiber holder with the mounted reflector is at lower left. The disk with the atmospheric seeing simulator can be seen in the background.

the planet fiber was insufficient to create the right contrast for the disk. Figure 3.11 depicts the simulator mounted on the optical table:

3.6 Circumstellar disk simulator performance

Images of the simulated circumstellar disk have been made using our ExPo instrument. Figure 3.12 shows the linear polarization structure of a disk together with a simulated exoplanet. To check the polarization structure more precisely, a profile tracing a circle centered on the star has been recorded from one of the two half-images of the polarimeter. This profile should be sinusoidal. The profile, with a sine fitted, is plotted in figure 3.13. To verify that the center of the polarization pattern is centered on the star, the contrast between the orthogonal polarization directions in the image below has been increased to produce figure 3.14. The cross formed by the boundaries

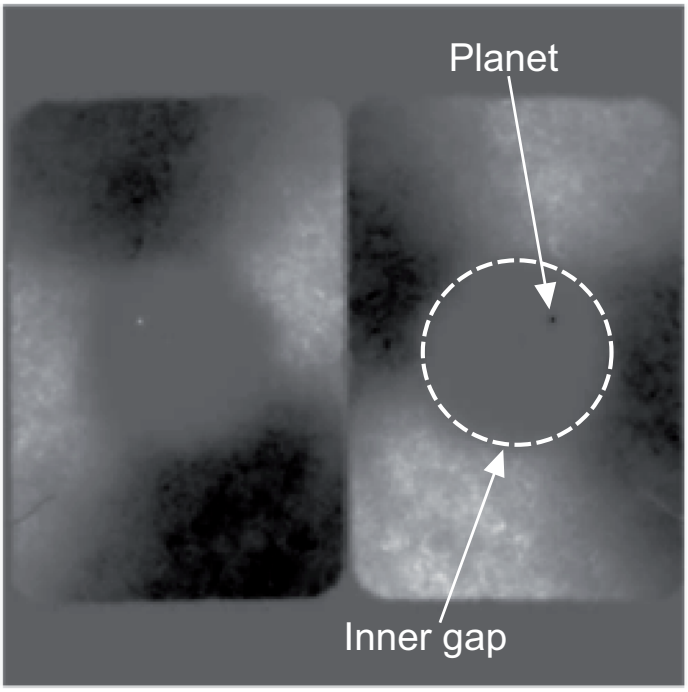

Figure 3.12: Simulated disk and exoplanet. The star was not illuminated and the atmospheric seeing simulation not used for this test. The image shows the linear polarization in both beams of the dual-beam ExPo polarimeter, with one direction shown as positive (white) and the perpendicular polarization direction being negative (black). While not a design requirement, we see that the hole in the reflector nicely simulates an inner gap in the disk. The diameter is about 4″.

between negative and positive polarization is indeed nicely centered on the star.

The second light source produces more than sufficient light to illuminate the disk. In fact an ND filter is needed to reduce its brightness to the required 10^{-4} contrast with the star.

3.7 Discussion and conclusion

One of the challenges in building a realistic scaled simulator of a star with a planet is placing the two light sources sufficiently close together to simulate a typical star/planet system. This should preferably be done without the use of mirrors or other reflective optics as this will induce scattering and unwanted polarization. The innovative design feature of the setup described in this paper, is the relatively simple way of producing the star and planet broadband point sources, with a scaled 1″ separation. The separation was achieved by placing the star and planet optical fibers

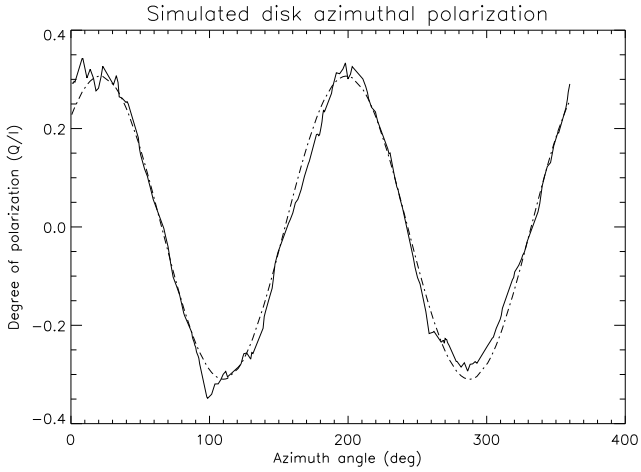

Figure 3.13: Azimuthal profile of the circumstellar disk. The profile is sinusoidal because it is taken from a polarimetry image where one direction is positive (the two maxima) and the perpendicular direction negative (two minima, at 90° from the maxima). When the direction is ignored, the intensity of the polarized light along a circle is more or less constant.

in a custom made holder. The broadband light is required to test the polarimeter for chromatic effects that may reduce its effectiveness. Moreover, the use of a single light source for both the planet and the star avoids differential chromatic effects between the two. Different spectra can however be simulated by inserting filters in both star and planet optical paths

Having a realistic laboratory simulator of a linearly polarized planet orbiting close to its host star is an invaluable resource for testing and calibrating ExPo. The total cost of materials for the simulator is approximately 2/3 of the cost of a night at the WHT. The results of the simulator show that it meets its science requirements, in terms of simulating the star, a linearly polarized planet orbiting at 1″, the effect of seeing, and the telescope. The simulator can also be easily modified to increase or decrease the star/planet contrast ratio and to remove seeing effects. As the data reduction techniques required by extended sources may pose different challenges than for point sources, the circumstellar disk simulator is a highly useful addition.

Comparing with other simulator designs, we find they are more complex or pose problems for the polarimetry, or both. The Ball Aerospace & Technologies (BAT) testbed for the TPF-C (Kendrick et al. 2006) uses a single broadband source (also and arc-lamp) for both the planet and the star. The light is split by an uncoated window beam splitter and coupled into star and planet optical fibers. The light from the star and planet fibers are recombined using a recombiner prism pair. The telescope is then simulated using a spherical mirror. The additional reflections this requires makes this design unsuitable, or at least complicated, to use with polarimetry. While the

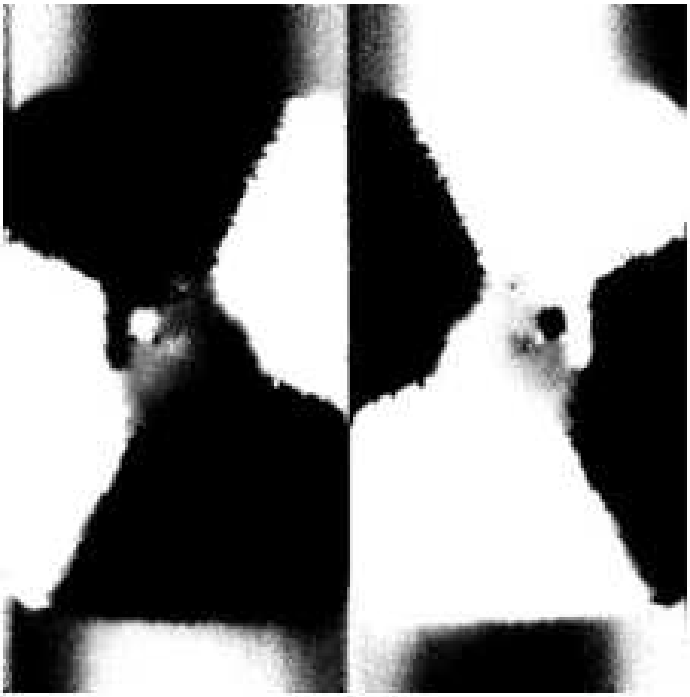

Figure 3.14: Enhanced-contrast image of the polarization structure in the simulated disk.

Hokkaido University setup (Baba & Murakami 2003) is intended for polarimetry, it combines the star and planet beams in a beamsplitting cube (used in reverse), making it harder to control the polarization accurately. In addition, this setup uses different light sources for the star and the planet, risking uncontrolled differential effects. Other setups, such as that developed by TU Delft have no planet, no polarization and do not radiate in broadband light.

3.8 References

Baba, N. & Murakami, N. 2003, The Publications of the Astronomical Society of the Pacific, Volume 115, Issue 814, pp. 1363-1366

Drakos, N. 1993, Computing differential refraction, (www.ls.eso.org/lasilla), (La Silla, Chile) (1993)

Keller, C. U. 2006, Ground-based and Airborne Instrumentation for Astronomy. Edited by McLean, Ian S.; Iye, Masanori. Proceedings of the SPIE, Volume 6269, pp. 62690T (2006)

Kendrick S. E. et al. 2006, Space Telescopes and Instrumentation I: Optical, Infrared,

and Millimeter. Edited by Mather, John C.; MacEwen, Howard A.; de Graauw, Mattheus W. M.. Proceedings of the SPIE, Volume 6265, pp. 62651Q (2006)

Lagrange, A.-M. et al. 2009, Astronomy and Astrophysics, Volume 493, Issue 2, pp.L21-L25 (2009)

Marois, C., Macintosh, B., Barman, T. et al. 2008, Science, vol. 322, pp. 1348

Schneider, J. 2010, The Extrasolar Planets Encyclopaedia (www.http://exoplanet.eu/catalog.php), consulted 30 November 2010

Stalder, M. & Schadt, M., Optics Letters, Vol. 21, Issue 23, pp. 1948-1950 (1996)

Stam, D., Hovenier, J. W. & Waters, L. B. F. M. 2004, Astronomy and Astrophysics, v.428, p.663-672 (2004)

Thalmann, C. et al. 2009, The Astrophysical Journal Letters, Volume 707, Issue 2, pp. L123-L127 (2009)

Thomas, S. 2004, Advancements in Adaptive Optics. Edited by Domenico B. Calia, Brent L. Ellerbroek, and Roberto Ragazzoni. Proceedings of the SPIE, Volume 5490, pp. 766-773 (2004)., ed. D. Bonaccini Calia, B. L. Ellerbroek, & R. Ragazzoni, 766773

Chapter 4

The Extreme Polarimeter: A sensitive imaging polarimeter for high-contrast observations of scattered light from circumstellar environments

M. Rodenhuis, H. Canovas, S.V. Jeffers, and C.U. Keller[1]

Abstract

We present the design, calibration approach, polarimetric performance and sample observation results of the Extreme Polarimeter, an imaging polarimeter for the study of circumstellar environments in scattered light at visible wavelengths. The polarimeter uses the beam-exchange technique, in which the two orthogonal polarization states are imaged simultaneously after which a polarization modulator is used to swap the polarization states of the two beams before the next image is taken. The instrument currently operates without the aid of Adaptive Optics. To reduce the effects of atmospheric seeing, the images are taken at a frame rate of 35 fps, and large numbers of frames are combined to obtain the polarization images. Three successful observing runs have been performed using this instrument at the 4.2 m William Herschel Telescope on La Palma, targeting stars with protoplanetary disks, other young stars and

[1]to be submitted to Astronomy & Astrophysics, 2011

debris disks. In terms of fractional polarization, the instrument sensitivity is better than 10^{-4}. The contrast achieved between the central star and the circumstellar source is of the order 10^{-6}. We show that our calibration approach yields absolute polarization errors below 1%.

4.1 Introduction

More than 500 exoplanets have been detected to date (Schneider 2010). Almost all of these have been detected using indirect techniques such as radial velocity surveys and transit detections. The information that can be gathered about the planets from these detections is however limited. For the majority of the planets, detected through radial velocity measurements, only the orbital eccentricity and distance and a lower limit of the planetary mass can be obtained. Transits yield the planet radius, mass, orbital inclination and in a few cases the upper atmospheric composition (Brown (2001); Charbonneau et al. (2002); Vidal-Madjar et al. (2003, 2004); Deming et al. (2005)). Moreover, these two detection methods have selection effects: radial velocity detections favor high-mass planets in close orbits and transit methods can only detect planets in orbital planes intersecting our line of sight to the star.

To further characterize exoplanets we must be able to directly detect light from them and separate it from the light of the central star. Direct imaging of exoplanets is however a very challenging prospect. Not only is the separation between a star and its companion very small; the ratio of their intensities, the contrast, is extremely high. As a consequence, only a handful of exoplanets have so far been imaged directly (e.g. Lagrange et al. (2009), Marois et al. (2008), Thalmann et al. (2009)). These direct detections have all been performed in the (near) infrared, imaging warm, self-luminous planets around young stars. To observe and characterize cooler planets or even contemplate imaging of rocky planets, we require observations of starlight at visible wavelengths reflected by the planetary atmosphere or surface. Unpolarized light from the central star that is reflected by exoplanets becomes linearly polarized by the reflection process (e.g. Stam et al. (2004)). Imaging polarimetry is therefore an ideal way to discriminate between the polarized light from circumstellar environments and the unpolarized light from the nearby central star. The use of polarimetry to detect and study extra-solar planets has already been investigated by Seager et al. (2000); Saar & Seager (2003); Hough & Lucas (2003).

We have built the Extreme Polarimeter (ExPo) with the aim of developing this technology. This imaging polarimeter has been developed with the goal of achieving an imaging polarimetry contrast better than 10^{-5} unaided by Adaptive Optics. The first concepts for this instrument have been presented by Keller (2006), the initial design is presented in chapter 2. Three successful observing runs have been performed using this instrument so far, all at the Nasmyth visiting focus at the William Herschel Telescope (WHT) on La Palma. The targets observed have included stars with protoplanetary disks, other young stars and debris disks. In this paper we present the instrument design, polarimetric performance and sample results.

We present the measurement principle, beam-exchange polarimetry, in section 4.2. Section 4.3 describes the instrument design and section 4.4 the polarimetric calibration approach. Results from the first observing runs illustrating the instrument performance and scientific potential are presented in section 4.5. Our conclusions are presented in section 4.6.

Table 4.1: ExPo key parameters.

Detector type:	Andor iXon EMCCD
Size (pixels):	512×512
Pixel pitch (μm):	16
Wavelenght range (nm):	500 - 900
Image scale (″/pix):	0.078
Field of view (″per beam):	20×30

4.2 Beam-exchange polarimetry

Polarization measurements are inherently differential: In the case of linear polarization, two measurements taken through orthogonal polarization filters are subtracted. An unpolarized source will be equally present in both measurements and vanish in the difference, while a polarized source will remain. It is necessary to make the two measurements simultaneously, as temporal changes caused by atmospheric seeing will otherwise appear as false polarization signals. A polarizing beamsplitter can be used to do this. However, differential aberrations between the two beams will still appear as false signals. To solve this, a polarization modulator is used to alternately rotate the polarization by 90°, effectively swapping the polarization information that is passed by the two beams. This so-called beam-exchange technique has been developed for sensitive solar polarimetry in the presence of atmospheric seeing (Semel et al. 1993). Keller (1996) has shown this technique to limit errors to 2nd-order effects and to be able to achieve polarization sensitivities better than 1×10^{-5} of the total intensity. The technique is depicted schematically in figure 4.1

To reduce the effects of atmospheric seeing, we take long sequences of many short-exposure frames, combining the frames in sets of 4 and averaging over the sets. The short exposure times (typically 28 msec) ensures that the instantaneous PSF is relatively unchanged between the frames that are subtracted which would otherwise lead to false polarization signals. The alignment of frames within a set is performed based on the PSF, and may change slightly between one set and the next. Using a polarization modulator has a further advantage: The filtering of the polarization state to which the instrument is sensitive takes place at the modulation element, making the instrument insensitive to instrument-induced polarization downstream

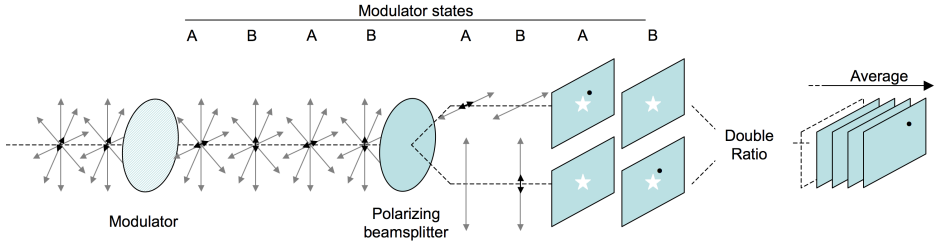

Figure 4.1: Diagram demonstrating the dual beam-exchange technique being used to detect an exoplanet. The modulator alternately aligns the polarization orientation of interest with two orthogonal directions that are then separated by the polarizing beamsplitter. Both beams are imaged simultaneously by a camera. Subtracting the resulting images cancels out the large unpolarized signal while the (partially) polarized planet signal remains.

of the modulator. It is thus desirable to place the modulator as far upstream in the instrument as possible.

4.3 Instrument design

The ExPo design was created to perform five distinct but linked functions, each of which will be discussed in detail below:

Polarimetry: The core of the polarimeter consists of the polarization modulator and the analyzer. For dual-beam polarimetry, the analyzer needs to be a polarization beamsplitter. We have chosen a cube beamsplitter over crystal-based alternatives such as a Wollaston or (modified) Savart plate. The advantage of the cube is that the polarization beamsplitting is achromatic and does not suffer from crystal-induced astigmatism. The price we pay for this is the lower extinction ratio. Moreover, the extinction ratios are not the same for the reflected and the transmitted beams. ExPo currently uses a standard polarizing beamsplitter cube offered by Halle that provides extinction ratios of 1:2000 and 1:40 for the transmitted/reflected beam over the 600-900 nm wavelength range.

The choice of polarization modulator has been driven by the fact that we wish to observe using short exposures in order to minimize the seeing variation during individual exposures and thus need to switch polarization states rapidly between exposures to achieve a high duty cycle. This means a mechanically rotating half-wave plate is not an option. We have chosen to use a Ferro-electric Liquid Crystal (FLC) device, which offers state transition times below 100 μsec. This is significantly faster than twisted nematic cells, for which the transition time is several milliseconds. Another difference is that with FLCs, the orientation of the fast axis is switched, while

in nematics, it is the retardance that is modulated. A problem with FLCs (as with the nematics) is that by definition, the device is a half-wave retarder at a specific wavelength, and so is chromatic. It is possible to combine several waveplates in an achromatic combination (Pancharatnam 1955) and we intend to do this using three FLCs. However, other attempts to do this have not yielded encouraging results and so far we have used a single FLC centered on 750nm.

The orientation of the FLC with respect to the polarizing beamsplitter determines the orthogonal polarization components (e.g. Stokes ±Q) the instrument is most sensitive to, namely the polarization angles that receive the maximum modulation. Polarization components at 45° to these angles (e.g. Stokes ±U) will have minimal modulation, and thus the instrument will be insensitive to them. The FLC is therefore mounted on a rotation stage so the full linear polarization field can be measured.

ExPo has been designed to operate from a gravity-invariant position in the Nasmyth focus of the William Herschel Telescope. At this position, a significant amount of linear polarization is introduced by the 45° M3 reflection. The ExPo design includes a tilted glass plate to compensate this unwanted polarization. A control loop adjusts the tilt continuously after measuring the introduced polarization by comparing subsequent images taken at opposite modulator. The tilt assembly is mounted on a rotation stage that keeps the tilt axis aligned with the M3 orientation as the telescope elevation changes. In order to perform polarimetric calibration, a linear polarizer can be inserted into the beam and rotated to any desired angle.

Coronagraphy: To reach high polarimetric sensitivity with a given dynamic range of the detector, it is desirable to suppress the peak of the stellar PSF. An added benefit is that the stray light in the instrument, and the possibility of it becoming polarized, is reduced. To this end, the ExPo design incorporates a coronagraph. We have opted for a classical Lyot-coronagraph consisting of a mask in the focal plane and a Lyot stop placed in the pupil. A large number of other coronagraph concepts exist but most tend to either introduce chromatic effects or be incompatible with polarimetry. Using a focal mask etched on a glass substrate allows us to use semi-transparent masks. The transmitted stellar peak can be used for precise guiding. The ExPo focal mask can be translated to place coronagraph dots of different sizes in front of the star. The Lyot stop includes masking of diffraction by the telescope spiders, and is mounted on a rotator stage that keeps the mask aligned with changing telescope elevation.

Imaging: To record both beams simultaneously and avoid synchronization issues associated with multiple detectors, ExPo relies on a single detector onto which both beams are projected. Two right-angle prisms mounted onto the polarizing beamsplitter are used to achieve this, as shown in figure 4.2

The detector itself is rotated by 45° to align it with the symmetry axis created by the beamsplitting cube. A disadvantage of this design is the slight projection angle introduced in the images. Due to the symmetry of the design, the projection effect is however the same for both beams, and their images can still be combined. As the instrument operates without the use of an Adaptive Optics (AO) system to correct

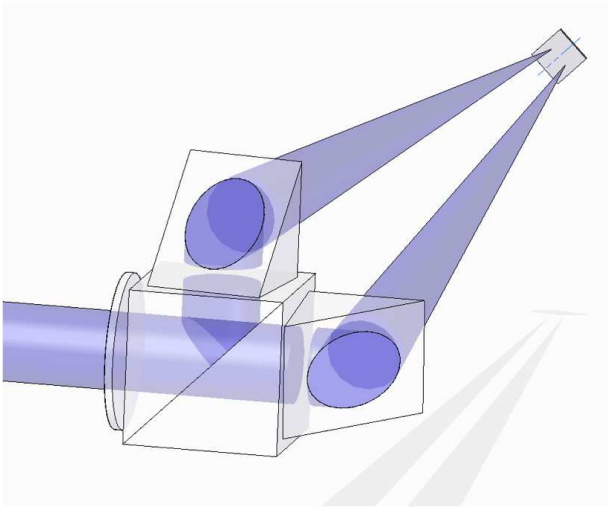

Figure 4.2: After the beamsplitter, the beams are projected onto the detector by slightly rotating the two right-angle prisms.

for the atmospheric seeing, we take large numbers of short exposures, with exposure times of the order of the speckle lifetime. Yet we also wish not to be limited to observing extremely bright targets by the detector readout noise. This has led to the selection of a detector using Electron-Multiplying CCD technology, where a signal can be amplified on the detector before being read out. The detector is an Andor iXon with a resolution of 512×512 pixels and a maximum framerate of 35 Hz. The design of the imaging optics also includes two fairly slow (fD 10-11) lenses, with most optical elements placed in the collimated beam between them. The focal ratio demagnifies slightly to create a field of view of 20×30 arcseconds on each half of the detector. A smaller field of view can be obtained by increasing the focal length of the second lens. This lens is placed directly before the polarizing beamsplitter.

Atmospheric dispersion compensation: The dispersion introduced by the atmosphere needs to be compensated before the coronagraph mask placed in the prime focus. A longitudinal ADC design has been chosen, primarily because any polarization introduced will be stationary in the telescope frame of reference. As with the polarization introduced by the Nasmyth flat, this can be compensated by the polarization compensator. The design consists of two wedge prisms, one fixed and one that can translate along the optical axis to increase the distance between the prisms, increasing the dispersion angle compensated. The complete ADC is mounted to the telescope derotator flange that can rotate to keep the prisms aligned with the plane of dispersion as the telescope elevation changes. For this design it was possible to use two identical off-the-shelf 3-inch prisms with a wedge angle of $3°$.

Wavelenght selection: A filter wheel with 12 50 mm circular filter positions is

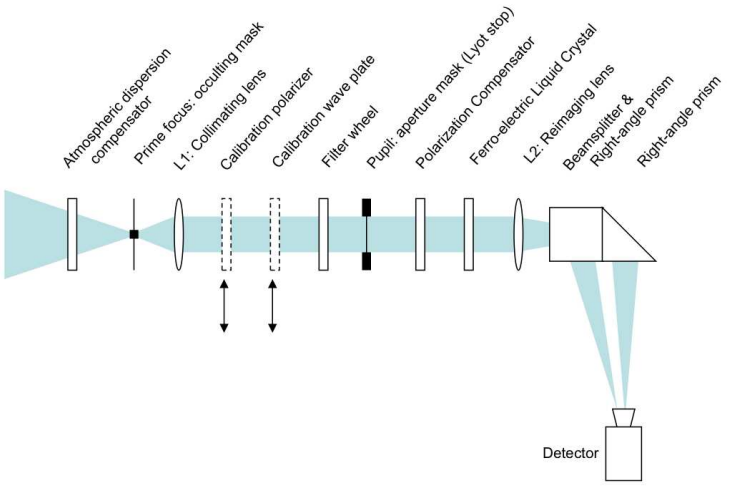

Figure 4.3: Schematic diagram showing the different ExPo components. The occulting mask in the prime focus and the aperture mask in the pupil image together form the coronagraph that suppresses the light from the star. The core of the polarimeter consists of the Ferroelectric Liquid Crystal (FLC) acting as the modulating element and the polarizing beamsplitter that splits the beam into its orthogonal polarization components.

used to perform ExPo observations with an array of broad- and narrowband filters.

Figure 4.3 below presents the instrument block diagram below showing the integration of these five design elements. The ExPo photon budget is provided in table 4.2.

In principle it is desirable to place the polarization modulator as far upstream in the instrument as possible. Any instrumental polarization introduced downstream will not be modulated and so cancels out in the differential imaging. The modulator however needs to be placed after the polarization compensator. As the compensators tilted glass plate introduces a slight and variable beam shift, it must be placed after the pupil mask, which requires precise alignment. This is the reason the modulator ends up relatively far downstream in the design.

Mechanically, the design is intended to be flexible, with components mounted and aligned individually on the optical table at the Nasmyth visiting instrument focus of the William Herschel Telescope. Much of the mounting hardware is off-the-shelf, with custom mounting hardware produced by our in-house workshop. After each observing run, the instrument is shipped back to our institute for testing and improvements in our optical lab. Figure 4.4 shows the instrument as mounted at the telescope.

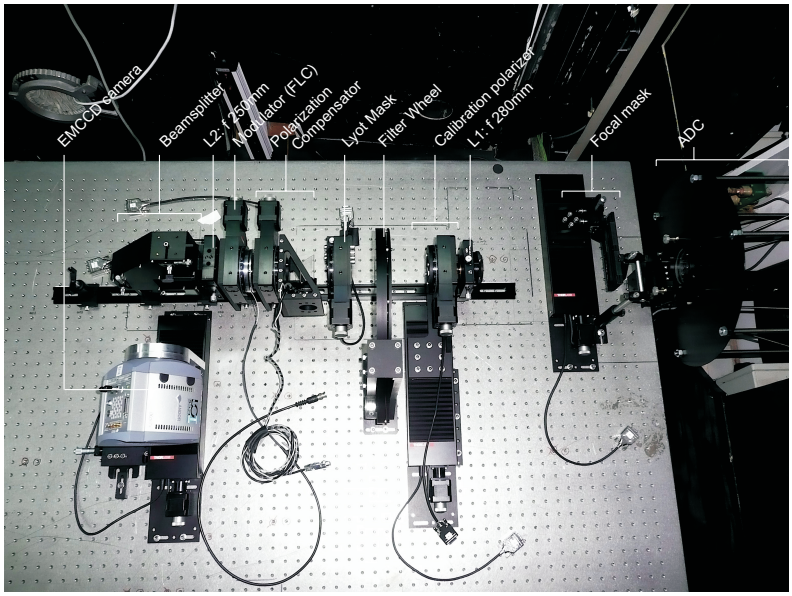

Figure 4.4: Image showing the instrument as installed on the WHT Nasmyth port optical table during one of the observing runs.

4.4 Data reduction and polarimetric calibration

The raw product of ExPo measurements are image series in which the even and uneven frames correspond to the two different states of the FLC polarization modulator. Each raw image has a left and right sub-image formed by the two beams of the polarizing beamsplitter (figure 4.5).

The FLC itself can be rotated to change the polarization direction to which the instrument is sensitive. The angle at which the instrument is sensitive to $\pm Q$ (in Stokes notation) is offset 22.5° from the angle for $\pm U$. For redundancy, ExPo observations are performed at four different FLC angles: 0°, 22.5°, 45°, 67.5°. With the combination of two FLC states (A, B) and the left/right sub-images, the beam-exchange technique thus yields four different types of images at every FLC angle.

For a general polarimeter, a minimum of four independent signals must be measured in order to determine the four elements of the Stokes vector. The signal matrix X relates the measured signals $\mathbf{S}$ to the input stokes vector I:

$$\mathbf{S} = \mathsf{X} \cdot \mathbf{I} \tag{4.1}$$

If X can be determined from a calibration source, its inverse can be used to obtain

Table 4.2: ExPo Photon budget (at 650 nm)

Element	Transmission
Atmosphere (V-band)	0.90
Central obscuration	0.94
Telescope primary	0.90
Telescope secondary	0.90
Nasmyth flat	0.90
ADC	0.98
Focal mask (no dot)	0.95
Collimating lens	0.98
Filter (Schott OG590 glass)	0.90
Lyot stop	0.75
Polarization compensator	0.93
Polarization modulator (FLC)	0.85
Refocussing lens	0.98
Beamsplitter (reflected)	0.48
Beamsplitter (transmitted)	0.42
Right-angle prisms	0.98
CCD Quantum Efficiency	0.93
Total (reflected beam)	0.13
Total (transmitted beam)	0.11
Photons, $m_V = 0$ star	
Entering 4.2 m telescope:	1.12×10^{11} ph/s
Detected (reflected beam):	1.4×10^{10} ph/s
Detected (transmitted beam):	1.3×10^{10} ph/s

the Stokes elements for the observed targets:

$$\mathbf{I} = \mathsf{Y} \cdot \mathbf{S} \quad \text{with} \quad \mathsf{Y} = \mathsf{X}^{-1} \tag{4.2}$$

ExPo does not measure circular polarization, so we are only interested in the first three elements of the Stokes vector: I, Q and U. For this, four measurements are more than sufficient. The two beams, two FLC states and four FLC angles combined provide 16 different measurements from which four must be chosen. However, choosing the A/B and left/right combination of images for a single FLC angle does not work. As the FLC exchanges the beams between the two modulation states, the A-left images will to a large degree contain the same polarization information as the B-right images. The same goes for the B-left and A-right pair, resulting in an ill-conditioned signal matrix X. Another option is to combine all four FLC angles for a single choice of FLC state and beam, e.g. A-left. These four measurements are sufficiently independent and matrix X will be well-conditioned and invertable.

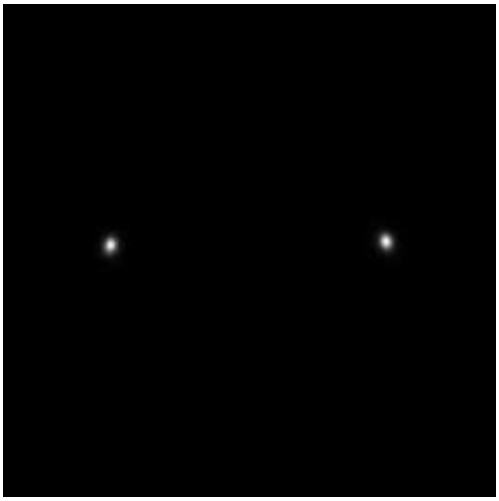

Figure 4.5: Raw ExPo frame showing the double image created by the two beams.

But this approach results in another problem: As the observation at a single FLC angle may take up to an hour, observational conditions will have changed too much between the first and the last FLC angle for them to be combined in a meaningful way. Furthermore, as the telescope tracks the target across the sky, unpolarized artifacts such as ghosts may change position in the image and will then no longer vanish from the result. To overcome these issues, we start by combining the images for a single FLC angle in the so-called double-difference:

$$S_{DD} = \frac{1}{2}(S_{A,left} - S_{A,right} - S_{B,left} + S_{B,right}) \tag{4.3}$$

As the left and right sub-images are located on the same raw image, it is essential that they are carefully co-aligned before the above subtraction takes place. Canovas et al. (2011) discuss in detail the processing of raw images performed to generate the double-difference images. Unpolarized signals drop out in this measurement, for which Keller (1996) has shown that all first-order effects drop out. A reduced signal matrix now relates the two double-difference measurements for FLC angles 22.5° degrees apart to the linear polarization elements of the Stokes vector:

$$\begin{pmatrix} S_{DD}^{FLC1} \\ S_{DD}^{FLC2} \end{pmatrix} = \mathsf{X} \cdot \begin{pmatrix} Q \\ U \end{pmatrix} \tag{4.4}$$

The parameters of X are determined by taking dome flats with the calibration polarizer at different angles. A fitting routine is used to fit the response parameters

a, b for each double-difference signal:

$$S_{DD} = \begin{pmatrix} a & b \end{pmatrix} \cdot \begin{pmatrix} Q \\ U \end{pmatrix} \tag{4.5}$$

The initial fit assumes the light entering the calibration polarizer is unpolarized. In reality this is not the case: The dome lights may be polarized and the Nasmyth flat will certainly introduce polarization. We iterate the fitting by using the first fit to calibrate dome flats taken without the calibration polarizer and estimate the real input Stokes vector. A new fit is then performed using this estimate. Errors are estimated by back-calibrating the flats taken with the calibration polarizer. Two iterations are sufficient to reduce the errors to a few percent. For real observations, the instrumental polarization introduced upstream of the calibration polarizer is removed by the polarization compensator. Table 4.3 shows the increase in accuracy of the consecutive calibration iterations and the effect of the polarization compensator.

Table 4.3: Dome flat polarization after each calibration iteration and the effect of the Polarization Compensator (PoCo).

Calib.	PoCo Off		PoCo On	
iteration	Q (%)	U (%)	Q (%)	U (%)
1	0.0	0.0	0.0	0.0
2	-0.02765	3.22021	0.00437	0.00243
3	-0.02740	3.21953	0.00437	0.00243
4	-0.02740	3.21953	0.00437	0.00243

The current ExPo setup is quite chromatic, using only a single FLC and not an achromatic, Pancharatnam configuration. As we use dome-flats with a specific spectrum for our broad-band calibration, the calibration may not be correct for targets that have a substantially different spectrum. This is certainly the case for young stars peaking towards the blue, such as AB Aurigae, as the dome flat lamps are fairly red (T_{eff} = 3000K). To overcome this problem, we have created a model of ExPo including the spectral response of all wavelenght-sensitive components, in particular the FLC, the polarization beamsplitter and the QE-curve of the detector. Using this model, we are able to generate synthetic calibration flats for any desired spectrum. The model has been calibrated to so that integrated dome flats generated with the dome flat spectrum are within 1% of the real flats.

As unpolarized signals drop out in the double difference, Stokes I cannot be determined from the double difference, but is instead found from:

$$I = \frac{1}{2}(S_{A,left} + S_{A,right} + S_{B,left} + S_{B,right}) \tag{4.6}$$

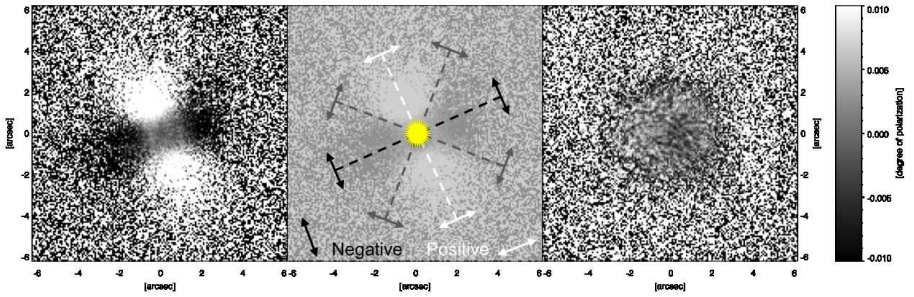

Figure 4.6: Uncalibrated fractional polarization images of the AB Aurigae protoplanetary disk illustrating the butterfly signature produced by the tangential polarization pattern. For comparison, the image on the right shows the diskless star HD112815. The images are clipped at ±1% degree of polarization.

Note that this yields the calibrated intensity in polarimetry terms but does not take attenuation by the atmosphere and optical transmission losses into account. A photometric intensity calibration must be performed using standard stars. The final step in the data reduction is the correction for sky rotation during the long observation sequences. This is achieved by first obtaining the double difference measurements from subsets corresponding to 30 seconds of observations. Each block of frames is physically rotated and calibrated while correcting for the rotation of polarization frame of reference. These blocks are then added together to obtain the final images in Stokes I, Q and U.

4.5 Instrument performance

Three successful observation campaigns have been conducted using the ExPo instrument at the William Herschel Telescope on La Palma. A short fourth run was conducted with a smaller field of view of 10″×15″, but this did not produce good results, partly due to adverse meteorological conditions. The observations have initially focused on stars known to or suspected of harboring protoplanetary disks as well as some debris disks. Here we present some results illustrating the performance of the instrument. Actual science results and analysis will be the topic of forthcoming papers.

For face-on disks, the direction of the scattering polarization from a disk is perpendicular to the direction to the star. In the uncalibrated double-difference images, this polarization signature produces a double-lobed butterfly pattern, illustrated in figure 4.6.

To demonstrate the advantage of the beam-exchange method, we have generated uncalibrated polarization images using only a subset of the data, emulating the

performance of a single beam instrument and an instrument that does not include modulation. The results are shown in figure 4.7.

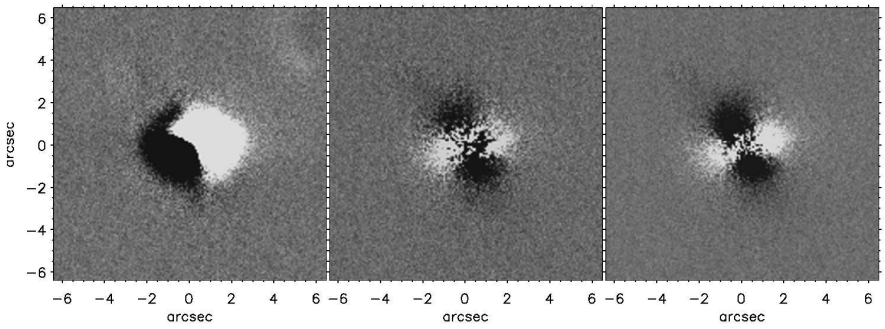

Figure 4.7: The advantage of the beam-exchange method. Left image: dual-beam without modulation. Middle: Single beam with modulation. Right: dual beam and modulation. Target is AB Aurigae.

In the left image, where the left and right beams are combined without modulation, differential aberrations between the two beams clearly destroy the butterfly pattern. In the middle image, in which subsequent modulated images from a single beam are used, the change in atmospheric seeing between the subsequent images produce smearing and a less defined butterfly pattern. The sharpest polarization pattern is clearly produced by the leftmost image, produced using the beam-exchange method.

The ExPo polarimeter is not intended primarily to provide extremely accurate absolute polarization measurements, but to be very sensitive to spatial variations in the polarization. Still, the calibration procedure described in the previous section yields results accurate down to the 1% range. Table 4.4 presents typical accuracies when back-calibrating the dome flats taken at different calibration polarizer angles:

Observations of diskless and unpolarized standard stars must be performed in order to check that the instrumental polarization introduced by the Nasmyth flat is correctly compensated. Table 4.5 shows the calibrated Stokes vectors of two diskless stars, demonstrating that this is the case.

A more visual confirmation can be obtained by simply mapping the polarization of the central part of a diskless star. The result can be found in figure 4.8.

A final analysis that can be performed using the diskless stars is to check how well the instrument rejects unpolarized light as a function of the radial distance to the star. Figures 4.9 & 4.10 show a radial profile of the achieved contrast and fractional polarization based on azimuthal averages. Figure 4.9 shows the total contrast: the polarized flux divided by the peak total stellar flux. The contrast achieved is 10^{-4} at the star position, increasing to 10^{-6} at about 4″ from the star. It should be noted

Table 4.4: Typical dome flat back-calibration residual calibration errors.

Calibrator position	Using FLC 0 & 22.5 Error in Q	Error in U
$+Q$	0.17%	1.03%
$+U$	0.22%	0.20%
$-Q$	0.16%	1.00%
$-U$	0.22%	0.20%
	Using FLC 45 & 67.5	
$+Q$	0.24%	0.63%
$+U$	0.39%	0.34%
$-Q$	0.22%	0.59%
$-U$	0.39%	0.34%

Table 4.5: Calibrated linear Stokes vector elements for two diskless stars. The values are averages of a 5×5 pixel area centered on the star.

Calibration star	Using FLC 0 & 22.5 Measured Q	Measured U
HD86275	-0.015%	0.002%
HD107170	-0.024%	-0.023%
	Using FLC 45 & 67.5	
HD86275	0.047%	-0.002%
HD107170	0.014%	0.017%

that fewer frames were taken in the observation of this diskless star in comparison with regular science targets. The higher photon noise limits the contrast achieved. This is clarified by the figure 4.10 showing the fractional polarization (polarized flux divided by total flux at the present radial distance from the star) plotted together with the profile of the photon noise detection limit. The measured fractional polarization closely traces this theoretical detection limit, except very close to the star, where the statistics become degenerate because of the small number of pixels that can be azimuthally averaged, and far away from the star, where there is hardly any signal detected and the result becomes very sensitive to small flat-field or dark correction errors. The fractional polarization that can be detected is therefore limited by the photon noise. Higher contrasts can be achieved using longer exposure times.

Having shown that our sensitivity is limited by the photon noise, it is clear that high-contrast polarimetry is a photon-hungry application. So while the polarization

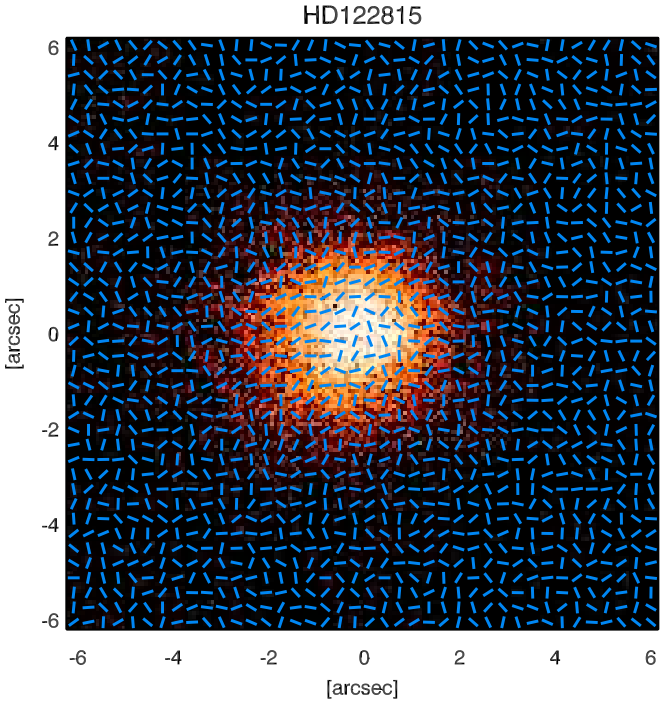

Figure 4.8: Polarized intensity image of the unpolarized reference star HD122815 overlaid with calibrated polarization vectors. The reason we still see a signal is that the polarized intensity, defined as $\sqrt{Q^2 + U^2}$, includes the absolute value of the photon noise. The vectors show no preferred orientation or other structure, showing that there is no residual instrumental polarization after the calibration.

sensitivity and accuracy are key performance parameters for a polarimeter, another important characteristic is the efficiency with which these results are achieved, i.e. how well the instrument makes use of the available photons. Del Toro Iniesta & Collados (2000) define the polarimetric efficiency with which a polarimeter measures the Stokes elements as:

$$\varepsilon_i = \frac{1}{\sqrt{m \sum_{j=1}^{m} \mathsf{Y}_{ij}^2}} \tag{4.7}$$

With Y being the inverse of the signal matrix X as described in the previous

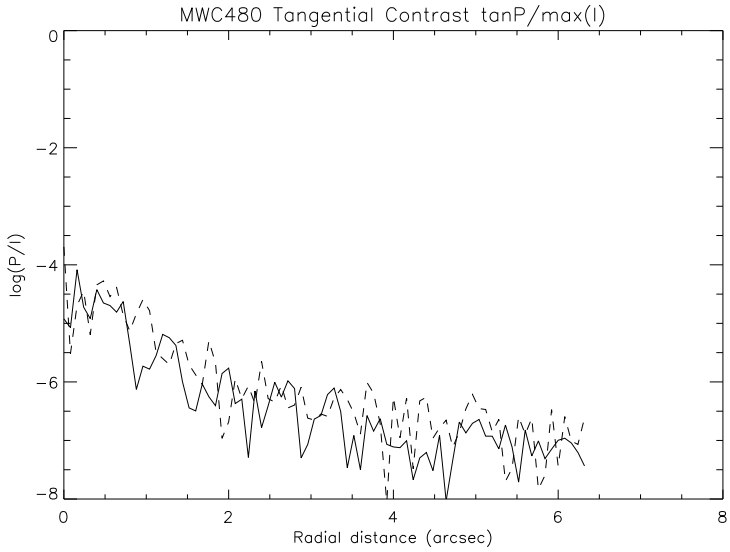

Figure 4.9: Contrast reached for increasing distance from the star. At the peak of the star, the contrast reached purely by polarimetry is 10^{-4}. This increases further out as the stellar intensity decreases. This target was observed for about 10 minutes, higher contrasts can be reached with longer observations.

chapter, m the number of measurements and i the index of the Stokes element. This expression makes no assumptions on how many measurements are performed to determine the Stokes element and how these measurements are performed. It is thus a global measure of the polarimeter efficiency with a theoretical maximum of 1.

Table 4.6 presents the efficiencies calculated for the individual beam and FLC state combinations (not the double difference), using all four FLC angles for the calibration matrices. The efficiencies per Stokes element are defined so that:

$$\varepsilon_Q^2 + \varepsilon_U^2 + \varepsilon_V^2 \leq 1 \tag{4.8}$$

As we do not measure circular polarization, the efficiency in V can be ignored. If we then require equal efficiency in Stokes Q and U we see that the maximum theoretical efficiency that can be reached is $\sqrt{0.5} = 0.707$.

4.6 Sample result: AB Aurigae

As a sample science result, we present our imaging polarimetry observations of the well-known circumstellar disk around AB Aurigae. Imaging polarimetry is an excellent tool to observe the faint, linearly polarized light scattered by the circum-

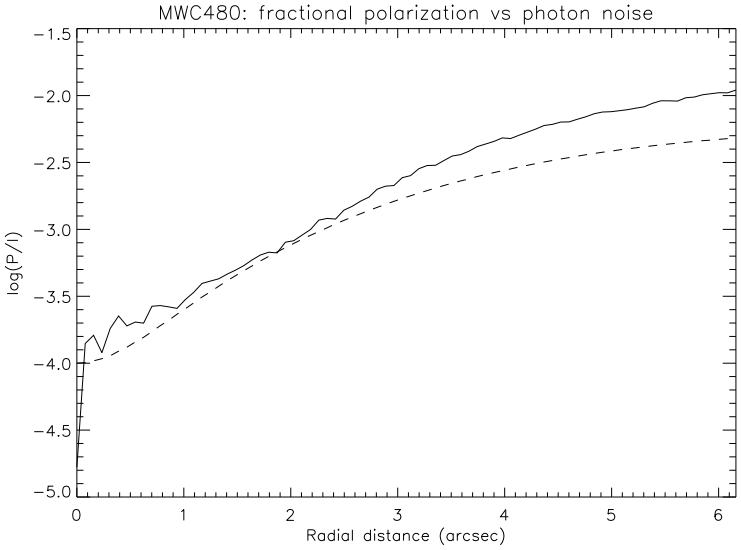

Figure 4.10: Fractional polarization averaged i circles around the star for increasing radial distance (solid line). The sensitivity is limited by photon noise and thus reaches its maximum close to the peak of the stellar flux. Dashed line: photon noise limit per pixel, averaged in circles around the star.

Table 4.6: ExPo polarimetric efficiency per stokes element for individual FLC state & beam combinations.

FLC state	Beam	ε_i	
		Q	U
A	Left	0.56	0.56
	Right	0.57	0.58
B	Left	0.56	0.56
	Right	0.56	0.57

stellar disk material while suppressing the unpolarized starlight. Kuhn et al. (2001) and Apai et al. (2004) have presented early studies of circumstellar disks using this technique.

The protoplanetary disk around AB Aurigae, a 4±1 Myr old Herbig star, has been shown (Grady et al. 1999, Fukagawa et al. 2004) to have several spiral arms. Imaging polarimetry observations by Oppenheimer et al. (2008) revealed an annulus with a gap at about 100 AU from the star. This gap was speculated to be caused by a companion, but Perrin et al. (2009) showed that the structure can also be explained by the geometrical projection effect of the inclined disk. Only recently Hashimoto

et al. (2011) presented very high resolution imaging polarimetry of the AB Aurigae disk. Their results reveal detailed structure in the inner region (up to 150 AU) of the disk, as well as clearly revealing the spiral arms extending out to about 450 AU. These results were all achieved using AO-assisted (or space-based in the case of Perrin et al.) coronagraphy in the near-infrared.

Our observations date from January 2^{nd} 2010. The imaging has been performed without the use of a color filter, thus spanning the full 400-900 nm wavelength range of our detector. Other observations have been performed using a Schott OG590 filter, but the results are inferior. This is not surprising given the A0e spectral type of AB Aurigae and the higher scattering efficiency towards the blue end of the spectrum. The average seeing during the observations was 1.0''.

Figure 4.11 shows two calibrated polarized intensity images, each generated by combining two sets of observations with the position of the FLC modulator 22.5° apart. The structure in both images is very similar, even thought the seeing was slightly worse for the observations used in the right image. The disk is slightly elongated along the NE-SW axis, which is consistent with previous observations. In the inner region, up to about 1'' from the star, we detect and elongated, almost bipolar structure oriented in the perpendicular direction. This structure is about at the highest resolution that can be resolved in our seeing-limited observations, but corresponds well to regions with higher polarized intensity to the NW and SE in the observations by Hashimoto et al.. Intriguingly, the first black contour in the left image appears to trace a similar annulus with a gap as reported by Oppenheimer et al., although the position is rotated slightly. Again, this is at the resolution limit and does not appear in the right-hand image, but both show traces of an annulus with a cleared inner region to the north of the star.

What can be seen very clearly in both images is a spiral arm starting at about 150 AU (1'') east of AB Aurigae and curving outward in the clockwise direction. To bring this structure out more clearly we have azimuthally averaged the image and then subtracted this from the original, producing figure 4.12. The arm labeled 'S1' by Hashimoto et al. shows up very clearly, while there are hints of two other arms.

Figure 4.13 shows the disk polarized intensity overlaid with a vector plot mapping the polarization orientation. This is a useful test to ascertain that it is indeed the scattering polarization that is observed and that there are no offsets caused by errors in the calibration or the removal of instrumental and sky polarization. As expected, the polarization direction is perpendicular to the scattering plane, producing the azimuthal vector plot.

4.7 Discussion & conclusion

The results we have presented demonstrate that our choice for the fast-modulating beam-exchange method and our relatively simple polarization-friendly optical design results in a sensitive imaging polarimeter, able to produce high-contrast observations of circumstellar environments without the aid of an AO system or a corona-

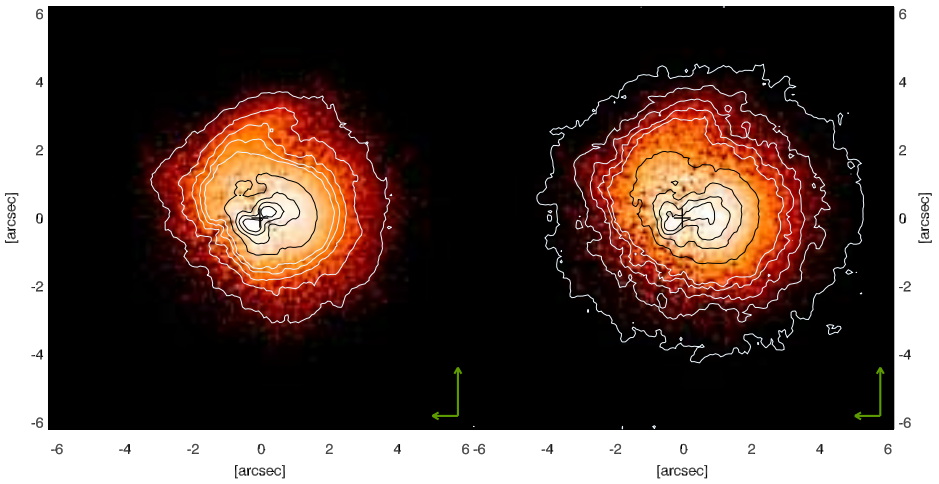

Figure 4.11: Broadband-visible polarized intensity images of AB Aurigae. Observations at two positions of the liquid crystal polarization modulator have been combined to create each calibrated image: 0° and 22.5° for the left image, 45° and 67.5° for the right image. The color scale is logarithmic and histogram-equalized. Black contours go from 80% of the maximum polarized intensity downwards in steps of 20%, white contours go from 10% of the maximum down in steps of 2%.

graph. While the sensitivity of around 10^{-4} is not as high as some aperture-integrated polarimeters such as PlanetPol (Hough et al. 2006) and POLISH (Wiktorowicz & Matthews 2008), the spatial information is highly useful, not only because of its inherent potential to detect and study structures in circumstellar envelopes but also as a means to check the observations for global errors introduced by instrumental or sky polarization. The calibrated polarization accuracy of 1% that can be reached with ExPo is similar to these instruments.

Being seeing-limited, the spatial resolution achieved with ExPo is not anywhere near that which can be achieved by current (e.g. HiCIAO: Hodapp et al. 2008) and future (e.g. GPI: Perrin et al., 2010; Sphere-ZIMPOL: Thalmann et al., 2008) AO-assisted coronagraphic imagers on 8-m telescopes. But none of these instruments have been designed specifically with polarimetry in mind and are likely to suffer sensitivity and accuracy losses incurred by the many reflections before the light arrives at the polarimeter module. Moreover, with the exception of Sphere-ZIMPOL, these instruments operate in the near-infrared, forgoing the inherently higher resolution and higher scattering efficiency available at shorter wavelengths.

With our sensitivity limited by photon noise, ExPo would of course benefit from operating at a bigger telescope or adding up more frames for a longer accumulated

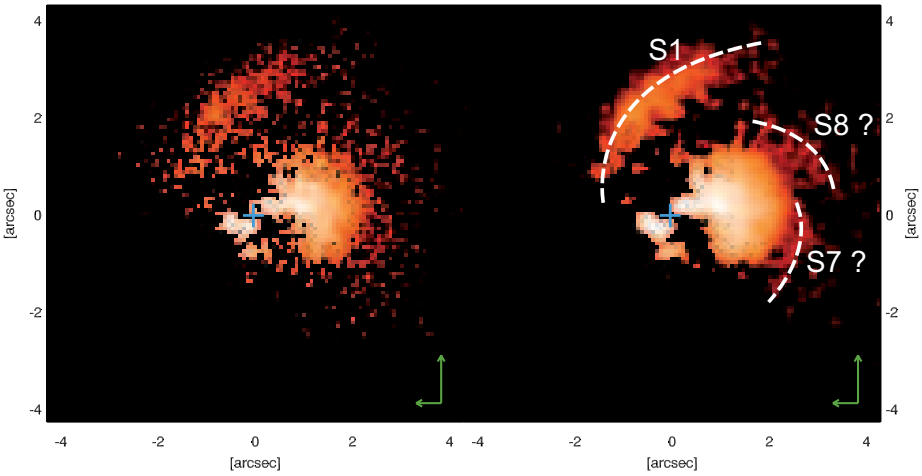

Figure 4.12: At left, the azimuthal average has been subtracted from the AB Aurigae polarized intensity image. At right, the image has been smoothed with a box-car width of 2 pixels. At least one of the spiral arms can clearly be identified. The arms have been labeled with the corresponding numbers from Hashimoto et al. (2011). The color scale is logarithmic.

exposure time. The last option is however complicated by seeing variations that occur over the longer timescale. Apart from the obvious attraction of higher resolution, this is another motivation for developing a polarization-optimized AO system for ExPo. An AO system will also allow us to make better use of the coronagraph included in ExPo.

The suppression of starlight achieved by combining coronagraphy and imaging polarimetry, coupled to the resolution and photon-flux provided by ELT-class telescopes and their associated extreme-AO systems, will enable contrasts of 10^{-8} - 10^{-9} to be achieved, the threshold at which Earth-like planets will be come detectable. We are currently applying the experience gained with ExPo to the design of the EPOL imaging polarimeter arm of the EPICS planet imaging & characterization instrument for the European ELT.

4.8 References

Apai, D., Pascucci, I., Wang, H. et al. 2004, Star Formation at High Angular Resolution. Burton, M. G., Jayawardhana, R. & Bourke, T. L. Eds. IAU Symposium vol. 221pp. 307

Brown, T. M. 2001, Astrophys. J. vol. 553, pp. 1006

Canovas, H., Rodenhuis, M., Jeffers, S. V. et al. 2011, in preparation

Charbonneau, D., Brown, T. M., Noyes, R. W., & Gilliland, R. L. 2002, Astrophys. J. vol. 568, pp. 377

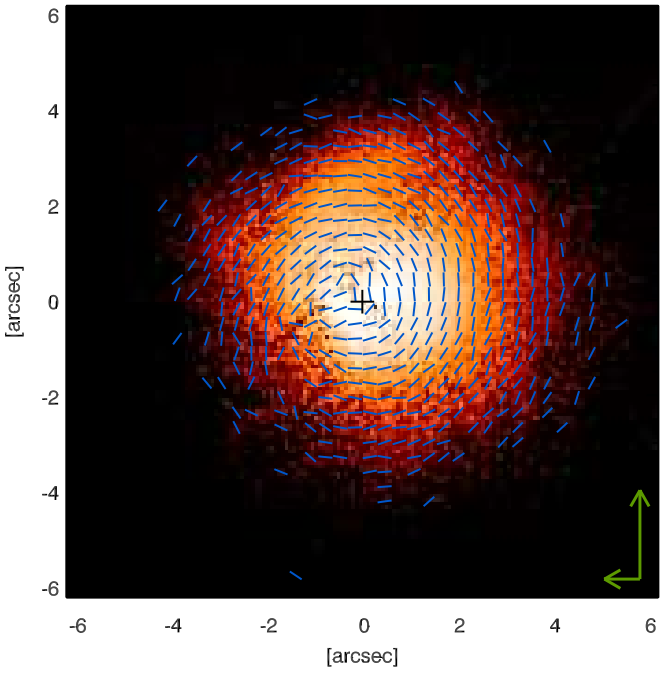

Figure 4.13: Polarized intensity image of AB Aurigae overlaid with a vector plot of the polarization direction clearly showing its azimuthal structure.

Deming, D., Brown, T. M., Charbonneau, D., Harrington, J., & Richardson, L. J. 2005, Astrophys. J., vol. 622, pp. 1149

Fukagawa, M., Hayashi, M., Tamura, M. et al. 2004, Astrophys. J. vol. 605 pp. L53

Grady, C. A., Woodgate, B., Bruhweiler, F. C. et al. 1999, Astrophys. J. vol. 523 pp. L151

Hashimoto, J., Tamura, M., Muto, T. et al. 2011, Astrophys. J. vol. 729 pp. L17

Hodapp, K. W., Suzuki, R., Tamura, M. et al 2008, Ground-based and Airborne Instrumentation for Astronomy II. Edited by McLean, Ian S.; Casali, Mark M. Proceedings of the SPIE, vol. 7014, pp. 701419

Hough, J. H. & Lucas, P. W. 2003, in ESA Special Publication, vol. 539, Earths: DARWIN/TPF and the Search for Extrasolar Terrestrial Planets, ed. M. Fridlund, T. Henning, & H. Lacoste, pp. 1117

Hough, J. H., Lucas, P. W., Bailey, J. A. et al 2006, Publ. Astron. Soc. Pac. vol. 118 pp. 1302

Keller, C. U. & Snik, F. 2009, Solar Polarization 5: In Honor of Jan Stenflo - ASP Conference Series, vol. 405 pp. 371

Keller, C. U. 2006, Ground-based and Airborne Instrumentation for Astronomy. Edited by McLean, Ian S.; Iye, Masanori. Proceedings of the SPIE, vol. 6269, pp. 62690T

Keller, C. U. 1996, Solar Physics, vol. 164 pp. 243

Kuhn, J. R., Potter, D. & Parise, B. 2001, Astrophys. J. vol. 553 pp. L189

Lagrange, A.-M. et al. 2009, Astron. Astrophys. vol. 493, issue 2, pp. L21-L25

Marois, C., Macintosh, B., Barman, T. et al. 2008, Science, vol. 322, pp. 1348

Oppenheimer, B. R., Brenner, D., Hinkley, S. et al. 2008, Astrophys. J. vol. 679 pp. 1574

Pancharantnam, S. 1955, Memoir no. 71 of the Raman research institute, Bangalore, pp. 308

Perrin, M. D., Schneider, G., Duchene, G. et al. 2009, Astrophys. J. vol. 707 pp. L132

Perrin, M. D., Graham, J., Larkin, J., et al. 2010, Adaptive Optics Systems II. Edited by Ellerbroek. Proceedings of the SPIE, vol. 7736 pp. 192

Saar, S. H. & Seager, S. 2003, Scientific Frontiers in Research on Extrasolar Planets - ASP Conference Series, ed. D. Deming & S. Seager, vol. 294, pp. 529

Schneider, J. 2010, The Extrasolar Planets Encyclopaedia (www.http://exoplanet.eu/catalog.php), consulted 30 November 2010

Seager, S., Whitney, B. A., & Sasselov 2000, Astrophys. J. vol. 540, pp. 504

Semel, M., Donati, J.-F., Rees, D. E. 1993, Astron. Astrophys. vol. 278 pp. 231

Stam, D., Hovenier, J. W. & Waters, L. B. F. M. 2004, Astron. Astrophys. vol. 428, pp. 663

Thalmann, C., Schmid, H.-M., Boccaletti, A. et al. 2008, Ground-based and Airborne Instrumentation for Astronomy II. Edited by McLean, Ian S.; Casali, Mark M. Proceedings of the SPIE, vol. 7014, pp. 112

Thalmann, C., Carson, J., Janson, M. et al. 2009, Astrophys. J. Letters, vol. 707, issue 2, pp. L123

del Toro Iniesta, J. C. & Collados, M. 2000, Appl. Opt. vol. 39, pp. 1637

Vidal-Madjar, A., Désert, J.-M., Lecavelier des Etangs, A., et al. 2004, Astrophys. J. vol. 604, pp. L69

Vidal-Madjar, A., Lecavelier des Etangs, A., Désert, J.-M., et al. 2003, Nature vol. 422, pp. 143

Wiktorowicz, S. J., Matthews, K. 2008, Publ. Astron. Soc. Pac. vol. 120 pp. 1282

Chapter 5

Imaging polarimetry of the asymmetric dust envelope around the Mira binary system

M. Rodenhuis, H. Canovas, M. Min, S.V. Jeffers and C.U. Keller[1]

Abstract

We present high-contrast imaging polarimetry of the dust shell surrounding Mira, the well-known variable binary star. The observations have been performed using the ExPo imaging polarimeter at the 4.2-m William Herschel Telescope in broadband visible light. The images have seeing-limited resolution, but still show detailed structure with evidence of clumpy outflows. We compare our observations with a model of the polarization signature expected from a dusty, bipolar outflow consisting of amorphous silicates mixed with iron. In the model, the inclination with the sky plane and the degree of bipolarity of the outflow can be varied. Our observations correspond best with a highly bipolar outflow inclined at 40° with the sky plane, with a dust grain-size distribution between 0.005 and 0.05 μm.

[1]to be submitted to Astronomy & Astrophysics, 2011

5.1 Introduction

Mira is a fascinatingly complex binary system, consisting of a companion orbiting a pulsating, cool 1.18 $M_{\odot}$ (Wyatt & Cahn 1983) giant in its AGB phase. At 128 pc (ESA 1997), Mira is the closest variable binary to Earth. Mira has been known to be a variable since the 16^{th} century (Hoffleit 1997) and is the prototype of the Mira class of variables. Its luminosity varies between 2^{nd} and 10^{th} magnitude over a 132 day period (Kholopov et al. 1998). The Mira B companion, discovered by Aitken (1923), orbits the primary with a period longer than 400 years, but the orbit is otherwise poorly known (Scardia et al. 2001). The nature of Mira B has been the subject of heavy debate for many years, with some, most recently Sokoloski & Bildsten (2010), claiming it is a white dwarf while others (e.g. Ireland et al. 2007) maintaining that it is a main-sequence star. Ireland et al. estimate the mass of the companion to be 0.7 $M_{\odot}$.

Mira B was first resolved in optical imagery using the HST by Karovska et al. (1997) and the separation was determined to be 0.58″, corresponding to a minimum distance between the components of ~70 AU. At this distance, traditional Bondi-Hoyle-Lyttleton wind accretion (Edgar 2004) predicts that Mira B will only have a localized influence on the mass flow from the primary. But the HST imagery hinted at a more substantial mass flow towards Mira B, with a hook-like appendage extending towards it, as observed at 346 nm. Long-term IR spatial interferometry observations of Mira by Lopez et al. (1997) further underlined the dynamic nature of the system with changes in visibility not only following the luminosity cycle, but also occurring between cycles. This was explained by invoking clumps in the Mira dust envelope. Radio interferometry of the molecular envelope also showed strong asymmetries, with evidence of a bipolar outflow in the North-South direction with substantially different radial velocities (Josselin et al. 2000). The dust envelope of Mira was directly imaged in the IR by Marengo et al. (2001) showing the companion to be embedded in an elongated dust envelope extending from the primary. New mid-IR observations by Ireland et al. (2007) indicate that the IR emission does not originate from a clump, but from an accreted protoplanetary disk around Mira B.

On a larger scale, a 2° long tail tracing the proper motion history of Mira has been discovered in GALEX Far-UV imagery (Martin et al. 2007). The Mira system has a high proper motion with a system velocity of 120 km/s. At distances down to a few arcmin, this tail has recently shown to be fed by a clumpy, bipolar outflow from Mira along a north-south axis with a high radial velocity difference (Meaburn et al. 2009). In this paper we present imaging polarimetry of the Mira dust envelope in broadband visible light over an area of 20″×20″. The next section describes our observations, the results of which are presented in section 5.3. The final section contains a discussion of these results.

5.2 Observations

We have observed Mira with a sensitive imaging polarimeter, ExPo, developed at Utrecht Univerity. Imaging polarimetry is a powerful technique to observe dust envelopes around stars as it is sensitive to the linearly polarized light scattered by the circumstellar material but suppresses the much brighter unpolarized starlight. ExPo operates in the visible (550 - 900 nm) and is a visiting instrument at the William Herschel Telescope on La Palma. The instrument employs the dual beam-exchange technique with a fast modulation (35 Hz) of the polarization states. This significantly reduces the sensitivity limits imposed by flat-field and seeing effects. ExPo achieves a suppression of unpolarized light by a factor of more than 10^{-4}, resulting in a contrast of 10^{-6} a few arcseconds from the star. The observations consist of large sets of short-exposure frames taken at consecutive modulator states, from which the polarization is obtained from the double-difference (Canovas et al. 2011).

The half-wave polarization modulator determines the polarization orientation that the instrument is sensitive to. Combining data taken with the modulator at two different angles with respect to the polarizing beamsplitter allows mapping the full linear polarization field. While the instrument is very sensitive to small spatial variations in polarization, the absolute polarization accuracy that can be achieved in the calibrated data is of the order 1%. Currently, the instrument operates without an AO system, resulting in seeing-limited spatial resolution.

Our Mira observations were performed on Jan 1^{st} 2010, approximately 48 days after the last maximum in the Mira luminosity cycle (figure 5.1). The average seeing during the observations was 1.24''. The images were taken through a 600 - 750 nm broadband filter. 10.000 frames were taken at each modulator angle for a total accumulated exposure time of 288 seconds.

5.3 Imaging polarimetry results

Figure 5.2 shows the linearly polarized light scattered by the Mira dust envelope. In Stokes notation, the polarized intensity equals $P = \sqrt{Q^2 + U^2}$. The positions of the two stars are indicated by a '+' (Mira A) and a '×' (Mira B) symbol. The dust envelope is clearly asymmetric and extends far out from the system when compared to the intensity image. We see what appears to be a large plume extending from Mira A in a south-easterly direction.

The structure is revealed more clearly by enlarging the polarized intensity image and overplotting it with smoothed contours (figure 5.3). As we observe at four different angles of the polarization modulator, two different polarized intensity images can be generated from two sets of observations where each set uses two modulator angles 22.5° apart. While some differences between the images can be discerned, the major features are consistent in both. The differences likely arise from changes in the atmospheric seeing conditions between the observations and calibration errors.

With our resolving power limited by atmospheric seeing, we cannot discern any

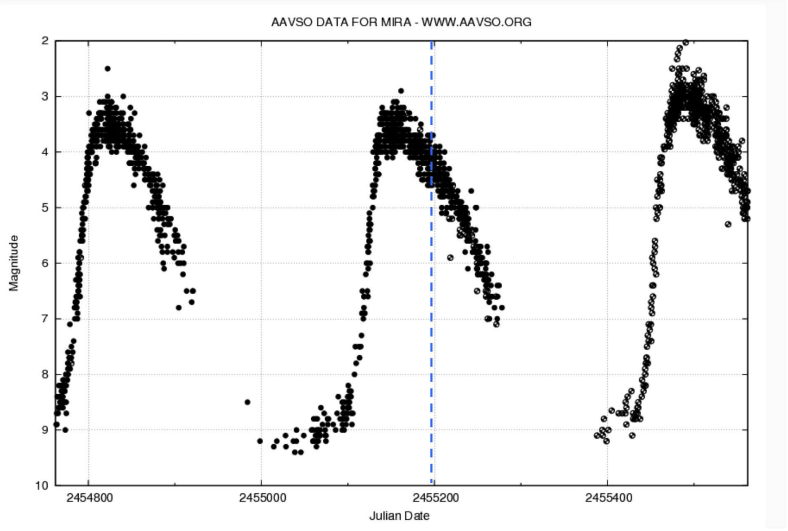

Figure 5.1: Mira light curve around the epoch of observation (dashed line). Source: www.aavso.org.

evidence of the suspected protoplanetary disk around Mira B. What we do see is a clear peak in the scattered light near but not co-located with Mira B. Lopez et al. (1997) proposed a clump in the dust shell at a distance of 0.55″ from Mira A at a position angle of 120° to explain the observed variations in IR interferometry visibility over several luminosity cycles. The peak of the polarized intensity in our data coincides well with this direction, although the distance between the Mira A and the peak is somewhat greater at 0.7″. Moreover, this peak does not appear as an isolated clump but is part of a much larger feature. Figure 5.4 shows profiles of the fractional polarization along the 120°-direction from Mira A and in the direction perpendicular to that. A large excess in the fractional polarization extends from 1″ to almost 4″ in this direction. For orientation, the direction of the cuts are indicated in figure 5.5.

Other features correspond well with earlier observations. Josselin et al. (2000) reported an east-west elongation of the observed 15″ × 20″ molecular cloud with two gaps along a roughly north-south axis from Mira A. While these gaps were observed at a distance of 4″ similar gaps can be seen in our polarized intensity images appearing as a waist-like feature of the dust cloud. The dust in the inner 0.5″ around Mira A appears to have an elongation along the axis connecting the two stars. Although this detail is below the resolution we can reliably assume for our seeing-limited observations, a similar elongation has been observed in the mid-IR by Marengo et al. (2001).

Using polarimetry we can also map the direction of the linear polarization reflected by the dust (figure 5.6). For intermediate scattering angles, we expect the orientations to be azimuthal, i.e. perpendicular to the direction to the illuminating

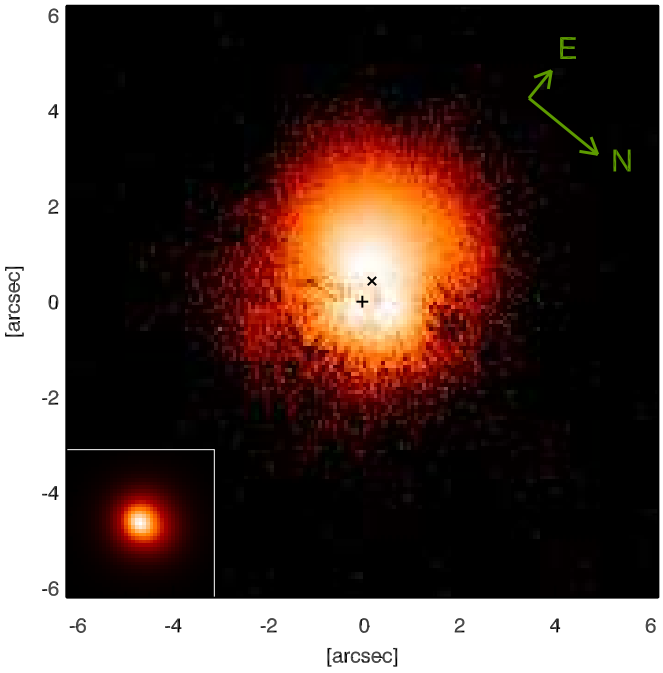

Figure 5.2: Polarized intensity image of the Mira dust envelope. Mira A and B have been marked by a + and a ×, respectively. The insert at lower left shows the intensity image at the same scale.

source. As can be seen, this is the case for large parts of the dust cloud. However in two regions, north and west of the primary, the polarization orientation is almost radial. From comet observations (Levasseur-Regourd et al. 1996) it is known that such negative polarization can occur for scattering angles in excess of 160°. In our Mira observations, these regions are thus regions where a high degree of forward-scattering predominates, evidence of the 3D structure of the dust envelope.

This can be seen more clearly when we create polar projections of the Stokes Q & U linear polarization centered on Mira A. In this projection, polarization that is oriented azimuthally around the star will be positive Q and radial polarization will be negative Q. As with regular Stokes parameters, the polarization may also have a $\pm U$ component, see figure 5.7. The projection is performed according to equation 5.1.

$$\begin{aligned} Q' &= Q\cos 2\theta - U\sin 2\theta. \\ U' &= -Q\sin 2\theta + U\cos 2\theta. \end{aligned} \tag{5.1}$$

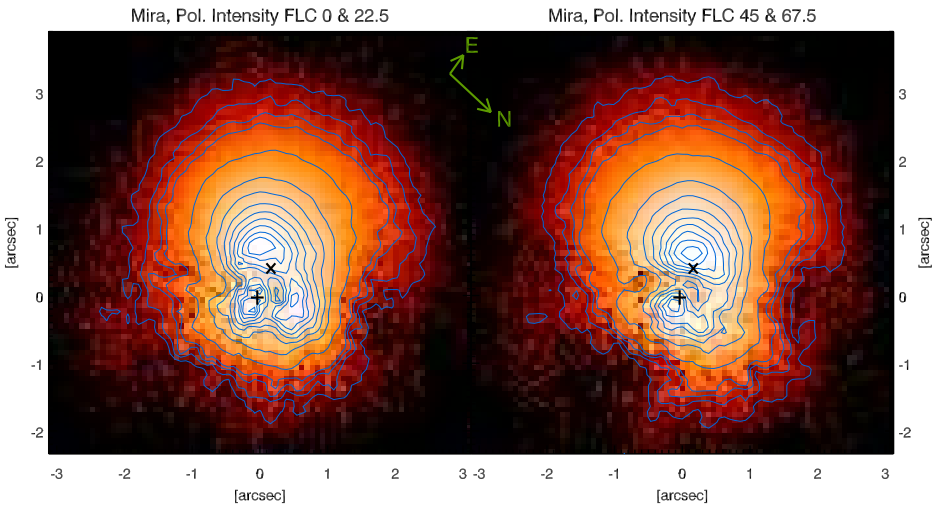

Figure 5.3: Enlarged polarized intensity images. Left: calibrated using FLC angles 0 & 22.5, Right: using FLC Angles 45 & 67.5. The '+' marks Mira A, the '×' Mira B. The smoothed contours trace the polarized intensity. First four contours are at 2%, 3%, 4% and 5% of the maximum polarized intensity, the subsequent contours are spaced at 10% intervals from 10% to 90% of the maximum.

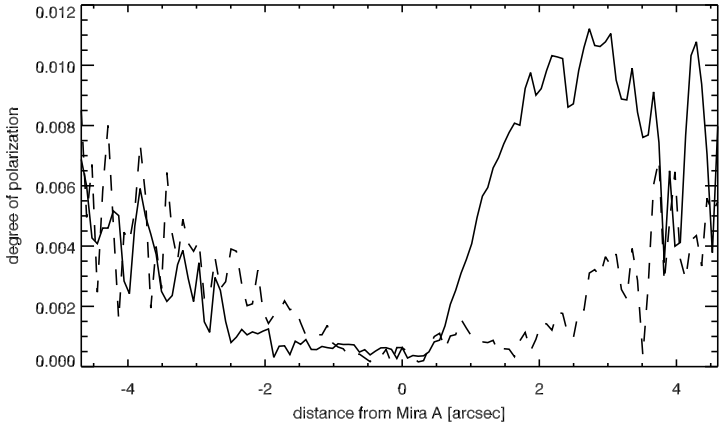

Figure 5.4: Fractional polarization along an axis with a position angle of 120° through Mira A, compared to the profile in the perpendicular direction (dashed).

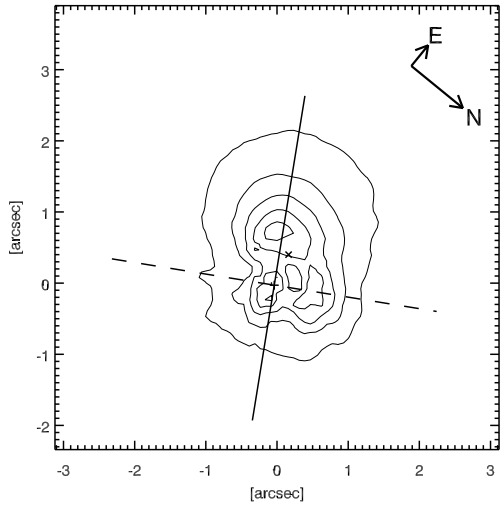

Figure 5.5: Contour map of the polarized intensity with the directions of the cuts of figure 5.4 indicated. Solid: Position angle 120°, dashed: 30°.

Figure 5.8, top row presents the polar projections of our Mira observations. The top left image shows the polar-projected Stokes Q with red indicating azimuthally oriented (positive) and blue the radially oriented (negative) linear polarization. The right-side image shows linear polarization oriented at ±45° with the radial direction from Mira A.

5.4 Modeling the bipolar structure of the Mira envelope

It is well known that outflows from (post-)AGB stars tend to have a bipolar structure; modeling of such outflow structures have been performed by García-Segura et al. (1999). To interpret our observations, we have created a model of the Mira bipolar structure and its resulting polarization structure. This model does not include the effects of the secondary star nor does it model time-dependent variability of the outflow mass flux.

The density distribution in the plane coincidental with the bipolar axis is given by:

$$\rho \sim \cos(\theta)^{\eta}. \tag{5.2}$$

Where η controls how tightly focused the bipolar flow is. We have generated

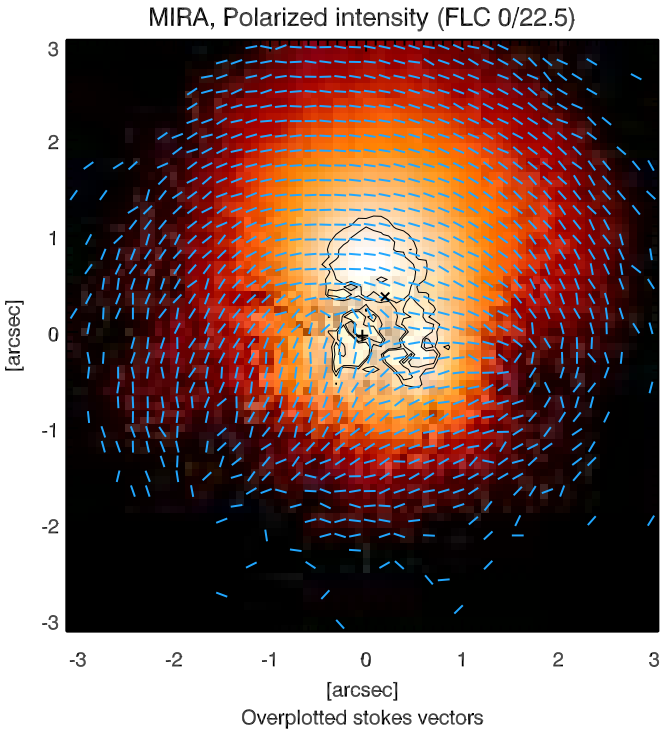

Figure 5.6: Polarization vector map of the Mira dust envelope. The background image is the polarized intensity at a logarithmic scale, with contours at 50% and 75% of the maximum that have been smoothed with a 2×2 pixel boxcar. The polarization orientation, indicated by the overplotted vectors, is only shown were the signal to noise is sufficient. The vectors are not scaled.

models with values of 0.5, 2, 4 and 6 for η. In the radial direction from the star, the density follows:

$$\rho \sim \frac{1}{r^2}. \tag{5.3}$$

The composition of the dust in our model is that derived by de Vries et al. (2010) for AGB stars and consists mostly of amorphous silicates with some iron mixed in. This composition and the amount of dust has been tuned so the simulated spectrum resembles actual spectra taken with the Short- and Long-Wavelength Spectrometers (SWS/LWS) of the ISO spacecraft (Clegg et al. 1996, de Graauw et al. 1996). The model is run as a Monte-Carlo radiation-transfer simulation (Min et al. 2009). To compare with our observations, we convolve the resulting polarization images with

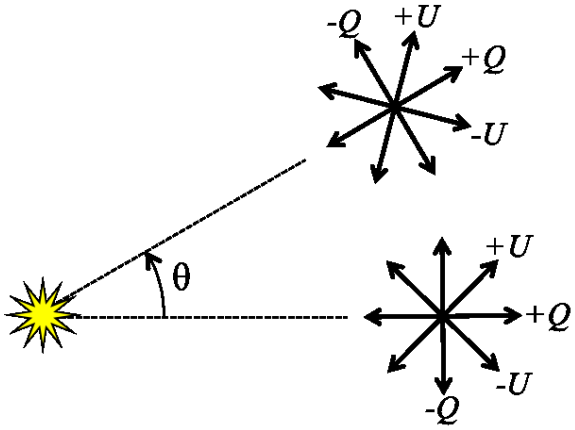

Figure 5.7: Polar-projected Stokes parameters.

the known PSF of our instrument at the William Herschel Telescope and add photon noise.

As well as varying the shape of the bipolar structure, the structure is also simulated at a range of inclination angles from 30° to 60° with the sky plane. We find very good correspondence with our observations for tightly focused bipolar outflows (η = 4, 6) at an inclination angle of 40°.

To compare with our observations, the model results (with η = 6) are presented in figure 5.8, again decomposed in polar-projected Stokes Q and U. The images have been rotated so the bipolar-axis is aligned with the 120° position angle of the observed main polarization feature. The outflow in the upper part of each image is tilted 40° away, and the lower towards, the observer.

The middle row of the image presents the results for a dust grain-size distribution according to Mathis, Rumpl & Nordsieck (1977) from 0.005-0.25 μm. In the polar-projected Stokes Q image (left) we see a large azimuthally-polarized plume associated with the back-scattering from the bipolar outflow tilted away from the observer. Small radially-polarized features (in blue) can also be seen around Mira A in the plane perpendicular to the bipolar axis, but these are much smaller than the observed regions of radial polarization. The features in the polar-projected Stokes U simulated images correspond fairly well to the observations, in particular for the outflow tilted away from the plane of the image (upper part).

As the dust density in the Mira outflow wind is known to be low (Lopez et al. 1997), the model has also been run with a grain-size upper limit of 0.05 μm. The results of this simulation are shown in the bottom row of figure 5.8. The azimuthally-polarized plume for the outflow tilted away from the observer becomes more pronounced, while that tilted towards the observer is diminished (left image). Also, the regions with radially oriented polarization are more extended, although they still do not

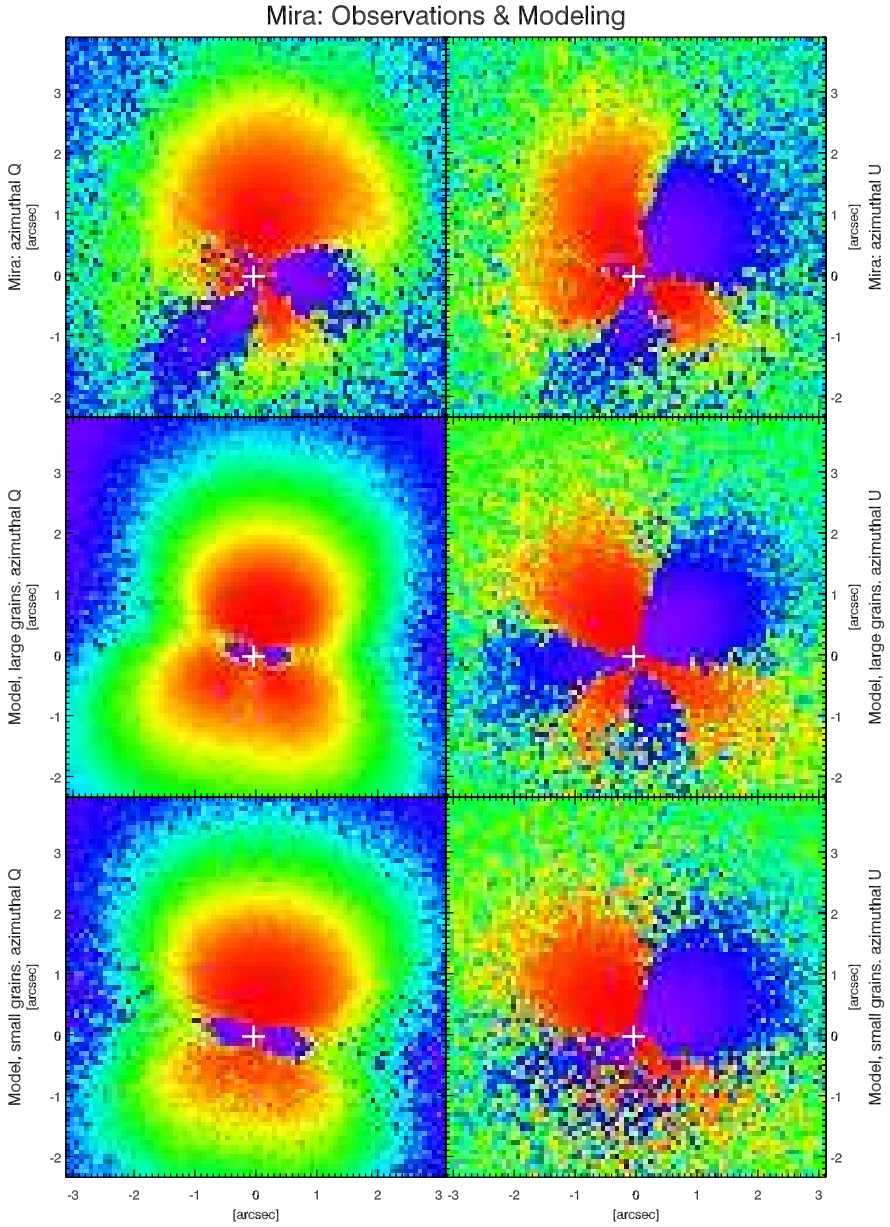

Figure 5.8: Polarized intensity of the Mira dust envelope for the observations (top) and two models of a bipolar dust outflow. Mira A is marked with a '+'. The left column shows images of Stokes Q in a polar projection around Mira A such that $+Q$ (red) indicates azimuthally oriented linear polarization and $-Q$ (blue) radial polarization. The images of the right column are of Stokes $\pm U$ polarization, oriented at $\pm 45°$ with the radial direction from Mira A. The middle row presents a model with a grain-size distribution from 0.005-0.25 μm. In the bottom row, the grain-size distribution has an upper limit of 0.05 μm.

extend as far out as those found in the actual observations. The polar-projected Stokes *U* image (right) still corresponds fairly well to the observations, although the features in the lower half, where the outflow is tilted away, are weaker and less clear.

5.5 Discussion & conclusion

The structure observed in polarized light corresponds well to the waist-like feature found through radio-observations of the CO envelope (Josselin et al. 2000), and with a clump proposed at a distance of 0.55″ from Mira A at a position angle of 120° (Lopez et al. 1997). The peak degree of polarization of this feature is observed to be 1.1%.

The large-scale structures in the imaging polarimetry can be explained with a model of a tighly-focussed bipolar ($\rho \sim \cos(\theta)^6$) outflow from Mira A, having an inclination with the plane of the sky of 40°. For the dust composition used in the model, consisting mostly of silicates with a small amount of iron, a grain-size distribution with an upper size limit of 0.05 μ fits better with the the observations compared with dust containing larger grains.

At much larger distances (127″) Meaburn et al. (2009) have observed a north-south oriented bipolar outflow with radial velocities of ±150 km/s with the South flow moving towards the observer and the North away. While this is consistent with the bipolar nature of the dust envelope presented here, the orientation is different. Our observations indicate an outflow away from the observer in the South-Easterly direction, and towards the observer in the North-West. The apparent change in orientation may of course occur over the large difference in scale of the observations.

The observations also reveal asymmetric features that cannot be explained with a symmetric bipolar outflow model. A more detailed model should include the binary companion so its effect on the dust envelope can be probed. Another effect not included in the current model is the likely, variable nature of the mass flux in the outflow.

These results shed new light on the complex Mira dust envelope and demonstrate the power of imaging polarimetry to probe and map dusty regions around stars.

5.6 References

Aitken, R. G. 1923, Publ. Astron. Soc. Pac. vol. 35 pp. 323

Canovas, H., Rodenhuis, M., Jeffers, S. V. et al. 2011, in prep.

Clegg, P. E., Ade P. A. R., Armand, C. et al. 1996, Astron. Astrophys. vol. 315 pp. L38

Edgar, R. G. 2004, New Astron. Rev. vol. 48 pp. 843

ESA 1997, The Hipparcos and Tycho Catalogues, ESA SP-1200

García-Segura, G., Langer, N., Różyczka, M. et al. 1999, Astrophys. J. vol. 517 pp. 767

de Graauw, T., Haser, L. N., Beintema, D. A. et al. 1996, Astron. Astrophys. vol. 315 pp. L49

Hoffleit, D. 1997, The Journal of the American Association of Variable Star Observers, vol. 25 pp. 115

Ireland, M. J., Monnier, J. D., Tuthill, P. G. et al. 2007, Astrophys. J. vol. 662 pp. 651

Josselin, E., Mauron, N., Planesas, P. et al. 2000, Astron. Astrophys. vol. 362 pp. 255

Karovska, M., Hack, W., Raymond, J., Guinan, E. 1997, Astrophys. J. vol. 482 pp. L175

Karovska, M. 1999, Asymptotic Giant Branch Stars - IAU Symposium vol. 191 pp. 139

Kholopov, P. N., Samus, N. N., Frolov, M. S. et al. 1998, Combined general Catalogue of Variable Stars

Levasseur-Regourd, A. C., Hadamcik, E. & Renard, J. B. 1996, Astron. Astrophys. vol. 313 pp. 327

Lopez, B., Danchi, W. C., Bester, M. et al 1997, Astrophys. J. vol. 488 pp. 807

Marengo, M., Karovska, M., Fazio, G. G. et al. 2001, Astrophys. J. vol. 556 pp. L47

Martin, D. C., Seibert, M., Neill, J. D. et al. 2007, Nature vol. 448 pp. 780

Mathis, J. S., Rumpl, W., Nordsieck, K. H. 1977, Astrophys. J. vol. 217 pp. 425

Min, M., Dullemond, C.-P., Dominik, C. et al. 2009, Astron. Astrophys. vol. 497 pp. 155

Meaburn J., Lpez, J. A., Boumis, P. et al. 2009 Astron. Astrophys. vol. 500 pp. 827

Podsiadlowski, Ph., Mohamed, S. 2007, Baltic Astronomy vol. 16 pp. 26

Scardia, M., Prieur, J.-L., Aristidi, E. et al. 2001, IAU Inf. Circ. 145, 2001

Sokoloski, J. L. & Bildsten, L. 2010, Arxiv preprint arXiv:1009.2509

De Val-Borro, M., Karovska, M., Sasselov, D. 2009 Astrophys. J. vol. 700 (2) pp. 1148

de Vries, B. L., Min, M., Waters, L. B. F. M. et al., 2010 Astron. Astrophys. vol. 516 pp. 86

Wyatt, S. P., & Cahn, J. H. 1983 Astrophys. J. col. 275 pp. 225

Chapter 6

High-contrast imaging: Reaching 10^{-8} using polarimetry

M. Rodenhuis, K. Martens, M. de Juan Ovelar, F. Snik, H. Canovas, S.V. Jeffers and C.U. Keller[1]

Abstract

Almost all of the exoplanets detected so far have been discovered using indirect methods, and the information we can obtain in this way is limited. Moreover, the radial-velocity and transit techniques that have yielded the bulk of these discoveries suffer from detection biases, being more sensitive to planets in close-in orbits with, in the case of radial-velocity detections, a high mass. Direct imaging of exoplanets will provide more information about their nature, and is also sensitive to planets at larger separations from their host star. The required imaging contrast is, however, very difficult to reach, even with advanced coronagraphic instruments.

We present a laboratory experiment combining coronagraphy with imaging polarimetry to demonstrate a contrast of 10^{-8} at a star-planet separation of 1″. The experiment is conducted using broadband visible light in ambient conditions and does not rely on active wavefront control. We show that the contrast is currently limited by systematic effects and that significantly higher contrasts can be reached if these can be removed.

[1] in preparation

6.1 Introduction

To advance the study of exoplanets, direct imaging and spectroscopy of these objects is required. Almost all of the 538 exoplanets detected to date (Schneider 2010, retrieved 13 March 2011) have been detected through indirect techniques such as radial velocity measurements or transits. While it has been possible to obtain some information on the upper atmosphere composition in a few cases (Brown 2001, Charbonneau et al. 2002, Vidal-Madjar et al. 2003, 2004, Deming et al. 2005) these detection methods only provide limited information about the vast majority of the planets discovered. Some planets have been found in what is known as the "habitable zone" around their host star, but estimates about the conditions at these planets are speculative as little is known about the albedo or atmospheric composition.

The current indirect methods also suffer from selection effects. The radial velocity technique is more sensitive to higher-mass planets in close orbits, while for the transit method, the chance of a transit is simply much higher when the planet orbits close in. Table 6.1 presents the mean minimum mass and semi-major axis for the currently known planets.

Table 6.1: Mean minimum mass ($M \sin i$) and semi-major axis of detected exoplanets. Source: (Schneider 2010, retrieved 13 March 2011).

	Number	Mass [Mjup]	Distance [AU]
Radial Velocity:	479	2.6	1.1
Transiting:	119	1.8	0.1
Directly imaged:	21	11.9	350.6

For radial-velocity detections, the orbital inclination (i) is unknown, meaning that only the minimum mass ($M \sin i$) can be determined. It is also important to note that the planet mass cannot be determined from a transit detection alone. The mean presented in the table is for the group of transit detections where the mass has been determined by radial-velocity follow-up measurements. Thus, this essentially represents a subset of the radial-velocity detections with an even smaller mean distance from the host star.

In spite of the preeminence of higher-mass planets, statistical analysis by Howard et al. (2010) of radial velocity observations of 166 sun-like stars with detected exoplanets show that the mass distribution rises towards lower masses, despite the detection bias. Correcting the distribution for this bias, they estimate that 23% of this type of stars should have planets between 0.5 and 2.0 M_{Earth}, but that 50% or more of these cannot be detected with current methods. A similar analysis by Mayor et al. (2009) based on the HARPS radial velocity survey shows that 30 ± 10% of G- and K-dwarfs can be expected to harbor planets of a Neptune mass or less in close-in orbits

($P \leq 50$ days). Comparatively few planets have been found using the microlensing technique, which suffers much less from a bias towards high-mass close-in planets. While drawing conclusion based on the small-number statistics, the planets detected with this technique at least do not contradict the proposition that lower-mass planets are more common, at least at larger separations from the star. Three times as many Neptune-mass planets than Jupiter-mass planets have been found beyond 2.5 AU using microlensing (Sumi et al. 2010).

To detect this majority of lower-mass, further-out planets and learn more about them than their periods and minimum masses, direct-imaging techniques must be developed. Direct imaging of exoplanets, however, poses formidable challenges. The separation between stars and their planets is very small, on the order of 1'' and less, and the intensity contrast between them is extreme. Earth-like exoplanets around the closest stars are expected to have contrasts of the order 10^{-10} - 10^{-11}. A small number of exoplanets have been directly imaged so far (e.g. Kalas et al. 2008, Marois et al. 2008, Lagrange et al. 2009, Thalmann et al. 2009). But these are all very massive ($>2.5\,M_{Jup}$) and at large separations (10 - 2000 AU) (Schneider 2010). Most have been imaged in the (near) infrared, where these planets exhibit significant self-luminosity and have a fairly high contrast ratio with the host star.

The high-contrast imaging techniques currently employed rely on coronagraphy; a host of new coronagraph concepts have been developed in recent years (e.g. Guyon 2003, Mawet et al. 2005, Swartlander et al. 2008) with direct imaging of exoplanets in mind. Many of these concepts can achieve contrasts of 10^{-8} - 10^{-9}, but not all are very practical, working only for narrow bandwidths or requiring extremely precise alignment.

Several space mission concepts have been proposed (e.g. Levine et al. 2009, Boccaletti et al. 2010) to detect and study exoplanets by direct imaging. Even in the absence of atmospheric turbulence, the background signal caused by diffraction from the edge of the primary mirror and speckles resulting from imperfect optics still need to be suppressed. A laboratory test-bed for such a mission, the Terrestial Planet Finder Coronagraph (TPF-C), has achieved a contrast of 10^{-10} at 4 λ/D (Trauger & Traub 2007). The test-bed uses narrowband laser light with precise wavefront control to 0.014 nm r.m.s. by a 1024-actuator deformable mirror and is housed inside a vibration-damped, temperature-stabilized vacuum chamber.

This paper presents an experiment to achieve a high contrast with imaging polarimetry in broadband visible light. Light scattered by the surfaces or atmospheres of exoplanets will become linearly polarized (Stam et al. 2004) so the polarization is a way to discriminate this light from that of the unpolarized host star. This technique is thus suitable for colder planets.

6.2 Experiment set-up

Our experiment has been conducted with the Extreme Polarimeter (ExPo), a sensitive imaging polarimeter developed at the Utrecht Astronomical Institute. ExPo

achieves high polarimetric sensitivity by simultaneously imaging the source in two orthogonal polarization states, and modulating these states between the two beams to remove systematic effects. The instrument has been used without an Adaptive Optics (AO) system to image protoplanetary disks, achieving on-sky contrasts of 10^{-5}. The instrument includes a Lyot-type coronagraph with several options for the diameter of the focal plane mask. The Lyot stop placed in the pupil of the system has a diameter of 90% of the collimated beam and also includes masking of the telescope central obscuration and spiders.

The same instrument is also used in combination with an exoplanet and circumstellar disk laboratory simulator to test and improve it. This simulator, described in chapter 3, provides two broadband point sources 1'' from each other. In the simulator, this corresponds to a separation of 30 λ/D at 640 nm. The simulated planet is linearly polarized and can be set to an intensity of 10^{-4} and less of the star. The degree and direction of this linear polarization can be controlled. The simulated star emits a photon flux corresponding to that of a $m_V = 0$ star observed through a 4.2-m telescope. The system operates at room temperature on a standard optical table.

The simulated star is not entirely unpolarized but suffers from residual linear polarization at the 10^{-4} - 10^{-5} level. In addition, the beam undergoes a 90° reflection on a aluminum-coated mirror, introducing additional linear polarization. While this complicates the experiment somewhat, it also is a realistic simulation of the tertiary mirror reflection for a Nasmyth-mounted instrument. To perform the high-contrast experiment we first adjust the angle of the Ferro-electric Liquid Crystal (FLC) polarization modulator. This element determines the orientation of the linear polarization the instrument is sensitive to (Stokes Q/U). The angle is set so the instrument is sensitive to Stokes U polarization, reducing the sensitivity to the Stokes Q introduced by the 45° mirror.

Still, the instrument will measure some residual polarization in the star. The instrument includes a polarization compensator; a fused-silica glass plate that can be tilted in the beam to reflect off excess polarization. The unit can be rotated around the optical axis to control the orientation of the linear polarization being compensated. This compensator is now adjusted until the amount of residual polarization in the star is as small as possible.

We then switch on the planet, initially at a much higher intensity than what is required for the experiment. The orientation of the planet polarization is now set to the angle for which the instrument has maximum sensitivity in this configuration. At this point the focal mask is inserted and centered in the instrument prime focus and the planet dimmed to the desired contrast using an neutral density filter wheel. A focal mask with a diameter of 1'' has been used for these measurements.

6.3 Data reduction

The FLC in the beam-exchange polarimeter modulates the polarization between two orthogonal states (A, B), while each of the two images formed by the two beams (left,

right) are recorded in every frame. To obtain the polarization image, we calculate the double-difference of the four images:

$$S_{DD} = \frac{1}{2}(S_{A,left} - S_{A,right} - S_{B,left} + S_{B,right}) \tag{6.1}$$

The intensity is calculated from the sum:

$$I = \frac{1}{2}(S_{A,left} + S_{A,right} + S_{B,left} + S_{B,right}) \tag{6.2}$$

The images are all dark-corrected before this operation takes place. For very long runs of our experiment we have noticed that the dark level fluctuates. In the dark-correction, the dark image is therefore scaled with a corner of the image. The left and right images are aligned based on the known positions of the star and planet.

The data reduction also includes an additional correction for instrumental polarization. For each left/right beam the mean of an area around the intensity peak is compared for the two consecutive modulator states and a scaled intensity image added to equalize this mean.

6.4 Results

For the experiment presented here, the planet intensity was set at 10^{-9} of the star. The contrast reached was however only slightly less than 10^{-8} and the planet was not detected. A radial cut from the star through the planet is shown in figure 6.1.

The contrast achieved at the position of the planet using just the coronagraph was 1.9×10^{-5}, so achieving a fractional polarization of 10^{-4} should have been enough to get to the 10^{-9} -level. Given enough photons, this is normally not a problem for the instrument. On-sky photon noise-limited sensitivity at this level has been achieved earlier (see chapter 4).

The experiment was run for over 80 hours, recording more than 1.4 million individual exposures of 0.2 s to ensure that sufficient margin over the photon noise was available. Clearly, the performance was not limited by the photon noise but by systematic effects. figure 6.2 shows the fractional polarization and the photon noise detection limit for the same cut as in figure 6.1.

6.5 Discussion & conclusion

While the contrast of 10^{-8} achieved is respectable, we are convinced that higher contrasts can be reached with this system once the systematic errors have been identified and removed, either by changing the instrument setup or by appropriate calibration. During an earlier stage, a systematic effect was found to be caused by

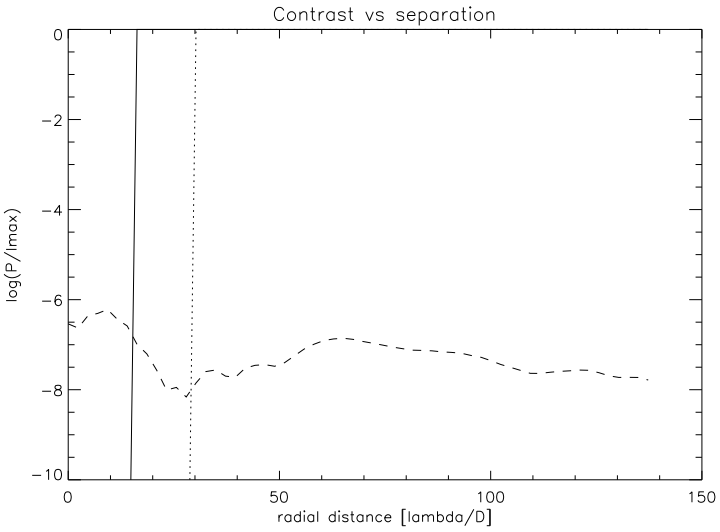

Figure 6.1: Contrast with the star peak intensity as a function of radial separation. The dotted, vertical line indicates the position of the simulated planet. The solid, vertical line indicates the edge of the focal mask.

the camera. The camera can run in two modes, with 'Frame transfer' on and off. If this mode is switched on, the camera runs in a continuous duty cycle with frames being exposed while they are transferred to the read-out memory. Without the frame transfer, exposure times are always shorter than the frame rate cycle and one or more clean cycles run in between the frames. It was, however, found that these clean cycles affect even and uneven frames differently, causing a noise signal in the resulting polarization measurement. The camera is now only run in frame-transfer mode.

The exact cause of the systematic effect affecting the results presented here is currently remains unknown. The source may lie within the instrument or within the laboratory exoplanet simulator.

Our experiment, however, clearly shows the high-contrast that can be achieved by coupling imaging polarimetry to coronagraphy. We emphasize that polarimetry is *complementary* to coronagraphy, allowing an additional reduction of the background by several orders of magnitude with respect to circumstellar sources scattering starlight. The combination of these techniques brings contrast ratios at which lower-mass exoplanets can be imaged directly within reach. The experiment however also demonstrates the need for extremely large telescopes to collect the required amount of photons to reach this sensitivity.

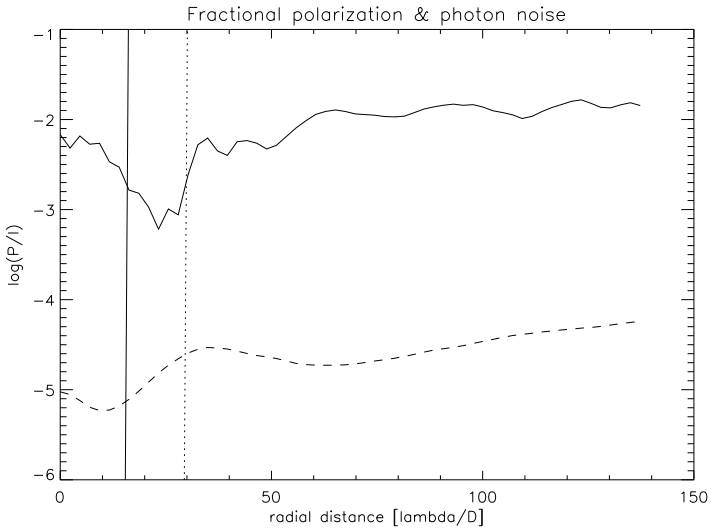

Figure 6.2: Fractional polarization (solid line) and the photon noise detection limit (dashed) with radial distance from the star. The dotted and solid vertical lines again indicate the positions of the simulated planet and the edge of the focal mask, respectively. The difference between the two curves shows that a systematic effect is deteriorating the performance and that almost two orders of magnitude in contrast can be gained if this effect can be removed.

6.6 References

Brown, T. M. 2001, Astrophys. J. vol. 553, pp. 1006

Boccaletti, A., Sozzetti, A., Schneider, J. et al. 2010, Highlights of Astronomy vol. 15 pp. 718

Charbonneau, D., Brown, T. M., Noyes, R. W., & Gilliland, R. L. 2002, Astrophys. J. vol. 568, pp. 377

Deming, D., Brown, T. M., Charbonneau, D., Harrington, J., & Richardson, L. J. 2005, Astrophys. J., vol. 622, pp. 1149

Guyon, O. 2003, Astron. Astrophys. vol. 404 pp. 379

Howard, A. W., Marcy, G. W., Asher Johnson, A. et al 2010, Science vol. 330 pp. 653

Kalas, P., Graham, J. R., Chiang, E. et al. 2008, Science vol. 322, pp. 1345

Lagrange, A.-M. et al. 2009, Astron. Astrophys. vol. 493, issue 2, pp. L21-L25

Levine, M., Lisman, D., Shaklan, S. et al. 2009 arXiv vol. 0911 pp. 3200

Marois, C. et al. 2008, Science, vol. 322, pp. 1348

Mawet, D., Riaud, P., Absil, O. et al. 2005, Astrophys. J. vol. 633 pp. 1191

Mayor, M., Udry, S., Lovis, C. et al. 2009, Astron. Astrophys. vol. 493 pp. 639

Schneider, J. 2010, The Extrasolar Planets Encyclopaedia (www.http://exoplanet.eu/catalog.php)

Stam, D., Hovenier, J. W. & Waters, L. B. F. M. 2004, Astron. Astrophys. vol. 428, pp. 663

Sumi, T., Bennet, D. P., Bond, I. A. et al. 2010, Astrophys. J. vol. 710 pp. 1641

Swartlander, G. A., Ford, E. L., Abdul-Malik, R. S. et al. 2008, Optics Express vol. 16 pp. 10200

Thalmann, C. et al. 2009, Astrophys. J. Letters, vol. 707, issue 2, pp. L123

Trauger, J. T., Traub, W. A. 2007, Nature vol. 446 pp. 771

Vidal-Madjar, A., Désert, J.-M., Lecavelier des Etangs, A., et al. 2004, Astrophys. J. vol. 604, pp. L69

Vidal-Madjar, A., Lecavelier des Etangs, A., Désert, J.-M., et al. 2003, Nature vol. 422, pp. 143

Chapter 7

First detection of ring-like polarized features in the atmosphere of Venus

M. Rodenhuis, F. Snik, D. Stam, R. de Kok, H. Canovas, M. de Juan Ovelar, S.V. Jeffers and C.U. Keller[1]

Abstract

We present broad- and narrowband imaging polarimetry of the Venusian atmosphere in the visible. The observations were made using the ExPo instrument at the William Herschel Telescope on La Palma at a Venus phase angle of 48.7°. We detect increased scattering polarization in the sub-polar regions surrounding the polar vortex known from prior observations. The atmosphere in these regions is known to have an inverted temperature profile resulting in very cold upper atmosphere layers and correspondingly smaller condensed particles. The scattering regions appear both in broad and narrowband imaging. In the narrowband observations, conducted while the atmospheric seeing was 0.8″ or better, we also observe ring-like structures. To our knowledge, this is the first time such features have been observed. The origin of these rings is not yet known.

[1] in preparation

7.1 Introduction

The sulfuric acid haze particles in the Venusian atmosphere polarize scattered light and it therefore is no surprise that polarimetry has been used for decades to study this atmosphere. A polarimeter was used to study Venus as early as 1922 (Lyot 1924). Dollfus & Coffeen (1970) noticed changes in ultra-violet polarization over a period of years while the changes during a Venus diurnal period were small, inferring that the scattering particles must be well distributed in the atmosphere, but subject to some global dynamical process. Using a polarimeter on board the Pioneer Venus probe, the haze particles have been shown to be 1 μm-sized spherical droplets of sulfuric acid (Hansen & Hovenier 1974).

Travis et al. (1979) observed increased polarization around the poles while the optical thickness of the upper cloud layer was measured to be higher poleward of 55° latitude (Kawabata et al. 1980). This has been interpreted as evidence for Hadley cells in the atmospheric circulation of Venus (Svedhem et al. 2007). Several observers (O'Leary 1966, Können et al. 1993) have seen indications of a (disk-integrated) 22° halo effect caused by hexagonal ice particles in the upper atmosphere, but no definitive confirmation of this has been published to date.

Extensive observations with the Venus Express probe (Titov et al. 2008) have revealed strong vortices on both poles of Venus, surrounded by a band roughly between latitudes 55° and 75° with an inverted temperature profile, resulting in a comparatively cold (210 K, Piccioni et al. 2007) cloud layer in the upper atmosphere.

This paper presents recent ground-based imaging polarimetry of the Venusian atmosphere at different wavelengths, using both narrow and broadband filters. We detail the methods of our observations in the next section. This is followed by the presentation and discussion of our results. Some preliminary conclusions are made in the final section.

7.2 Observations

Our Venus observations have been carried out with the ExPo imaging polarimeter installed at the William Herschel Telescope on La Palma. This instrument has been designed for the observation of faint, linearly polarized light scattered by circumstellar material. The instrument is very sensitive to linearly polarized light, capable of reaching a sensitivity of 10^{-4} provided sufficient photons are available. At present, no Adaptive Optics system is used, resulting in seeing-limited spatial resolution. Details of the instrument design and performance are given in chapter 4. Canovas et al. (2011) provide a description of the data reduction pipeline.

The observations were performed during twilight on 24 May 2010. At this time, the Venus phase angle was 48.7° and its angular diameter 12.5''. Six different filters were used, four narrowband and two broadband. The filter specifics are found in Table 1. The narrowband filters, normally used to study atomic spectral lines, were simply the available filters. The results we report are not suspected to be caused by

physical effects in the corresponding spectral lines.

For each filter, observations were made at four angles (0°, 22.5°, 45°, 67.5°) of the Ferro-electric Liquid Crystal (FLC) polarization modulator. This modulator alternates between two states (A & B) that introduce rotations of the linear polarization by ±45°. This allows switching of orthogonal polarization states between the two beams of the polarimeter, canceling out first-order systematic effect caused by differences in the optical path between them. The switching is synchronized with the 35 Hz frame rate of the camera. This fairly high switching speed reduces the effect of variations in atmospheric seeing between consecutive frames. Two measurements using FLC modulator angles spaced 22.5° apart are required to produce a calibrated map of the linear polarization field. Both the Q and U parameters in the Stokes polarization notation can then be determined. The observations at four FLC modulator angles therefore produce two redundant datasets.

Table 7.1: Venus observation filters

Filter name	Central wavelength [nm]	Width [nm]
H-alpha	656.3	1.0
H-alpha cont.	647.1	1.0
Na	589.4	5.0
Na cont.	580.0	5.0
Sloan i	762.5	152.6
Sloan r	623.1	137.3

7.3 Image processing

The observations for each FLC modulator angle consist of 5000 frames with an exposure time of 28.8 ms each in which the two modulator states (A & B) alternate. Each frame contains two images (left & right) at orthogonal polarizations. The linear polarization image is extracted from these frames through the so-called (Bagnulo et al. 2009) 'double-difference' (Eq. 7.1)

$$S_{DD} = \frac{1}{2} \sum_{\text{frames}} (S_{A,\text{left}} - S_{A,\text{right}} - S_{B,\text{left}} + S_{B,\text{right}}) \tag{7.1}$$

The images must be carefully aligned before this combination can be performed. We have done this by calculating the 'center of intensity' for each individual frame

(Eq. 7.2).

$$R_I = \frac{\sum I_i \mathbf{r}_i}{\sum I_i} \tag{7.2}$$

Calibrated Stokes Q and U polarization images are calculated by combining two double-difference images taken at FLC modulator angles 22.5° apart (Eq. 7.3).

$$\begin{pmatrix} Q \\ U \end{pmatrix} = \mathsf{M} \cdot \begin{pmatrix} S_{DD}^{FLC1} \\ S_{DD}^{FLC2} \end{pmatrix} \tag{7.3}$$

The calibration matrix M is generated by combining dome flats with a calibration polarizer at four different positions (Stokes $\pm Q$ and $\pm U$ at the two different FLC angles. The details of this procedure are given in chapter 4. The accuracy with which the degree of polarization can be determined in this way is 1%. The calibrated Q and U images have finally been corrected for sky polarization.

We have also created maps of the observed polarization by projecting the images onto a regular latitude-longitude grid. To do this, the sub-observer point (center of disk) must be determined for each observation. We first generate an image of the Venus limb by summing the absolute values of the derivatives in x- and y-direction. Along the limb, we perform a Hough transform using circles with the estimated disk radius with a width of 3 pixels. Having thus obtained the center the radius to each point along the Venus limb is calculated. This is not constant, as there is a slight optical projection effect in the images. A sine is fitted to the radius profile along the limb to find the degree and direction of the compression, after which the images are deprojected.

The actual mapping can now take place by calculating the latitude and longitude for each pixel on the Venusian disk. The North polar angle and inclination are obtained from JPL Horizons ephemeris data (retrieved from http://ssd.jpl.nasa.gov/?horizons). The pixels are then placed on the latitude-longitude grid and the remaining map pixels added using a nearest-neighbor approach.

7.4 Results

In all our observations we see increased polarization in regions near both poles. A second feature, observed only in the narrowband images, is an intriguing structure consisting of several thin rings extending across the illuminated disk of Venus. Calibrated polarized intensity images are shown for all filters in figure 7.1.

The rings are detected in three of the narrowband filters but not in the Sodium continuum filter. To ascertain whether the filters are truly global features, we have tried subtracting scaled images in which the rings do not appear from the images with rings. The large polar features are, however, not quite the same in the different images and it was not possible to clearly isolate the rings in this way. Nevertheless,

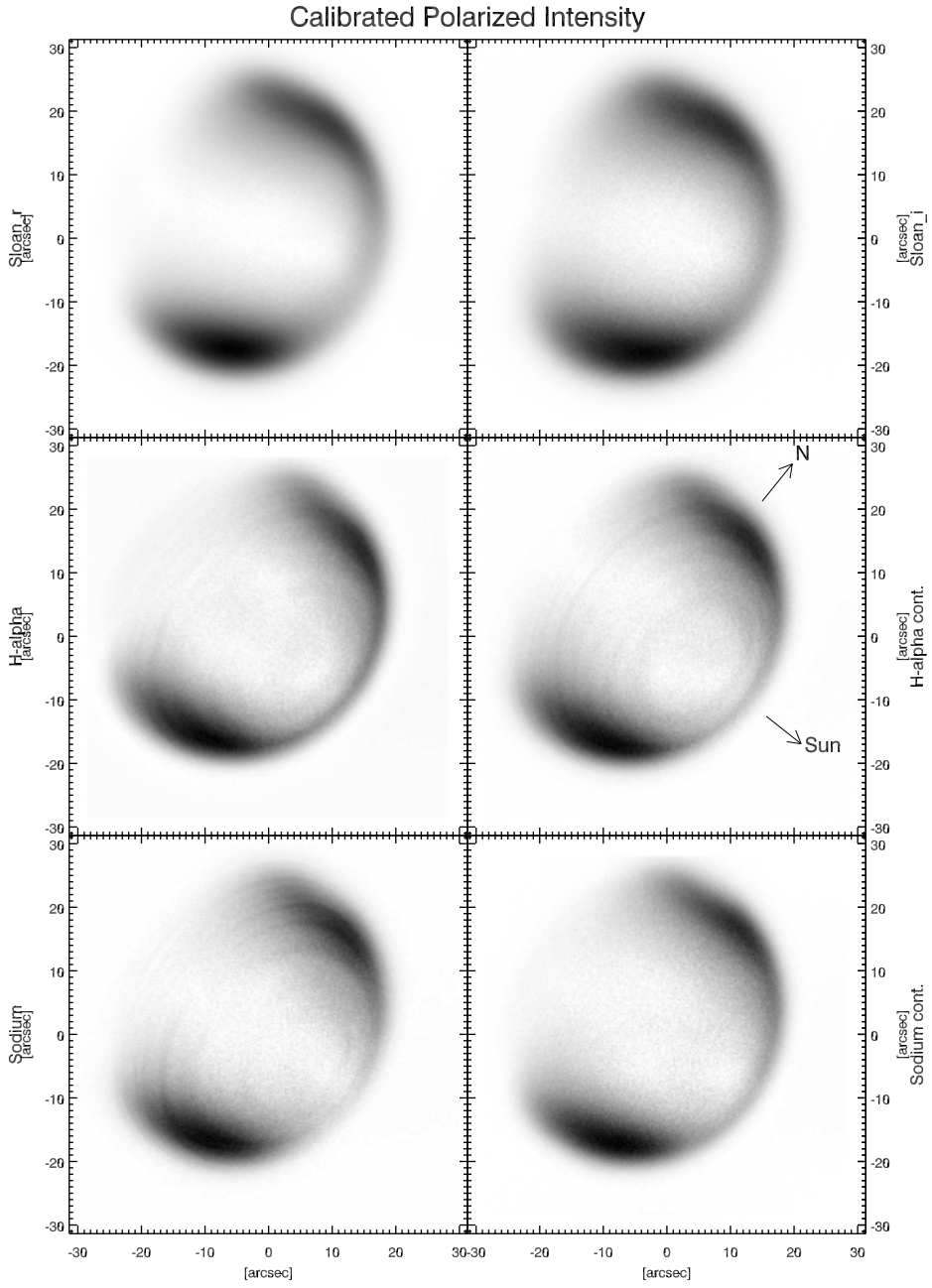

Figure 7.1: Venus calibrated polarized intensity for all filters. First row are the broadband measurements: Sloan *r* (left) & Sloan *i* (right). Middle row: narrowband H-alpha & H-alpha cont. Bottom row: narrowband Sodium & Sodium cont. The negative images are plotted for better contrast. The North and Sun directions are indicated for all images in the middle left pane.

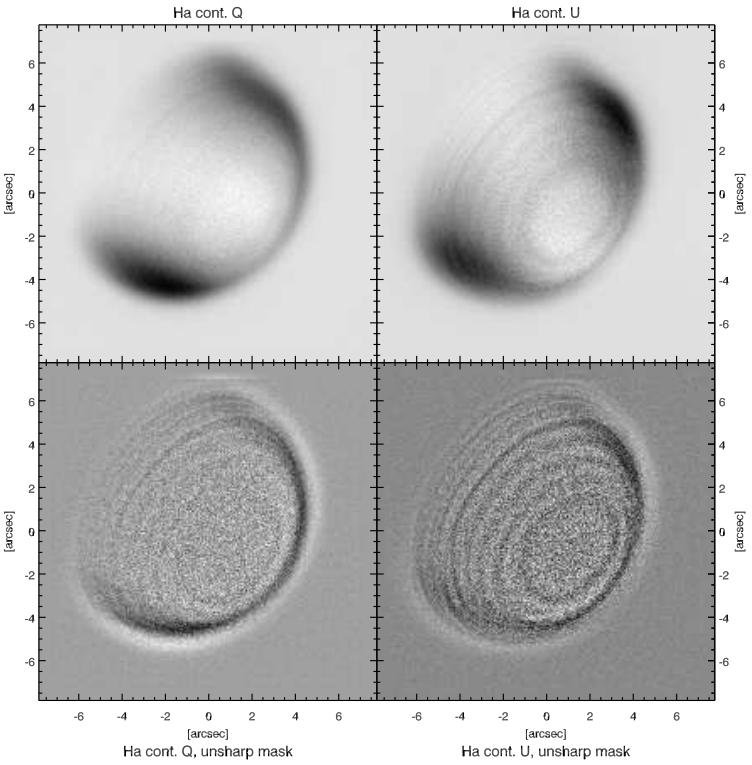

Figure 7.2: Calibrated Stokes Q and U images (top) and with an unsharp mask subtracted (bottom).

in images where we have subtracted an unsharp mask (figure 7.2), the rings clearly appear as global features. Moreover, in the calibrated Stokes Q and U images, the rings appear constant, meaning the orientation of the linear polarization does not change significantly along the rings.

From the polarization images it seems the rings may be concentric around the sub-solar point, but mapping the images onto a latitude-longitude grid shows that this is not quite the case. For the H-alpha filter, this map is shown in figure 7.3. In Stokes notation, the polarized intensity has been calculated according to Eq. 7.2.

$$P = \sqrt{Q^2 + U^2} \tag{7.4}$$

From the generated latitude-longitude maps, it becomes clear that the rings are not centered on the sub-solar point, but follow intensity contours. The intensity maximum is approximately half-way between the sub-solar point and the point for maximum specular reflection. The radius of the innermost ring is around 20°, after

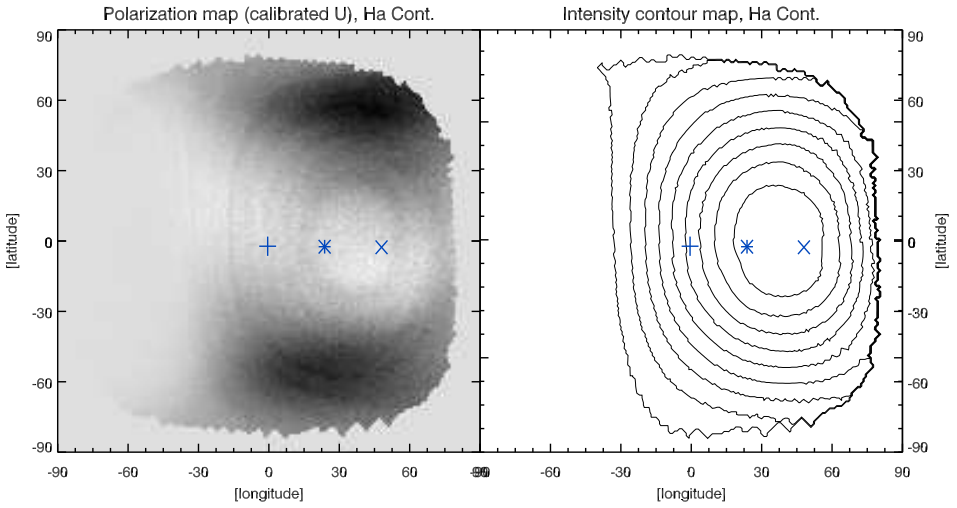

Figure 7.3: Map-projected polarized intensity & intensity contours. Points marked in intensity contour map: Sub-observer point (+), sub-solar point (×), point of maximum specular reflection (*). Images are for the FLC67 position in the H-alpha cont. filter.

which the next rings appear at intervals around 9°. Towards the terminator, the rings are more closely spaced.

Comparing the broad- and narrowband intensity images overplotted with intensity contours (figure 7.4) we see that the global shape is the same. While the polarized rings appear to trace the intensity contours, the intensity gradient alone is not sufficient to produce the rings.

To compare the ring structure in the different filters we isolate the equatorial regions from the latitude-longitude maps, removing everything North and South of 30° latitude (figure 7.5). These maps are overplotted with the calibrated Stokes U/I polarization, averaged over the region ±5° North and South of the equator. The rings are predominantly negative Stokes U features, and are much less visible in Stokes Q.

In the comparison, the rings are clearest in the H-alpha and H-alpha continuum filters. Note that these have a narrower bandpass than the Sodium and Sodium continuum filter (Table 1). The rings are clearly linked to an increase of a few tenths of percent in negative Stokes Q polarization. Note that due to the calibration accuracy of 1%, there may be a significant offset to the Q/I values indicated on the scales.

It is not clear whether the positions of the rings are constant or exhibit a wavelength-dependent shift. The two most prominent rings in the H-alpha and H-alpha continuum filters appear slightly shifted, but the wavelength difference between these filters is only a few nm.

Using the calibrated images, the polarization direction can be superimposed as

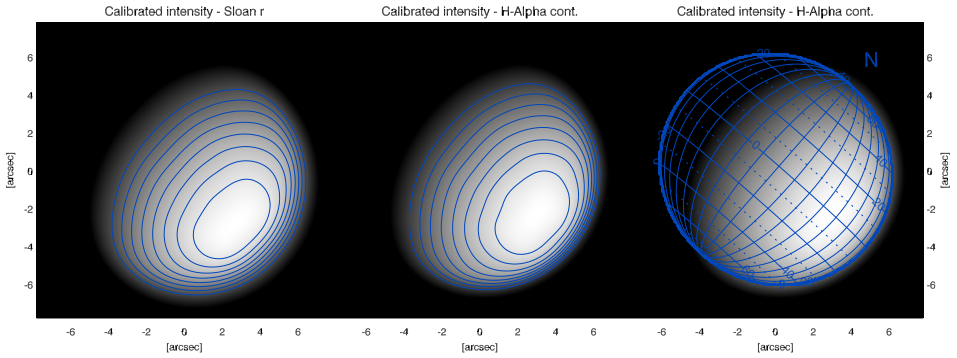

Figure 7.4: Intensity in broad- and narrowband and an image with latitude and longitude contours.

vectors onto the polarization images (figure 7.6). For visible light from green to red wavelengths, the orientation of the polarization is expected to be *parallel* to the scattering plane due to the scattering properties of the spherical haze particles (Coffeen & Gehrels 1968). This is indeed the result we obtain for most of the Venusian disk, although there is some rotation of the polarization orientation between the limb and the terminator side of the polar regions. As expected, the polarization orientations are also more or less symmetrical with respect to the equator.

Clearly, the degree of polarization becomes higher moving from the equator towards the poles. The maximum degree of polarization found in the narrow band around the Venus equator dominated by the rings is of the order 0.2%.

We have sampled and binned pixels from different parts of the most prominent ring features to probe the polarization orientation in the rings and find that it is also aligned parallel to the scattering plane, consistent with the negative Stokes U peaks at the ring locations seen in figure 7.5. The orientation of the ring polarization furthermore appears constant along the rings, which is supported by the fact that the intensity along the rings is fairly constant in the Stokes Q and U images.

Figures 7.7 & 7.8 show maps of the degree of polarization in both broadband and narrowband. The observed degrees of polarization are less than 2%. Clearly, the areas of peak degree of polarization are poleward of ±60° latitude, but do not reach all the way to the pole. The topography of the polarization in the polar regions and the degrees of polarization measured are similar in the narrow- and broadband observations. The degree of polarization at the north pole is slightly higher towards the blue, at least in the broadband observations. The west/eastwards shift of the polarization peak at the north/south pole is peculiar. While it might appear as a rotation error in the map projection, the intensity map shows no sign of this.

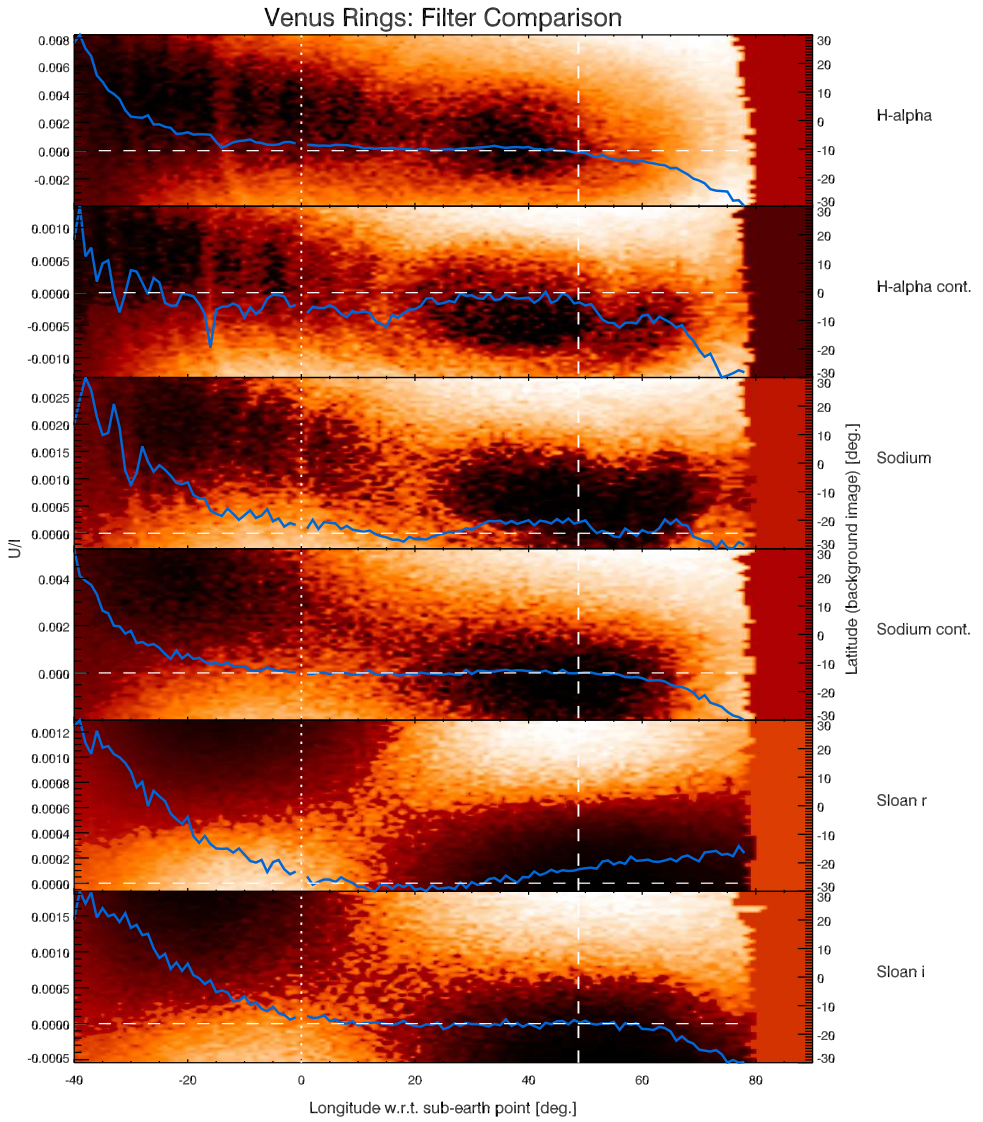

Figure 7.5: Comparison of rings in different filters. The background images are Stokes U for latitude between -30° and 30°. The Stokes U/I is plotted on top of the images, averaged over the region between 5° and 5° of latitude. The scale is shown at the left side. The dotted line indicates the sub-Earth longitude, the dashed line the sub-solar longitude.

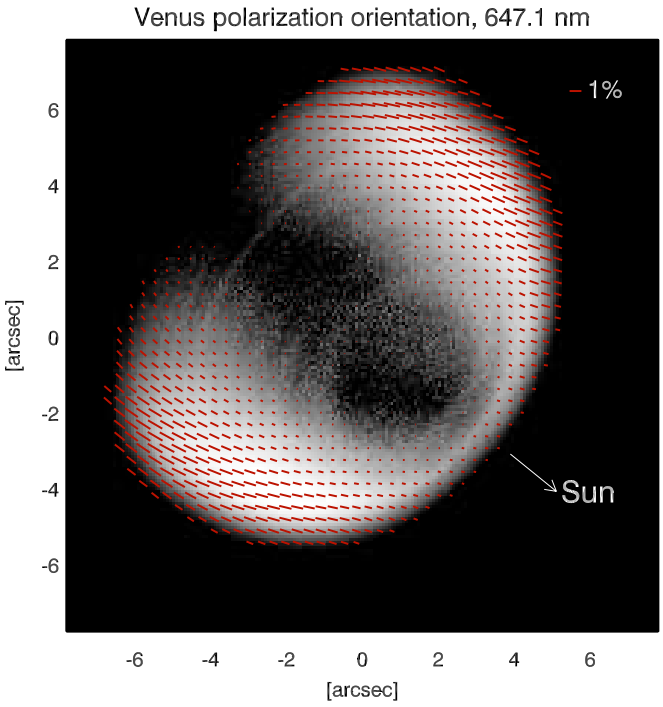

Figure 7.6: Calibrated polarized intensity image overplotted with vectors indicating the polarization orientation. The vectors are scaled with the degree of polarization.

7.5 Discussion

7.5.1 Increased polarization in the polar regions

The increased polarization observed in the polar regions agrees well with the prior observations by Coffeen & Gehrels (1968), Travis et al. (1979), Kawabata et al. (1980) and Knibbe et al. (1992) and indicates higher scattering polarization by condensed particles in the cold sub-polar regions.

Both the degree of polarization of less than 2% in the polar regions and its orientation are consistent with the observations of Coffeen & Gehrels (1968) at 520 nm. The brightness of the polar regions is known to vary (Kawabata et al. 1980, Svedhem et al. 2007) and the degree of polarization we measure, though quite low, is within the range found by other observers (Travis et al. 1979). The increasing (negative) polarization towards the poles is consistent with smaller haze particles (Hansen & Hovenier 1974). The fact that the polarized regions do not reach all the way to the

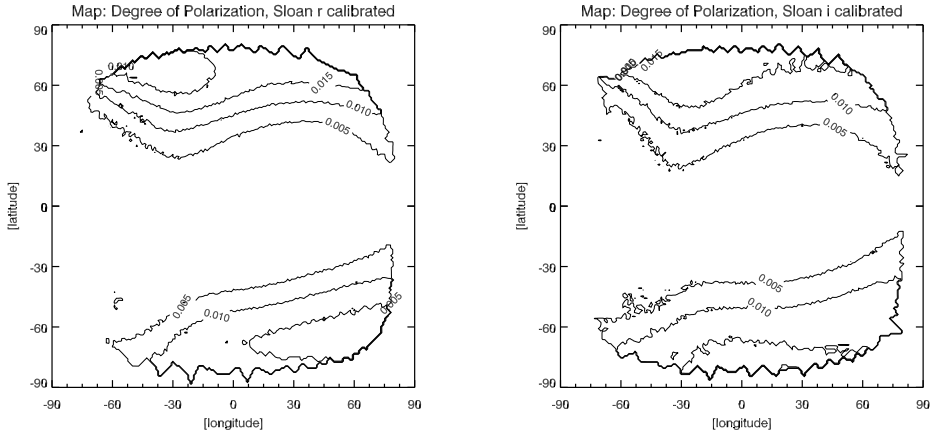

Figure 7.7: Comparison of the degree of polarization in the polar region in the two broadband filters.

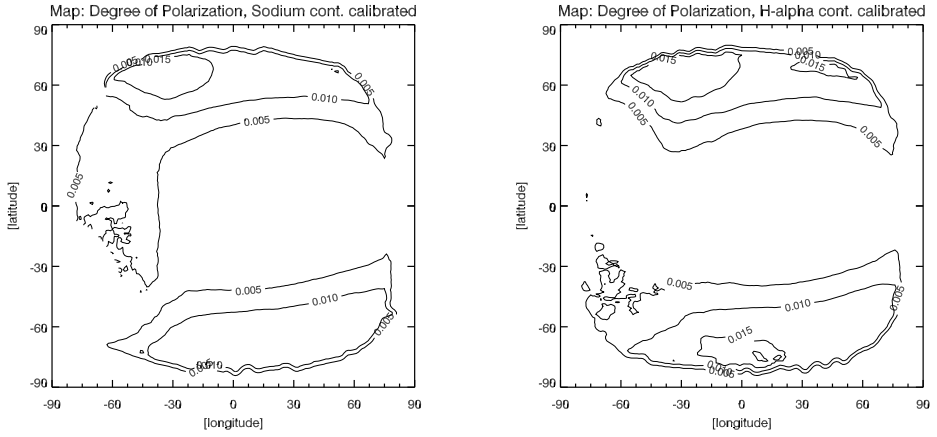

Figure 7.8: Comparison of the degree of polarization in the polar region in the two narrowband filters. As the images are noisier than the broadband images, the contours have been slightly smoothed.

poles corresponds to the observation of a cold collar around the comparatively hotter polar vortices (Titov et al. 2008).

7.5.2 Polarized rings: An instrumental effect?

A number of scenarios have been analyzed to test whether the polarized rings could be the result of an instrumental effect, but so far such a cause has not been identified. An instrumental cause would have to fall in one of two categories:

1. An optical effect within the instrument
2. An effect introduced by the data reduction process

As ExPo observations consist of large numbers of short-exposure dual-beam images that must be aligned and combined to generate the polarization image, a cause in the latter category might be suspected. It would however be peculiar if such a problem would affect only the narrowband and not the broadband images. Nonetheless, an alternative way to process the images was tested.

In stead of aligning the individual frames on the 'center of intensity' we have also processed the images using the standard approach to aligning ExPo imaging polarimetry of stellar sources. Here, the individual frames are aligned according to the best correlation with an average image. The results are however almost identical to the centroiding approach and the ringlike structures still show up clearly.

Investigating possible optical effects and noting that ExPo is a dual-beam polarimeter, one might suspect a differential effect such as a focus difference in the the two beams. This is however unlikely: A key feature of the ExPo instrument is its employment of the beam-exchange method. The polarization modulator switches the orthogonal polarization states between the two optical paths, canceling out first-order effects in the differential aberrations between them on the polarization measurements. An instrumental effect should therefore be looked for upstream of the polarization beamsplitting.

An optical effect such as polarized fringes would be expected to be constant in relation to the instrument or rotate with the FLC polarization modulator. Fringes in a constant position and orientation with respect to the instrument optical axis should appear most clearly if all the individual sub-images used to generate the polarization images are cut from fixed areas of the raw frames. In fact, one would expect the any shifting to align the frames to negate or at least smear out and thus dampen any polarized fringes. To verify this, we have also generated a double-difference polarization image using a fixed alignment for all individual frames (figure 7.9).

The rings are completely gone. The only remaining feature is the central dark oval area, corresponding to the area within the innermost ring. Clearly, the images must be very precisely aligned to see the rings. But due to difficulty in guiding on such an extended source, the amounts of shift that must be applied to the individual frames is not the same for all narrowband observations. In fact, the guiding was corrected at some point during the observations when the guiding had drifted to the point where the Venus disk was getting close to the edge of the field-of-view. In addition, the amount of tip-tilt introduced by the atmospheric seeing varied during the observations. Yet when aligned, the rings show up very similarly in the narrowband images.

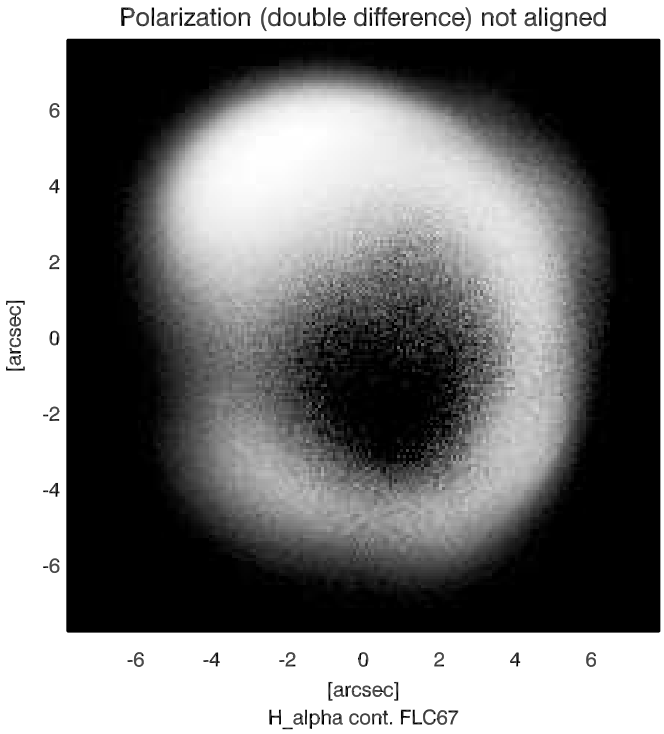

Figure 7.9: Double-difference polarization image generated with a fixed alignment for all frames.

This leaves us with an optical or electronic effect that is caused by the intensity gradient itself. But as shown by figures 7.3 & 7.4 this intensity gradient is also present in the broadband images and the narrowband Sodium continuum.

We have also investigated whether an intensity-related electronic effect might be the cause of the rings. If the camera analog-digital converter has a bit error where the digitally recorded intensity values skips some count values, the discrete intensity steps might end up as rings in the polarized images. A large number of digital count histograms of the raw data were checked, but no such systematic effect was encountered.

A final piece of evidence that the observed polarized rings may well be real is provided by the narrowband Sodium continuum observation and the sequence in which the observations have been made. The Sodium continuum filter was the last narrowband filter to be used, after which the broadband observations were performed. By this time, Venus was starting to set and the telescope elevation was very low. While the rings may still be a narrowband effect, an alternative explanation

may be that they are also visible in broadband, but may have become smeared by the deteriorating seeing by the large airmass. But if this is true, the cause of the rings must be sought on Venus itself.

7.5.3 Polarized rings: A halo effect?

In the terrestrial atmosphere, polarized halos caused by scattering by particles with a preferential geometrical shape and/or alignment are well known. For the Venus rings, the polarization scattering angle is constant along the rings, as is the orientation of the resulting polarization. Even if there would be a layer of crystalline (ice) particles with hexagonal or cubic structure and aligned with the local zenith direction, it is not clear how this could create the observed polarization features (Können, 2011, private communication). It would also be difficult to explain how aligned crystalline particles could cause so many rings. Finally, one would expect the particle density and orientation to show some variation, but the rings appear as a global feature.

7.5.4 Intensity gradient and optical depth effects

The fact that the rings appear to follow intensity contours (figure 7.3) appears to be the key to their origin. The intensity gradient over the observed Venus disk is interesting on its own accord. The location of the peak intensity point, away from the sub-solar point is notable, and we have been unable to find much discussion of this feature in the literature. Figure 7.10 compares contours of intensity and the cosine of the local solar zenith angle. The intensity shows a marked shift.

From the fundamental optical reciprocity principle stated by Helmholz, Minnaert (1941) has derived an expression for the scattered intensity based on the cosines of the angles of the incident and scattered beams with the local zenith direction (μ_{in}, μ_{out}).

$$I\mu_{\text{out}} = I_0(\mu_{\text{out}}\mu_{\text{in}})^k \tag{7.5}$$

While Minnaert's work relates to the scattering from solid surfaces, this relationship has also been used in the study of planetary atmospheres (e.g. Sromovsky et al. 1981). The exponent k, refered to as thet 'limb-darkening parameter' by Sromovsky et al., is a measure for the degree in which optical depth effects play a role in the scattering process. The value of k can be found by plotting $I\mu_{\text{out}}$ versus $\mu_{\text{out}}\mu_{\text{in}}$ on a log-log scale for a large number of points on the disk and fitting a straight line. Performing this analysis at different wavelengths or different regions of the atmosphere can yield information about the atmospheric structure.

We show this plot for the calibrated intensity image through the H-alpha continuum filter if figure 7.11.

This plot is not precise enough to accurately fit a value for k; Points of equal latitude (equal color in the plot) should follow the same trend. We see there is some variation which may be due to errors in the mapping. We do note that the

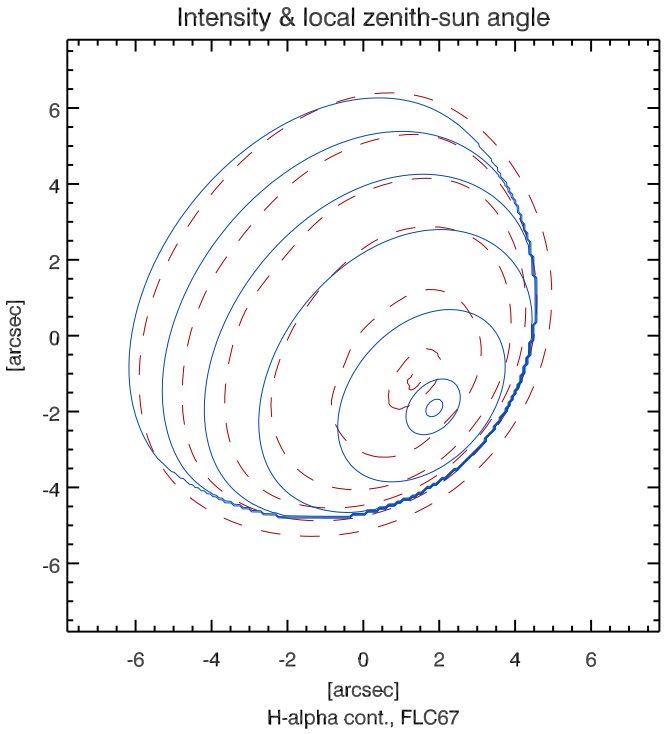

Figure 7.10: Contours of intensity & local solar zenith angle.

global gradient of the plot, and thus the value of k, is close to 1, corresponding to a Lambertian scattering process. The gradient appears to decrease towards the poles, implying a decrease in scattering anisotropy.

While the Lambertian scattering does not in itself imply optical depth effects, the fact that the rings trace the intensity directly links them with global scattering effects. As the intensity is produced by scattering in the Venus atmosphere, it is likely that the ring-like polarization features are due to a combination of scattering effects and a global, highly inhomogeneous stratification in the layers that we observe.

7.5.5 Polarized rings: Stratification in the Venus atmosphere?

With the observed polarized rings tracing intensity contours and the intensity gradient caused by optical depth effects, we now speculate that the rings may originate from stratification in the Venusian atmosphere. Indications of such a stratification has been observed in-situ by descending probes (Lacis & Hansen 1974). The optical depth traversed by the scattered light depends on the angle of incidence of the incom-

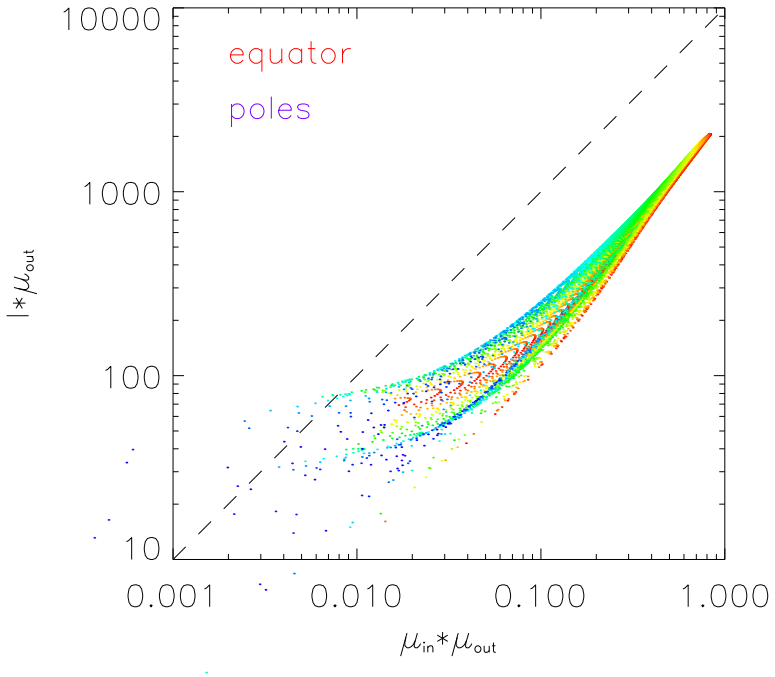

Figure 7.11: Minnaert scattering plot. Points have been color-coded according to latitude, ranging from red at the equator through yellow, green and blue to purple at the poles. The divergence towards lower left is likely due to errors in the map projection.

ing and outgoing rays. As different areas in our images probe the Venus atmosphere at slightly different depths, atmospheric layers that are thin in height but global in horizontal extension might be the origin of the rings.

Clearly, this is no more than a initial idea based on qualitative arguments. Detailed radiative transfer modeling of these effects must be performed before anything can be concluded about the origin of the polarized rings with any certainty.

7.5.6 Why have the polarized rings not been observed before?

Polarimetry is a common tool in the study of the atmosphere of Venus. But many of the ground-based observations have been conducted in broadband light and have searched for disk-integrated effects at certain phase-angles (e.g. Können et al. 1993). The polarimeter carried on board the Pioneer Venus orbiter supported an imaging polarimeter mode (Travis et al. 1979), but it is not clear that the sensitivity would

be sufficient to detect the rings. Moreover, the viewing geometry from the orbiting instrument would be very different. The instrument was used mostly in a scanning mode resulting from the 5 r.p.m. spin rate of the spacecraft. The instrument carried a range of filters, but none of them were narrowband.

To our knowledge, no imaging polarimeter with the sensitivity of ExPo has been used to study Venus before. Our results have clearly also benefited from the excellent seeing during the observations. We believe this may explain why these structures have not been seen before.

7.6 Conclusion

We have observed a previously unknown ring-like polarization structure in the atmosphere of Venus that we believe is real, although the nature is not yet understood. The other polarization structure detected in the polar regions corresponds well with other observations and is understood to originate from a haze of condensed particles in this relatively cold region of the atmosphere.

To confirm our detection of polarized rings, detailed radiative-transfer modeling of the atmosphere of Venus is required including polarization effects. We also plan follow-up observations, including using an alternative instrument.

Our observations demonstrate the utility of sensitive imaging polarimetry in studying the complex scattering and optical-depth effects of dynamic planetary atmospheres. Besides ground-based observations, modern polarimeters on board future Venus space missions would be able to shed new light on the nature of the Venusian atmosphere. Polarimetry is a powerful tool for the study of planetary atmospheres, including (future) observations of exoplanetary atmospheres.

7.7 References

Bagnulo, S., Landolfi, M., Landstreet, J. D. et al. 2009, Publ. Astron. Soc. Pac. vol. 121 pp. 993

Canovas, H., Rodenhuis, M., Jeffers, S. V. et al. 2011, in prep.

Coffeen, D. L., Gehrels, T. 1968, AJ vol. 74, pp. 433

Dollfus, A., Coffeen, D. L. 1970, Astron. Astrophys. vol. 8 pp. 251

Hansen, J. E., & Hovenier, J. W. 1974, J. Atmos. Sci. vol. 31 pp.1137

Kawabata, K., Coffeen, D. L., Hansen J. E. et al. 1980, J. Geophys. Res. vol. 85 pp. 8129

Knibbe, W. J. J., Wauben, W. M., Travis, L. D. et al 1992, In Lunar and Planetary Inst.

Können, G.P., Schoenmaker, A. A., Tinbergen, J. 1993, Icarus vol. 102 pp. 62

Lacis, A. A., Hansen, J. E. 1974, Science vol. 184 pp. 979

Lyot, B. 1924, L'Astronomie vol. 38, pp. 102

Minnaert, M. 1941, Astrophys. J. vol. 93 pp. 403
O'leary, B. T., 1966, Astrophys. J. vol. 146 pp. 754
Piccioni, G., Drossart, P., Sanchez-Lavega, A. et al 2007, Nature vol. 450 pp. 637
Sagan, C., Polack, J. B. 1965, Annales d'Astrophysique, Vol. 28, pp.22
Sromovsky, L. A., Suomi, V. E., Pollack, J. B. et al. 1981, Nature Vol. 292 pp. 698
Svedhem, H., Titov, D. V., Taylor, F. W. et al. 2007, Nature vol. 450 pp. 629
Titov, D. V., Taylor, F. W., Svedhem H. et al. 2008 Nature vol. 456 pp. 620
Travis, L. D., Coffeen, D. L., Hansen, J. E. et al 1979, Science vol. 203 pp. 781

Hoofdstuk 8

Samenvatting in het Nederlands

8.1 Hoge-contrast sterrenkunde

Sterrenkunde wordt al sinds de antieke oudheid beoefend, en is misschien wel de oudste wetenschappelijke discipline. Door de technologische vooruitgang heeft de sterrenkunde de laatste eeuwen een stormachtige ontwikkeling ondergaan. Gedurende duizenden jaren was de waarneming van de sterrenhemel beperkt tot de ongeveer 5600 sterren van de zesde magnitude en helderder die met het blote oog gezien kunnen worden. Een moderne telescoop zoals de Hubble kan echter bronnen tot de 30^{ste} magnitude waarnemen, maar liefst 250 miljoen keer zwakker dan de zwakste sterren die we met het blote oog kunnen waarnemen. Er zijn ook interessante sterrenkundige objecten die niet alleen erg lichtzwak zijn, maar zich ook zeer dicht bij een felle bron bevinden. Een bekend voorbeeld hiervan zijn exoplaneten: planeten rond andere sterren. Door voornamelijk indirecte meettechnieken zijn er hier inmiddels 548 van bekend. Door het grote contrast tussen ster en planeet is het echter zeer moeilijk ze rechtstreeks waar te nemen. Om ons eigen zonnestelsel als voorbeeld te nemen: Vanaf een afstand gezien is het licht dat door Jupiter weerkaatst wordt ongeveer 1 miljard keer zo zwak als het licht dat de zon uitstraalt. Om dit soort objecten waar te nemen zijn zogenaamde *hoge-contrast beeldvormende technieken* nodig. Al sinds het begin van de vorige eeuw wordt veelvuldig gebruik gemaakt van coronagrafie: een klein masker in het beeld bedekt de felle bron, waardoor de zwakkere omgeving, bijvoorbeeld de zonnecorona, zichtbaar wordt. Moderne coronagrafen kunnen contrasten van 10^{-5} halen op 1 boogseconde afstand van de ster, hetgeen niet voldoende is om de overgrote meerderheid van exoplaneten in beeld te krijgen. Een andere aantrekkelijke techniek is polarimetrie. Door het weerkaatsen van het sterlicht raakt het gepolariseerd; het vlak van de elektromagnetische golfbeweging waarmee het licht zich voortplant krijgt een voorkeursrichting. Als alleen het gepolariseerde licht waargenomen kan worden, terwijl ongepolariseerd licht sterk onderdrukt wordt, kan het zwakke licht worden waargenomen dat door

materie rondom de ster gereflecteerd wordt. Polarimetrie en coronagrafie sluiten elkaar niet uit, maar kunnen in combinatie gebruikt worden om een zeer hoog contrast te bewerkstelligen. Behalve voor exoplaneten, kan beeldvormende polarimetrie ook gebruikt worden om stofschijven rond jonge sterren waar te nemen. In deze schijven kunnen zich planeten vormen. Ook rond oudere sterren kunnen zich schijven van stof en puin bevinden, restanten van het proces van planeetvorming. Bepaalde sterren (*Asymptotic Giant Branch* of AGB sterren) spuwen aan het einde van hun leven in relatief korte tijd enorme hoeveelheden stof en gas uit. Ook de nevels die hieruit ontstaan zijn interessante objecten om met beeldvormende polarimetrie waar te nemen. Voor het waarnemen van stof in schijven en nevels rond sterren biedt polarimetrie een aantal extra voordelen. Ten eerste hangt de polarisatiegraad bij een bepaalde golflengte af van de grootte van de reflecterende deeltjes. Ten tweede wordt de polarisatiegraad ook benvloed door de hoek waaronder het licht gereflecteerd wordt. Zodoende kan door middel van polarimetrie ook informatie over de samenstelling en driedimensionale structuur van het stof afgeleid worden. ExPo, *the Extreme Polarimeter*, is door het Sterrekundig Instituut Utrecht ontwikkeld om met beeldvormende polarimetrie in het zichtbare deel van het spectrum een zo hoog mogelijk contrast te realiseren. Polarimetrie is eerder toegepast in sterrenkundige instrumenten om het contrast te verhogen, maar meestal in het infrarode deel van het spectrum en in een aantal gevallen niet-beeldvormend (een-punts metingen). Daarbij wordt polarimetrie vaak toegevoegd aan instrumenten die door vele interne reflecties niet optimaal zijn ontworpen voor gevoelige polarimetrie. ExPo is daarentegen van de meet af aan ontworpen met gevoelige polarimetrie tot doel en is een experimenteel instrument dat door het modulaire ontwerp voortdurend gewijzigd en verbeterd kan worden.

8.2 Het ontwerp van ExPo

Polarisatie kan alleen differentieel, dat wil zeggen door het vergelijken van twee waarnemingen, gemeten worden. Als we bijvoorbeeld ongepolariseerd licht door een polarisatiefilter laten schijnen en het filter vervolgens over 90° draaien, zien we dat in beide gevallen precies 50% van het licht doorgelaten wordt. Is het licht echter in een van de twee richtingen gepolariseerd, dan zal de balans gaan verschuiven. Het is van groot belang om systematische fouten bij het maken van de twee metingen te vermijden. Als de twee metingen enige tijd na elkaar worden gemaakt kan een verschil tussen de twee metingen ook ontstaan doordat de meetomstandigheden in de tussentijd gewijzigd zijn. Worden de metingen gelijktijdig gedaan met twee verschillende detectoren kan het zijn dat deze niet precies even gevoelig zijn. Om systematische fouten te vermijden maakt ExPo daarom gebruik van een meetmethode waarin niet alleen de twee orthogonale polarisatierichtingen tegelijkertijd gemeten worden, maar ook door een polarisatiemodulator herhaaldelijk omgewisseld worden tussen de twee meet-armen van het instrument. Het polarimeterontwerp bestaat ten eerste uit een polariserende splitter-kubus om de twee orthogonale polarisatierichtingen van elkaar te scheiden. Twee rechthoekige prisma's worden gebruikt om

de twee bundels symmetrisch naast elkaar op de camera af te beelden. Door gebruik te maken van één camera worden synchronisatieproblemen vermeden. De polarisatiemodulator is een dubbelbrekend ferro-elektrisch vloeibaar kristal. Door middel van een wisselend spanningsveld wordt de richting van de kristallen veranderd en komt de modulatie van de polarisatie tot stand. De modulatiesnelheid wordt bepaald door de camera, die een maximale beeldfrequentie van 35 Hertz heeft. ExPo-waarnemingen bestaan hierdoor uit lange reeksen beelden met een individuele sluitertijd van iets minder dan 29 milliseconden. Voor de modulator bevindt zich een glasplaat die gekanteld kan worden om de polarisatie die door de derde (Nasmyth) telescoopspiegel wordt gentroduceerd te compenseren. De compensator kan om de optische as van het instrument draaien om de veranderende inclinatiehoek van de telescoop te volgen. Twee lenzen zorgen er voor dat het gezichtsveld van de twee afbeeldingen op de camera 20×30 boogseconden is. De meeste optische elementen zijn in de gecollimeerde bundel tussen de twee lenzen geplaatst om aberraties in het beeldvlak zoveel mogelijk te vermijden. Om boven op de polarimetrie het contrast verder te kunnen verhogen heeft ExPo ook een coronagraaf, bestaande uit een instelbaar masker met stippen van verschillende diameter in het eerste brandpunt van de telescoop, en een Lyot-masker in de pupil na de eerste lens.

8.3 De testsimulator

Voor ExPo is eerst een testsimulator gebouwd. De simulator bestond in eerste instantie uit een gesimuleerde ster met op 1 boogseconde afstand een planeet. Later is hier een simulatie van een circumstellaire stofschijf aan toegevoegd. Twee glasvezels worden gebruikt om de ster en de exoplaneet te simuleren. Het licht van de planeet is lineair gepolariseerd en de polarisatierichting en het contrast met de ster is instelbaar. Het gebruikte licht is breedband in het zichtbare deel van het spectrum, afkomstig van een Xenon booglamp. De beeldvervorming door de turbulentie van de aardatmosfeer wordt nagebootst door een roterende glasplaat waarop haarlak gespoten is. Het aantal lagen lak bepaalt de mate van beeldvervorming. De gesimuleerde stofschijf wordt geprojecteerd op een spiegelend vlak rondom de stersimulatie. Een speciale polarisatieomvormer, gebruikmakend van dubbelbrekende vloeibare kristallen, zet lineaire polarisatie om in het azimutale polarisatiepatroon van een reflecterende stofschijf. Het ontwerp van ExPo is eerst door middel van een prototype geverifieerd met de testsimulator, waarna het uiteindelijke ontwerp is gemaakt. Ook voor het testen van het uiteindelijke instrument, en verschillende verbeteringen daarvan, is de laboratoriumsimulator onmisbaar gebleken.

8.4 Beeldbewerking, kalibratie en gevoeligheid

De ruwe ExPo data bestaat uit lange reeksen digitale beelden, met een om-en-om wisselende modulatorstand. Elk beeld bestaat uit een linker- en rechterhelft met de

twee orthogonale polarisatiecomponenten van het waargenomen object, in elk volgende beeld wisselen de componenten van kant. Uit de vier beelden van de linker- en rechterhelft van twee opeenvolgende beelden kan het lineair gepolariseerde beeld verkregen worden. Hiervoor worden de beelden eerst voor donkerrespons en gevoeligheidsvariatie gecorrigeerd en nauwkeurig met elkaar uitgelijnd. Het promotieonderzoek van mijn collega Hector Canovas is geheel gewijd aan de beeldbewerking van ExPo data. Een meetreeks kan de polarisatie in twee orthogonale richtingen bepalen maar is ongevoelig voor de polarisatie die daarmee onder een hoek van 45° staat. Om het volledige polarisatieveld te bepalen moet de modulator daarom gedraaid worden en een tweede meeting voor de polarisatiecomponenten onder 45° gedaan worden. Om de polarisatiemetingen te kalibreren worden metingen gedaan van de verlichte binnenkant van de telescoopkoepel of van ongepolariseerde kalibratiesterren. Hierbij wordt een lineaire polarisator in het instrument geschoven. Uit metingen van 16 verschillende combinaties van modulator- en polarisatorhoek kan de polarisatierespons van het instrument berekend worden. Door twee metingen van het polarisatieveld (45° uit elkaar) te vermenigvuldigen met de verkregen kalibratiematrix wordt het gekalibreerde eindbeeld verkregen. De nauwkeurigheid van deze kalibratieprocedure is beter dan 1%. De gevoeligheid van het instrument, dat wil zeggen de mate waarin ongepolariseerd licht onderdrukt wordt, is veel hoger. Voor een observatie van 10 minuten van de ongepolariseerde ster MWC480 met een magnitude van 7.7 is deze gevoeligheid, en dus het behaalde contrast, ter plekke van de ster 10^{-4}. Op 1 boogseconde afstand leidt dit tot een contrast van 10^{-6}. Deze gevoeligheid grenst aan het door de fotonenruis maximaal haalbare. Door langere waarnemingen kan dus een hoger contrast gerealiseerd worden.

8.5 Eerste resultaten

Met ExPo zijn drie zeer succesvolle waarnemingscampagnes uitgevoerd bij de 4.2m William Herschel Telescoop op La Palma, het meest westelijk gelegen Canarische eiland. Twee korte campagnes hebben door slechte weersomstandigheden weinig bruikbare resultaten opgeleverd. De waargenomen objecten zijn voornamelijk protoplanetaire stofschijven rond jonge (Herbig Ae/Be) sterren en de uitgestoten stofwolken van oude (post-AGB) sterren. Rond een aantal sterren heeft ExPo voor het eerst de protoplanetaire schijf in beeld kunnen brengen. Aan het einde van de inleiding van mijn proefschrift is een viertal voorbeelden van deze waarnemingen te vinden. De complexe stofwolk rond de jonge ster T-Tauri siert ook de kaft. Een bekend voorbeeld van een protoplanetaire schijf is die rond de ster AB Aurigae. Andere waarnemers hebben met de coronagraaf van de 8m Subaru telescoop en een geavanceerd AO (Adaptieve Optiek) systeem voor correctie van de atmosferische turbulentie een spiraalstructuur in deze schijf waargenomen. Deze kan het resultaat van planeten in wording zijn. In onze waarnemingen van AB Aurigae (einde van hoofdstuk 4) is deze spiraalstructuur ook te zien, enkel in polarimetrie, met een aanzienlijk kleinere telescoop en zonder gebruikmaking van een AO-systeem. Daarbij

zijn onze waarnemingen in het zichtbare deel van het spectrum, terwijl die van de Subaru in het infrarood gemaakt zijn.

8.6 Mira

Mira is een afgekoelde reuzenster van 1.18 zonsmassa's in de AGB-fase. De ster stoot grote hoeveelheden stof en gas uit die een wolk vormt rond de ster. Mira is tevens een variabele dubbelster; de (nog niet rechtstreeks waargenomen) begeleider is mogelijk een witte dwerg. Met ExPo is de asymmetrische stofwolk rond Mira zeer goed in beeld te brengen (hoofdstuk 5). We hebben de ExPo waarnemingen vergeleken met een model van de stofwolk waarin we de samenstelling en grootteverdelingen van de stofdeeltjes en de vorm van de wolk kunnen controleren. De waarnemingen komen het beste overeen met een sterk bipolaire wolk bestaande uit amorf silicaat en een kleine hoeveelheid ijzer, met deeltjes tussen de 0.005 en 0.05 micrometer. De bipolaire as staat onder een hoek van 40° met het beeldvlak. Deze waarnemingen zijn een goed voorbeeld van de toegevoegde waarde van de polarimetrie. Niet alleen wordt de wolk door het behaalde contrast zichtbaar, de polarisatiegraad geeft ook informatie over de stofsamenstelling en structuur van de wolk.

8.7 Contrast van 10^{-8} in het laboratorium

ExPo is tot nu toe gebruikt zonder adaptieve optiek (AO), een systeem om de beeldvervorming door turbulentie in de aardatmosfeer te corrigeren. De vervorming zorgt ervoor dat waarnemingen minder gedetailleerd zijn. Het beperkt ook de polarimetrische gevoeligheid, en daarmee het behaalde contrast van het instrument. Zonder de beeldscherpte die een AO systeem kan bewerkstelligen is de coronagraaf van ExPo, die het contrast verder zou kunnen verhogen, niet erg bruikbaar gebleken. Met metingen met onze laboratoriumsimulator is nagebootst hoe hoog het contrast zou kunnen zijn als ExPo wél een AO systeem zou hebben. Hiertoe is de roterende glasplaat waarmee de atmosferische turbulentie wordt nagebootst uit de laboratoriumsimulator weggehaald. Met gebruikmaking van de coronagraaf haalt ExPo dan een contrast van 10^{-8} op 1 boogseconde van de ster (hoofdstuk 6). De metingen zijn nog niet helemaal optimaal; een contrast van 10^{-9} zou zeker haalbaar moeten zijn. Inmiddels wordt voor ExPo een eigen AO-systeem ontwikkeld. Speciale aandacht wordt daarbij besteed aan het zoveel mogelijk beperken van de eigen (instrumentele) polarisatie die dit AO-systeem creert.

8.8 Polarimetrie van de Venusatmosfeer

Tijdens een van de laatste waarnemingscampagnes was Venus goed zichtbaar aan de avondhemel, bij een fasehoek van 48°. De kans is toen gegrepen om Venus met ExPo te observeren, gebruikmakend van zowel smal- als breedband filters. In de

waarnemingen met de smalband filters is iets interessants waargenomen: smalle gepolariseerde ringen die de intensiteitcontouren op de planeet volgen (hoofdstuk 7). Het is nog steeds mogelijk dat hier sprake is van een instrumenteel effect, maar de meest voor de hand liggende instrumentele verklaringen hebben we uit kunnen sluiten. Zo zijn de ringen alleen zichtbaar als de individuele beelden precies met elkaar uitgelijnd worden, terwijl je bij een optisch-instrumenteel effect zou verwachten dat dit het sterkste zou zijn zonder de verschuivingen die nodig zijn om de beelden uit te lijnen. Dit ringeffect is voor zover bekend nog niet eerder waar genomen. Er zijn echter ook geen andere smalband polarimetrische waarnemingen met de gevoeligheid van ExPo van Venus bekend. Andere aspecten van de waarnemingen van Venus, zoals de richting van de waargenomen polarisatie en de hogere polarisatiegraad richting de polen, komt goed overeen met eerdere waarnemingen. Met modelberekeningen aan de venusatmosfeer wordt momenteel gezocht naar een mogelijke verklaring van de ringen.

8.9 Vooruitblik

Dit proefschrift documenteert niet het einde maar het begin van de ontwikkeling van ExPo. Nieuwe promovendi en studenten zijn al hard aan het werk aan verbeteringen en uitbreidingen. Daarvan werd een eigen Adaptieve Optiek systeem al genoemd. Ook wordt gewerkt aan een zgn. Integral Field Unit, een uitbreiding waarmee de waarnemingen gelijktijdig in een aantal golflengtegebieden gedaan kunnen worden. De ervaring die met ExPo opgedaan is wordt ook toegepast bij het testen van het nieuwe Sphere-ZIMPOL instrument voor de Europese Very Large Telescope. Dit instrument heeft ook een beeldvormende polarimetrie-modus, zij het met een ietwat ander concept dan dat van ExPo. Voor de langere termijn wordt in Utrecht inmiddels gewerkt aan het EPICS-EPOL instrument, waarvan het ontwerp voor een groot deel van ExPo is afgeleid. Dit instrument, voor de toekomstige European Extremly Large Telescope (spiegelmiddellijn 42m), moet in staat zijn exoplaneten rechtstreeks waar te nemen en te karakteriseren.

Acknowledgements / Dankwoord

I owe a large number of people for the contributions they have made to this work, but this list without a doubt starts with my thesis supervisor, Christoph Keller. With my engineering background and working at a commercial company, I must have been quite an unusual candidate for a PhD in astrophysics. But this did not deter you from hiring me. You gave me lots of freedom to discover and learn but stood ready with advice and encouragement when needed. I am especially thankful for the understanding you have of the complications that occasionally arise with a young family. I feel proud and privileged to be a member of your impressive team a while longer.

This thesis would not have been possible without the other members of the ExPo team, Sandra Jeffers, Hector Canovas, and now also Maria de Juan. The fun and excitement of our La Palma expeditions have been the highlights of my PhD. Hector, you have not only been an invaluable sparring partner on all things ExPo, but also a fun office mate.

Several students made substantial contributions to the work presented here: Nick Miesen, I will always associate the smell of hairspray with atmospheric seeing simulation... Lars Einarsen, I enjoyed seeing you get the hang of optical design and having fun with the disk simulator. Brigitte Sprenger, your work on the IFU, though it did not make it to this thesis, has a big future ahead of it.

ExPo would not have been possible without the expertise and hard work of many people at the University's Scientific Instrumentation workshop. Although I am bound to forget someone, I would like to name a few: Dante Killian, Jos van Gemert, Marcel Rossewij, Sander Deelen, Kees van der Neut, Christian Straman, Jos Haverkamp, Piet Hoogendoorn and everybody on the workshop floor. I am grateful to you all.

The success of the ExPo observations are to a large degree due to the excellent support we have invariably received at the William Herschel Telescope. I would like to thank everybody there many times, in particular Juerg Rey, Chris Benn, Frank Gribbin, Luis Hernández and all the telescope operators.

To get ExPo to the telescope on time, in spite of ash clouds and the intricacies

of Spanish customs, the help of Rob Hammerschlag and Felix Bettonvil has been invaluable.

I gratefully acknowledge the financial support of the Netherlands Organisation for Scientific Research, NWO, for supporting ExPo financially.

One person, though only loosely associated with ExPo, deserves much credit for the countless contributions he has made to the project: Frans Snik. Frans, whether it was a logo, a problem with the calibration or background papers on Venus, I could always count on you for help. I thoroughly enjoyed our trip to La Silla and hope we still have many such adventures ahead of us.

I am also indebted to Michiel Min for teaching me new things about dust and circumstellar disks, and for his contribution to the analysis of the Mira observations.

I would like to thank my reading committee (professors Bram Achterberg, Hans Gerritsen, Alex de Koter, Jan-Willem Pel and Frank Verbunt) many times for their encouragement and useful critique.

At the institute, Marion Wijburg and Sake Hoogeveen keep things running and I am grateful for their support. Finally, a big thanks to all the people at the institute that make working there interesting and fun.

Zeer veel dank ben ik verschuldigd aan mijn oude vrienden Jeroen Webers en Bas Vellekoop, voor alle lol die we door de jaren heen gehad hebben en voor jullie bereidheid om vanuit de verste uithoeken van de wereld (Buenos Aires en Sakhalin island) naar Utrecht af te reizen om mijn paranimfen te zijn. Fantastisch!

Lieve ouders, aan jullie liefde, steun en aanmoediging dank ik bijna alles in mijn leven. Jullie stonden ook gedurende deze onderneming weer altijd voor mij klaar. Bedankt voor alles.

Ria en Leo, ook jullie hulp in moeilijke tijden was voor dit project onontbeerlijk.

Lieve Elske en Marinke, jullie weten het nog niet, maar jullie hebben ook een belangrijke bijdrage aan dit werk geleverd. Jullie onbekommerde vrolijkheid herinnert mij er telkens aan dat er meer is in het leven dan het kalibreren van waarnemingen en schrijven van papers. Soms is dat hard nodig.

Allerliefste Karin, mijn laatste en grootste dank is natuurlijk voor jou. Zonder jou was ik hier nooit aan begonnen, en zonder jouw steun en liefde had ik het nooit afgemaakt. Ik hou van je.

Curriculum Vitae

Michiel Rodenhuis was born on 25 September 1971 in Schiedam, the Netherlands, but spent most of his childhood in Denmark. At the age of 17, his family moved back to the Netherlands and he completed his secondary education (VWO-B) at the "Christelijk Lyceum" in Gouda in 1990. He spent the next year in Montpellier, France learning French and enjoying himself.

Michiel then started studying Aerospace Engineering at the TU Delft. The studies were interrupted for a year while he was president of the student society "DSV Sint Jansbrug". During his student project, he participated in building the Young Engineers Satellite, a space tether experiment, at the European Space Technology Centre (ESTEC). Michiel travelled to the Korou spaceport to help prepare the satellite for launch and acted as spacecraft operations coordinator during the 3-day mission. His thesis project, a test-bed simulator for the Lunarsat mission, was also conducted at ESTEC and supervised by prof. Wubbo Ockels. Michiel received his MSc in 1999.

He spent the next year and a half at the European Space Operations Centre in Darmstadt, Germany, working as a Young Graduate Trainee on the operations simulators for the Mars Express and Rosetta missions. During this period he also spent two months in Valparaiso, Chile at the International Space University summer school.

After returning to the Netherlands, Michiel worked for several years at TERMA B.V. in Leiden on simulation projects for the European Space Agency. This included work on SMART-1, the Automated Transfer Vehicle, and the Galileo satellite navigation system.

A desire to learn more about the fascinating universe surrounding us led Michiel to pursue a PhD in experimental astrophysics, and he started at the Utrecht Astronomical Institute at the beginning of 2007. He developed and built the Extreme Polarimeter (ExPo), the subject of this thesis. Michiel also assisted in the development and commissioning of the HARPS spectropolarimeter.

After completing his PhD, Michiel will build on the experience gained with ExPo to work on the polarimeter for EPICS, the exoplanet characterization instrument planned for the European Extremely Large Telescope.

Michiel lives in Rotterdam together with Karin and their two young daughters, Elske and Marinke.

Atheism is more than the knowledge that gods do not exist, and that religion is either a mistake or a fraud. Atheism is an attitude, a frame of mind that looks at the world objectively, fearlessly, always trying to understand all things as a part of nature.

- Carl Sagan